Doctor Dissertation

Band Engineering of $AgInS_2$ Core/Shell Semiconductor Quantum Dots for Photoluminescence Redshift

($AgInS_2$ 半導体量子ドットのバンドエンジニアリングによる発光レッドシフト)

Navapat Krobkrong

November 2023

Department of Applied Chemistry

Graduate School of Engineering,

Osaka University

Preface

This study was conducted during 2021–2023 under the supervision of Professor Dr. Susumu Kuwabata at the Department of Chemistry, Graduate School of Engineering, Osaka University.

The objective of this thesis is to develop band engineering techniques for silver indium sulfide-based core/shell semiconductor quantum dots (QDs), in particular for photoluminescence redshift. This thesis presents the structural design of core/shell QDs to control the charge distribution within the particles by designing band alignment.

The author firmly believes that this study would provide further insight into the band engineering of silver indium sulfide-based QDs. Additionally, the knowledge obtained in this work will contribute to the development of nanomaterials towards achieving sustainable development goals.

Navapat Krobkrong

Department of Applied Chemistry,

Graduate School of Engineering,

Osaka University,

Suita, Osaka,

JAPAN

November 2023

List of Publications

1. Emission Tuning of $AgInS_2$-Based Core/Shell Semiconductor Quantum Dots with Type-II and Quasi-Type-II Band Alignments

   Navapat Krobkrong, Taro Uematsu*, Tsukasa Torimoto, and Susumu Kuwabata*

   Japanese Journal of Applied Physics **2023**, *62* (6), 061003

   DOI: 10.35848/1347-4065/acd895

2. Photoluminescence Redshift of $AgInS_2$ Quantum Dots by Employing Shells with Graded Composition

   Navapat Krobkrong, Taro Uematsu*, Tsukasa Torimoto, and Susumu Kuwabata*

   Electrochemistry **2023**, *91(10)*, 107001

   DOI: 10.5796/electrochemistry.23-00084

3. Bright Red Luminescence from Ag−In−Ga−S-based Quantum Dots with the Introduction of Copper

   Taro Uematsu,* **Navapat Krobkrong**, Ken-ichiro Asai, Genichi Motomura, Tsukasa Torimoto, and Susumu Kuwabata*

   Bulletin of the Chemical Society of Japan **2023**, *96(11)*, 1274–1282.

   DOI: 10.1246/bcsj.20230216

Content

General Introduction

Semiconductors are materials that have a moderate bandgap (E_g) compared to insulator, with their Fermi level typically located near the middle of the bandgap.[1] When a semiconductor is irradiated with light whose energy exceeds the bandgap, electrons jump across the bandgap. The excited electrons are thus accommodated in the conduction band (CB), leaving positive charges, called holes, in the valence band (VB) as illustrated in **Fig. I (center)**.

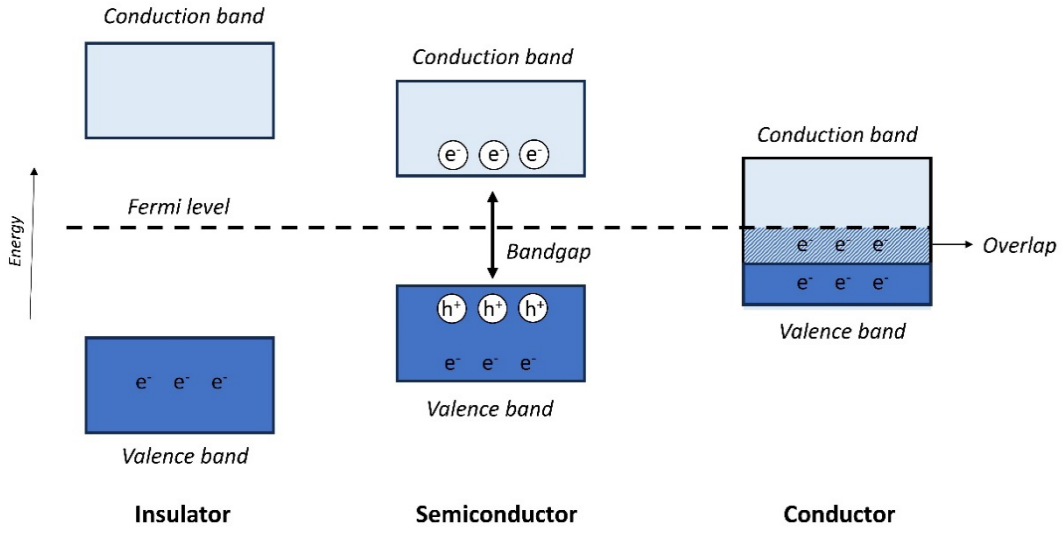

Figure I. Schematic energy diagrams of insulator, semiconductor, and conductor.

The interaction with photons unique to semiconductors is useful for various applications such as photocatalysts[2-4] and fluorescent materials.[5-6] After the light irradiation, the excited electrons and positive holes are generated as displayed in arrow (1), **Fig II (a, b)**). In photocatalyst (generally TiO_2[7-8] and ZnO[9-10]), the electrons and holes move apart and eventually reach the surface to react with adsorbed species (seen in arrow (2), **Fig II (a)**).[11-13] Therefore, preventing charge recombination is particularly important for improving photocatalytic performance. Conversely, in fluorescent materials, after the electrons and holes recombine, emitting light that corresponds to the energy gap between the CB and VB as

shown in arrow (2), **Fig. II (b)**. This process is known as the band-edge emission. While the efficiency of photoluminescence (PL) can be improved by enhancing the charge recombination of the photogenerated carriers, semiconductors in the bulk state are far from such a situation; they do not exhibit PL unless they are cooled to cryogenic temperatures.

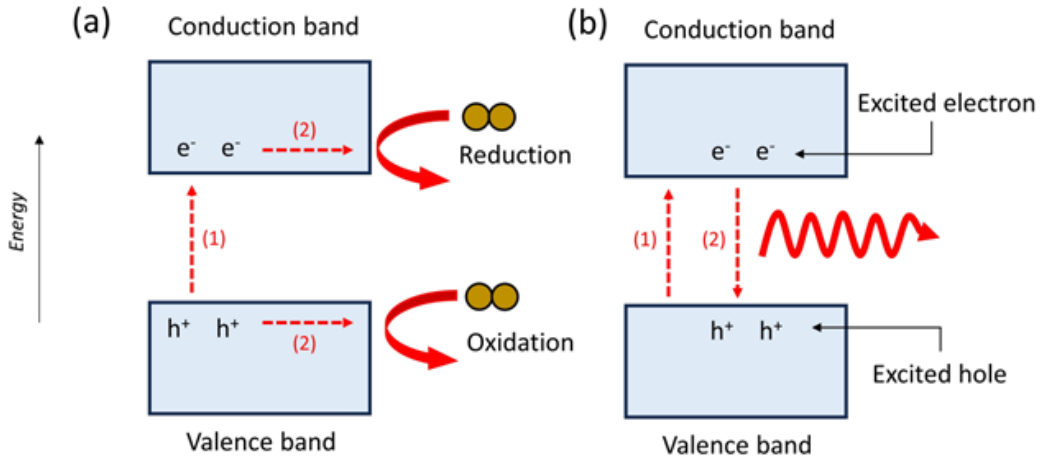

Figure II. Mechanisms of (a) photocatalytic reaction and (b) fluorescence under light whose energy exceeds the bandgap. The red-dash arrows display the flow of excitons after the materials are excited by light.

I. Semiconductor quantum dots (QDs) and their quantum size effect

Semiconductor quantum dots (QDs) are defined as semiconductor particles with few nanometers in size. When one or more dimensions of a semiconductor material are reduced to the level of the Bohr exciton radius (typically 1–20 nm), the photoexcited electrons and holes are restricted to specific wavefunctions.[14-15] As a result, their energy becomes quantized, similar to the electrons surrounding an atomic nucleus. The density of states of the semiconductor, which is originally continuous and monotonically increasing from the band edge inward, becomes partially discretized due to the aforementioned quantization effect (**Fig. III (a)**).[16-17] The changes in the band structure affect the optical absorption. With a decrease in particle size, multiple pronounced peaks appear in the ultraviolet–visible (UV–vis) spectra (**Fig. III (b)**) In addition, the energy eigenvalue for each quantized wavefunction shifts

higher as the particle size decreases. This effect shifts the conduction band-edge potential to the negative direction, while shifting the valence band-edge potential to the positive direction. As a result, the bandgap increases with decreasing particle size. These phenomena are known as the quantum size effect. Meanwhile, room temperature PL is another important feature of QDs that has elevated them to their current position as an efficient light source in display applications. The emission is partly due to the overlapping electron/hole wavefunctions, which accelerates the carrier recombination rate. Although Henglein and Brus et al. found weak luminescence from CdS colloids in the 1980s, this PL originated from spontaneously generated defect levels in the crystal or on the surface.[18-19] It was in 1993 that Murray and Bawendi et al. found the spectrally narrow band-edge PL, an emission originating from the band-edge transition, in the QDs capped with alkyl phosphines and phosphine oxides.[20] The combination of band-edge PL and bandgap shifts by size creates useful fluorophores; for instance, at room temperature, PL emission can be obtained when the size is smaller than the bulk Bohr radius (~5.8 nm). Besides, the emission energy can be easily tuned by varying their diameter (seen in **Fig. II (b)**).[21-23] This effect enables control over the emission characteristics by manipulating their size[21-23], shape[17, 24], structure[25-26], and surface properties[27-29] Due to these unique properties, semiconductor QDs have attracted much attention in various applications of fluorescence, such as fluorescent labeling in biochemistry[30-31], wavelength conversion[32-33], and light emitting diodes (LEDs)[34-35]

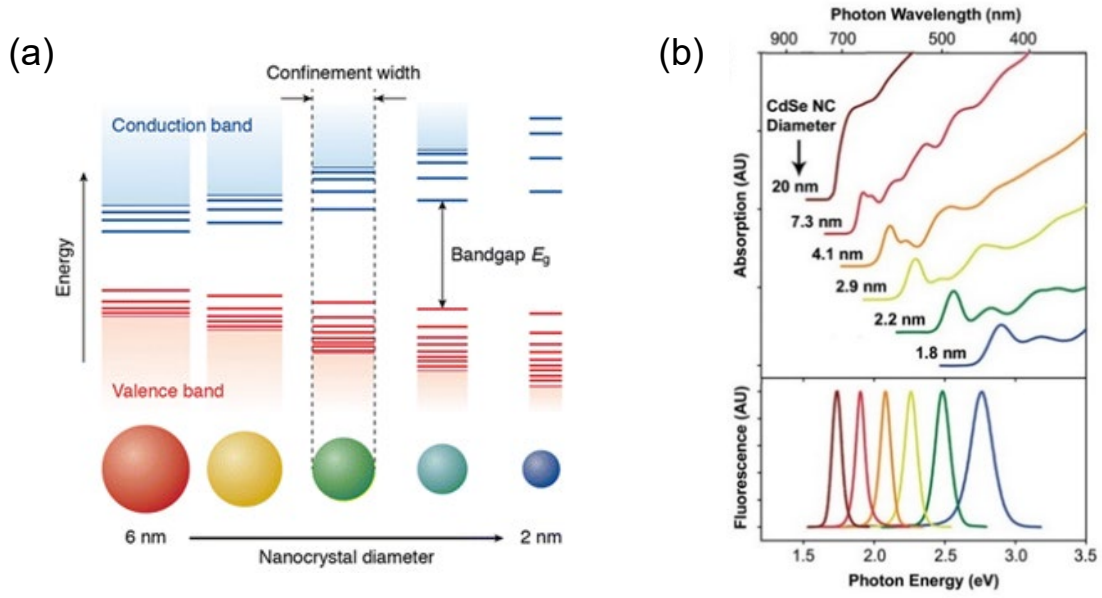

Figure III. (a) Schematic representation of the quantum confinement effect on the electronic states of semiconductor materials (cited from the publication[36]) and (b) optical properties of CdSe semiconductor NCs with size tunability (cited from the publication[21]).

The simplest systems in which quantum size effects are observed are semiconductor films with a thickness equal to or less than the Bohr exciton radius. The bandgap shift can be theoretically calculated by a one-dimensional quantum well model, as shown in **Fig. IV (a)**.[37] In this model, the potential energy ($V(x)$) inside the well, between $x = 0$ and $x = L$, is zero, and the potential energy outside the well, where $x > L$, is infinite, as written below,

$$V(x) = \begin{cases} 0, & 0 < x < L \\ \infty, & x > L \end{cases} \quad (I)$$

This environment allows charge carriers to move freely in the well and prohibits any penetration of charge carriers into the wall, as if the walls on both sides were impermeable barriers. The following is Schrödinger equation written in one-dimensional coordinates (x)

$$-\frac{\hbar^2}{2m}\frac{d^2\psi(x)}{dx^2} + V(x)\psi(x) = E\psi(x) \quad (II)$$

where $\hbar$ is Planck's constant divided by 2π, E is the energy eigenvalue, $\psi(x)$ is the eigenfunction, and m is the effective mass of the charge carriers.

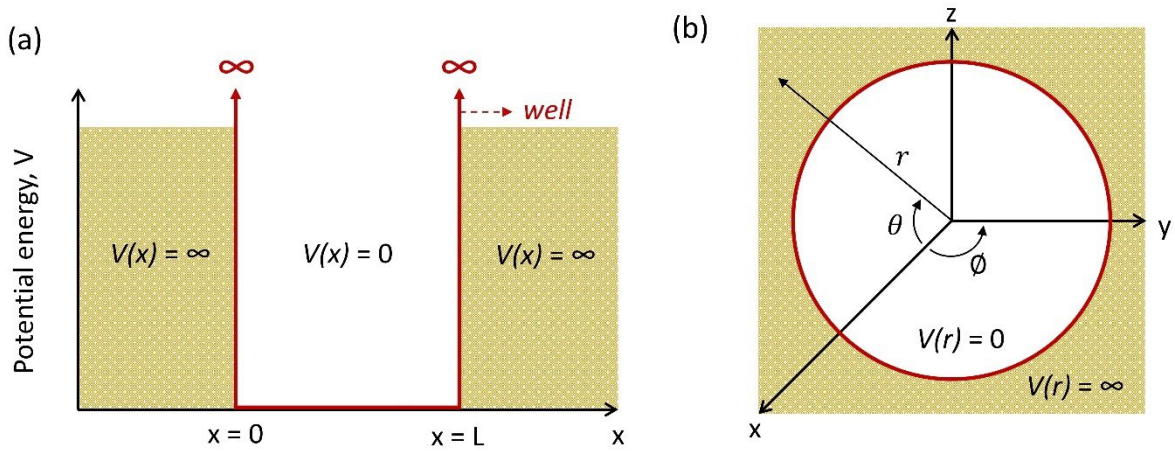

Figure IV. Energy diagrams for the infinite quantum well model; (a) one-dimensional well and (b) spherical model with a particle radius r_0.

On the other hand, when calculating the size effect in semiconductor QDs, the three-dimensional spherical model should be used instead (see in **Fig. IV (b)**). In this model, a carrier is confined in a spherical container and the potential outside the container is infinite, which is called the infinite spherical well model. The potential energy can be expressed by the following equations using the particle radius, r_0 and the extra-particle potential energy $V(r) = \infty$,

$$V(r) = \begin{cases} 0, & r < r_0 \\ \infty, & r > r_0 \end{cases} \quad (III)$$

Under this boundary condition, it is better to convert the Schrödinger equation into spherical coordinates, as shown below,

$$-\frac{\hbar^2}{2m}\left(\frac{\partial^2}{\partial r^2}+\frac{2}{r}\frac{\partial}{\partial r}+\frac{1}{r^2}\Lambda^2\right)\psi(r,\theta,\phi)+V\psi(r,\theta,\phi)=E\psi(r,\theta,\phi) \quad (IV)$$

When the angular mentum quantum number, l, is equal to 0, the equation can be simplified as

$$-\frac{\hbar^2}{2m}\left(\frac{d^2}{dr^2}+\frac{2}{r}\frac{d}{dr}\right)R(r)+VR(r)=ER(r) \quad (V)$$

with the eigenfunction $R(r)$ separated from $\psi(r,\theta,\phi)$ to have only the radial function.

The actual materials do not possess infinite potential. Instead, they are composed of organic ligands or, for core/shell QDs, semiconductors with a larger bandgap. This concept,

termed the Finite Depth Effective Mass Approximation (FDEMA), allows for a more accurate prediction of QD bandgaps, as depicted in **Fig. V (a, b)**.[38-40] Particularly, the FDEMA is suitable for predicting quantum size effects observed in regions with relatively large particle sizes. The parameters used for calculation include the bulk bandgap of QDs, the electron mass (m_e), the hole mass (m_h), the energy difference between the core and matrix (ligand) (V_0), and the relative permittivity (ϵ_r) of the semiconductor. Therefore, the feature of this model is that it considers the leakage of the wavefunction into the environment, which does not exist when infinitely high walls are assumed.

Applying a finite value ($V(r)$) to the potential energy outside the particle gives the following equations;

$$\frac{d^2R(r)}{dr^2}+\frac{2}{r}\frac{dR(r)}{dr}+\left(\frac{2mE}{\hbar^2}\right)R(r)=0 \quad (r<r_0,\text{core}) \quad \text{(III)}$$

$$\frac{d^2R(r)}{dr^2}+\frac{2}{r}\frac{dR(r)}{dr}-\left(\frac{2m|E-V_0|}{\hbar^2}\right)R(r)=0 \quad (r>r_0,\text{surroundings}) \quad \text{(IV)}$$

The following substitutions

$$k_{\text{in}}^2=\frac{2mE}{\hbar^2} \quad (V)$$

$$k_{\text{out}}^2=\frac{2m|E-V_0|}{\hbar^2} \quad (VI)$$

gives the following eigenfunctions:

$$R(r)\propto\frac{\sin(k_{\text{in}}r)}{k_{\text{in}}r} \quad \text{(Bessel function)} \quad (VII)$$

$$R(r)\propto-\frac{\exp(k_{\text{out}}r)}{k_{\text{out}}r} \quad \text{(Hankel function)} \quad (VIII)$$

Applying a boundary condition

$$\frac{\sin(k_{\text{in}}r_0)}{k_{\text{in}}r_0}=-\frac{\exp(k_{\text{out}}r_0)}{k_{\text{out}}r_0} \quad (IX)$$

gives the energy eigenvalue defined in eq V. The eigenvalues for the electron in the CB and the hole in the VB become the energy offsets from the bulk state (ΔE_{e} and ΔE_{h}).

On the other hand, there is a Coulomb interaction between the electron and the hole. This can be calculated with a simple equation,

$$E_{\mathrm{coul}} = -1.75 \times \frac{e^2}{\epsilon R} \quad (X)$$

using the relative permittivity, ϵ, and the elementary charge, e.

Taking all factors together, the bandgap variation due to particle size is

$$E_{\mathrm{g}} = \Delta E_{\mathrm{e}} + \Delta E_{\mathrm{h}} + E_{\mathrm{coul}} + E_{\mathrm{g,\,bulk}} \quad (XI)$$

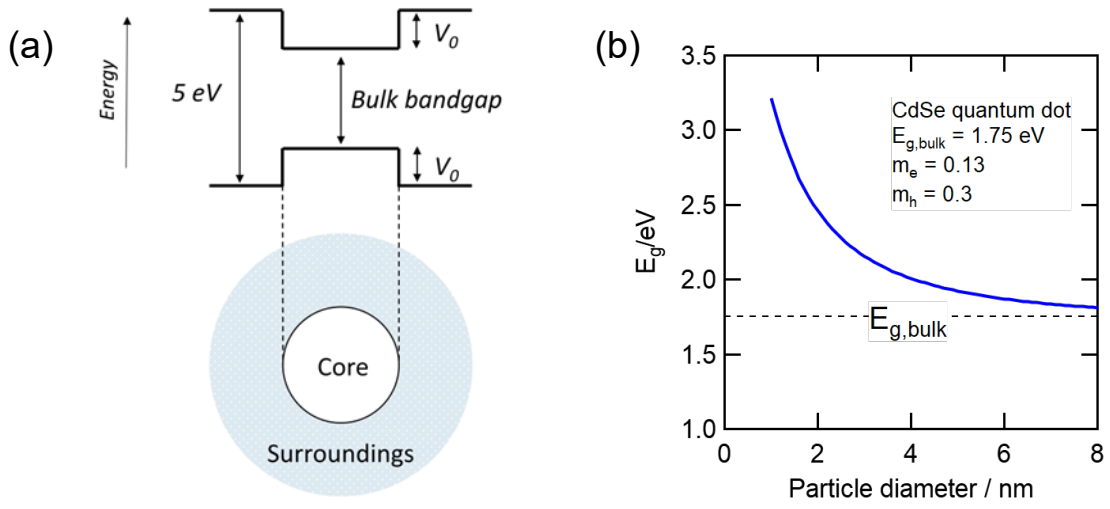

Figure V. (a) Schematic energy diagram and (b) relationship between bandgap and diameter of CdSe QDs calculated by FDEMA approach. A surrounding matrix (E_g = 5.00 eV) was adopted.[41]

II. Silver indium sulfide QDs with core/shell structure

Silver indium sulfide ($AgInS_2$, AIS) QDs are ternary semiconductor QDs belonging to the group 11–13–16 semiconductor family, which includes $CuInS_2$ and its selenide derivatives. Since the discovery of luminescence, AIS QDs have attracted interest for their outstanding properties, including their low toxicity, color tunable PL, and a large extinction coefficient due to direct transition.[42-44] The absence of environmentally hazardous metals

makes them an alternative to Cd and Pb chalcogenide QDs (CdSe[45-46], CdTe[47-48], and PbS[49-50]). However, these QDs exhibit spectrally broad emission with a full width half maximum (FWHM) of more than 300 meV, with a large Stoke shift between the PL peak and the absorption edge. This emission is due to donor–acceptor pair (DAP) recombination via intrinsic defects, such as surface defects and crystalline defects, the former consisting of oxide and the latter consisting of interstitial atoms or atomic vacancies, as shown in **Figs. VI (a, b)**. However, in the case of QDs, surface defects often dominate because of their very large specific surface area. For display applications, broadband emission is undesirable because it degrades color purity.

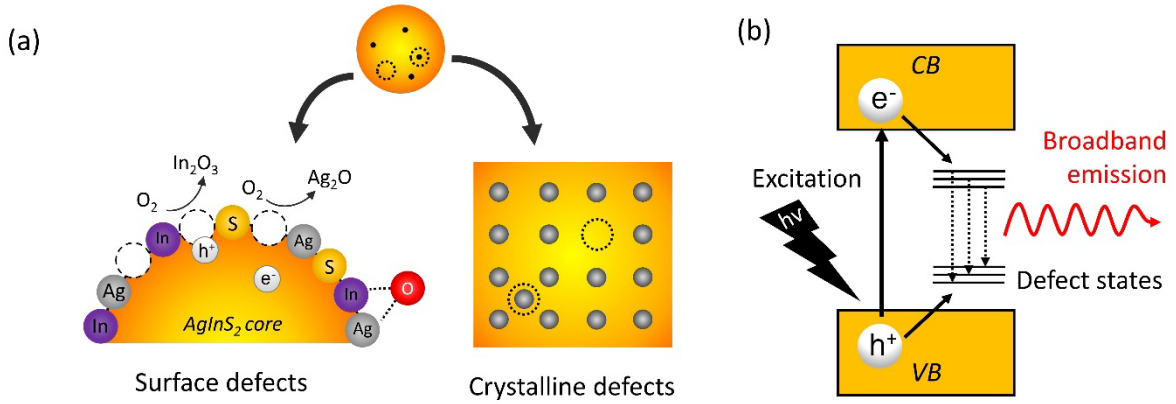

Figure VI. (a) Schematics of defects in QDs and (b) energy diagram of photoluminescence via defect sites. [51-52]

The typical method to remove surface defects is to grow a shell of another semiconductor material to construct a core/shell structure. Besides, the semiconductor shell can improve the long-term stability by suppressing the surface oxidation of the core surface. Typically, the core/shell structure is classified into 4 types based on the band alignment of the core and shell materials, as shown in **Fig. VII**.[53-54] In type I, the CB and VB edges of the core are within the bandgap of the shell. The carriers are confined to the core region. In quasi-type II (or quasi-type I), either the CB or VB edge of the core is close to that of the shell. As a result, one of the electrons or holes is delocalized throughout the particle, while another

carrier is kept confined to the core. In type II, the CB or VB edges of the core are in the bandgap of the shell. One carrier is localized in the core and the other in the shell. The last reverse type I is the opposite case of the normal type I band alignment, where the carriers are mostly delocalized in the shell region. Each type of core/shell QD exhibits optical properties characteristic of its electronic structure, i.e., PL wavelength, PL lifetime, and material stability.

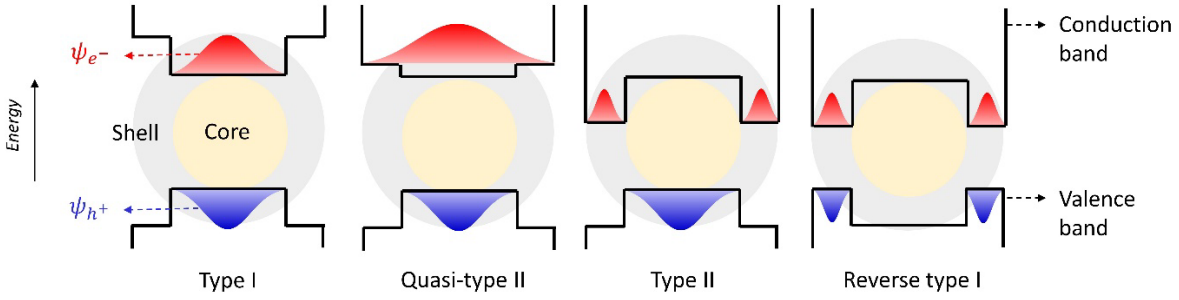

Figure VII. Schematic band alignment of different core/shell structure: type I, type II, quasi-type II and reverse.

Type I is best suited for fluorescent materials. The leakage of excited electrons and holes can be suppressed by the strong confinement of the wide bandgap shell. It enhances charge recombination, resulting in an increase in PL QY without changing the spectral shape, except for a minor redshift due to a variation in the wavefunction.[54] Over the past 30 years, ZnS has been widely used as a shell material. In fact, it has been useful for CdSe and InP QDs, achieving nearly unity PL QY depending on the formation conditions. Therefore, the same ZnS shell was used for the groups 11–13–16 QDs because the bandgap of the shell ($E_{g,\,bulk}$ = 3.7 eV) is considered suitable to meet the type I criteria and stabilize the surface of AIS and $CuInS_2$ cores.[55-56] However, whereas ZnS shell improved the PL QY and stability, it did not narrow the broadband PL spectra generated by DAP recombination. This result indicates that the Zn–S shell was ineffective in removing the surface traps of AIS QDs. On the other hand, a significant blueshift of PL was observed due to the formation of silver indium zinc

sulfide alloy[57] and/or due to the variation of defect levels by contact with ZnS. Remarkably, in 2018, the research group I am affiliated with successfully achieved a spectrally narrow band-edge emission from AIS QDs by coating a wide-bandgap gallium sulfide (Ga–S) shell.[51-52] The Ga–S shell was coated on the AIS core without alloying. It was assumed that the contact with the Ga–S shell effectively removed the defects of the AIS core, unlike the ZnS shell, which only changed the energy level of the defects while maintaining the nature of the emission. Moreover, the AIS/Ga–S core/shell QDs demonstrated the high PL QY over 50% due to the removal of non-radiative emission from the surface trap states.

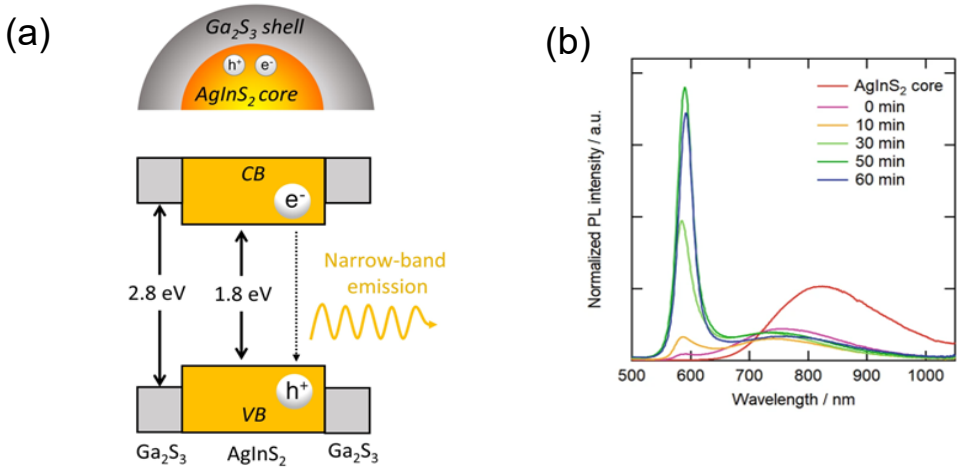

Figure VIII. (a) Band alignment of AIS/Ga–S core/shell QDs (adapted from the publication[52]) and (b) time-resolved PL spectra of Ga–S coating on AIS core QDs (cited from the publication[52]).

III. Wavelength tunability of AIS-based core/shell QDs

Many studies have been devoted to precisely tuning the PL of group 11–13–16 semiconductor QDs to expand their applications. [58-59] In particular, fluorophores with three primary color emissions–blue, green, and red–are required for display applications. [60-61] A common strategy for modifying these QDs involves an alloying process that allows control of the PL wavelengths by changing the chemical composition.[62-63] For instance, systematic

emission tuning of $AgIn_xGa_{1-x}S_ySe_{1-y}$ QDs was achieved for the visible to near IR regions.[46] Since the band gap of $AgInS_2$ (E_g, bulk = 1.8 eV) is larger than that of $AgInSe_2$ (E_g, bulk = 1.2 eV), the PL spectra were shifted to longer wavelengths by increasing the Se/(S+Se) ratio.

Band engineering within core/shell structures offers an alternative approach to tuning PL wavelengths. In addition to stoichiometry control, which directly alters the bandgap of emissive QDs, band engineering involves controlling the distribution of charge carriers in the core and shell regions.[64] For binary QDs, there are common strategies to use band-structure design for both core and shell, as illustrated in **Fig. IX.**

1) Type II structure: The formation of type II QDs is a common approach to redshift the PL wavelength. Due to the staggered band structure, charge recombination occurs across the interface, leading to a redshift compared to band-edge emission of core QDs, as illustrated in **Fig. IX (a)**.[65] Thus, the emission wavelength of type II-QDs is strongly dependent on the core and shell materials. Xiaomin et al. successfully achieved PL redshift of Cu_2S/CdS core/shell QDs with type II band alignment.[65] Since the CB of CdS is in the bandgap of Cu_2S, the emission wavelength was systematically changed from 515 to 760 nm by changing the core size and shell thickness.

2) A graded shell: The formation of a graded shell can broaden the distribution of electrons and holes by creating alloyed interfaces, as shown in **Fig. IX (b)**.[66-68] This process results in a redshift of the PL spectra due to an increase in effective size, achieved by extending the electron and hole wavefunctions.[66] Unlike the discrete shell, the formation of a gradient shell at the interface can relieve the lattice strain and reduce the non-radiative defect states at the core/shell interface which enhances the quantum efficiency.[64] Abdellah et al. investigated the electron delocalization and surface passivation of CdSe/$Cd_{1-x}Zn_xSe_{1-y}S_y$ core/graded shell QDs.[66] A gradually increasing redshift in the emission was observed due to extended delocalization of excitons into thick graded shell from 0.6 to 2.3 nm.

3) Metal doping: the metal doping of QDs can effectively control the PL wavelength by introducing new electronic states within the forbidden band, as shown in **Fig. IX (c)**. These new electronic states provide additional pathways for electronic transitions, resulting in a redshift in the PL spectra.[69] Song et al. studied the optical properties of Mn^{2+} and/or Cu^{+}-doped $ZnSe_{1-x}Te_x$/ZnS core/shell QDs.[70] By introducing Cu^{+}, the PL originating from the CB-to-Cu^{+} transition appeared at a longer wavelength compared to the band-edge PL of the $ZnSe_{1-x}Te_x$ core. Additionally, a systematic redshift was achieved by changing the energy level of the $ZnSe_{1-x}Te_x$ core by increasing the Te/Se ratio.

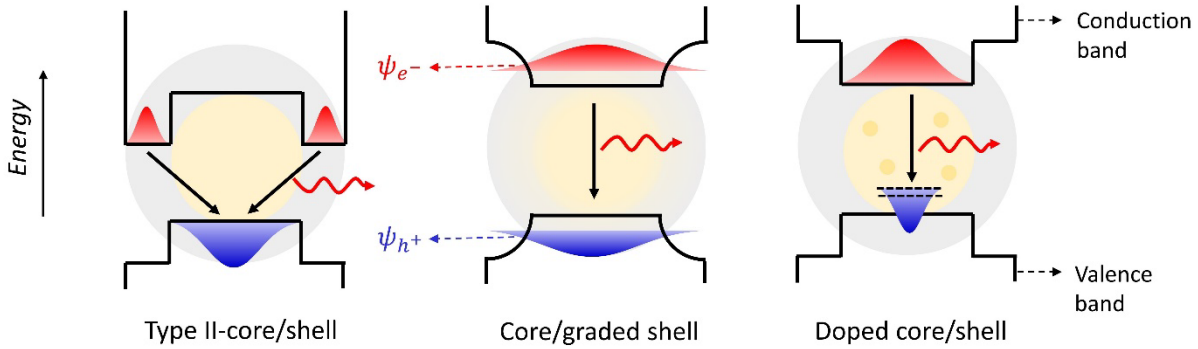

Figure IX. Electronic transition of type-II core/shell QDs, core/graded shell structure, and doped core/shell QDs.

Present work

In this study, I undertook several approaches to explore and achieve a PL redshift of band-edge PL from AIS-based core/sell QDs. The abstract comprises three main chapters, which are summarized as follows:

Chapter 1 "Emission Tuning of $AgInS_2$-Based Core/Shell Semiconductor Quantum Dots with Type-II and Quasi-Type-II Band Alignments"

The attempt to redshift the yellow emission AIS/gallium sulfide (Ga–S) core/shell QDs was made by using type-II or quasi-type II core/shell band alignment. This type-II band structure was realized by replacing the Ga–S shell with Ga–Se, which has a higher valance band potential. When treated with HCl, electronic defect states were removed and the PL QY was improved. This treatment also led to a partial S/Se substitution in the AIS core QDs, increasing the VB potential and narrowing the bandgap. While both these changes contributed to the PL redshift, the band alignment of the final structure was revealed to be quasi type-II. Furthermore, the emission color could be controlled between the yellow to red spectral regions by varying the S/(S+Se) ratio of the gallium sulfide selenide (Ga–S–Se) shell.

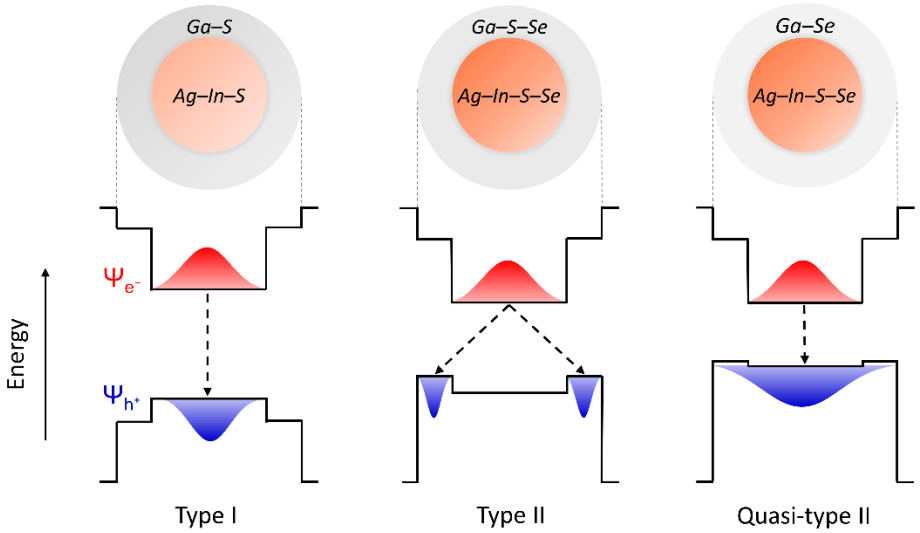

Chapter 2 “Photoluminescence Redshift of $AgInS_2$ Quantum Dots by Employing Shells with Graded Composition”

The redshift of the band-edge PL was achieved without the use of Se by broadening of the exciton wavefunction. When AIS QDs were coated with In–S shells, their band-edge PL shifted to the longer wavelength than those coated with Ga–S shells. However, the AIS/In–S core/shell QDs exhibited a low PL QY and persistent defect PL. To address this, an additional Ga–S shell was formed over the AIS/In–S core/shell QDs. While QDs emitting between 602 nm and 622 nm were obtained, compositional analyses showed a significant decrease in In content, which typically lead to an increased bandgap. The inconsistent results were attributed to the formation of the graded shell. This type of shell broadened the wavefunctions in its region, effectively increasing the effective QD size and leading to a PL redshift.

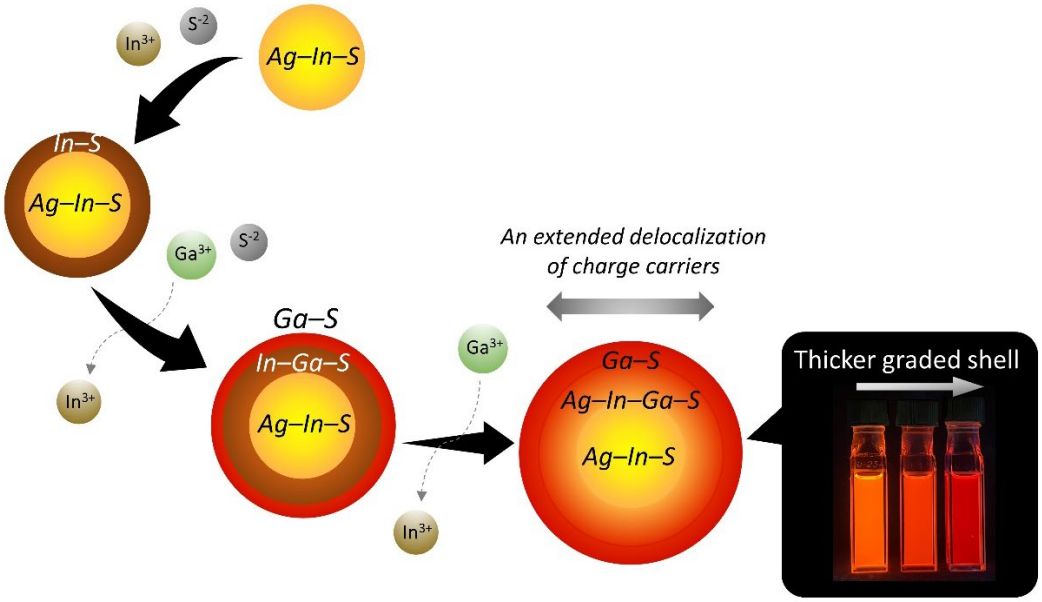

Chapter 3 “Bright Red Luminescence from Ag−In−Ga−S-based Quantum Dots by Introducing Copper”

The effect of introducing Cu into the silver indium gallium sulfide (Ag–In–Ga–S) core QDs was investigated with the aim of redshifting the yellow band-edge emission of AIS. Using a recently developed technique to fabricate uniform Ag–In–Ga–S QDs, a mixture of Cu and Ag sources was rapidly injected into a hot solution containing In, Ga, and S sources. The silver copper indium gallium sulfide (Ag–Cu–In–Ga–S) QDs were synthesized without byproducts, and the red-color PL was obtained after coating with Ga–S shell. Changing the In/Ga ratio of the core QDs strongly affected the PL wavelength, while changing the Ag/Cu ratio did not. This emission was found to be due to the transition between electrons in the conduction band and holes localized at Cu levels. Additionally, the QD-LED fabricated by the Ag–Cu–In–Ga–S/Ga–S core/shell QDs exhibited red electroluminescence (EL) meeting the BT2020 standard.

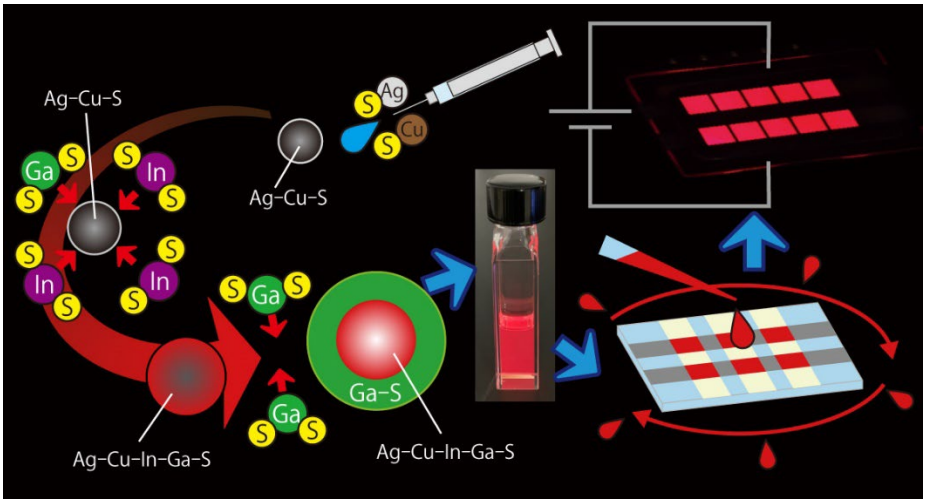

Chapter 1

Emission Tuning of $AgInS_2$-Based Core/Shell Semiconductor Quantum Dots with Type-II and Quasi-Type-II Band Alignments

1.1 Introduction

The 11–13–16 semiconductor QDs such as AIS, $CuInS_2$, and their selenide derivatives are of particular interest as alternatives to highly toxic Cd- and Pb-based QDs.[42-43, 71] Similar to conventional QDs, these alternatives are direct transition semiconductors with high extinction coefficient in the visible to near-infrared region while containing only low toxic elements.[72] However, they exhibit broad emission spectra due to intrinsic defects, leading to low color purity. In 2018, the research group I am affiliated with successfully achieved a spectrally narrow band-edge emission from AIS QDs by a coating of Ga–S shells.[51]

Coating the shell with a wide-bandgap semiconductor is a common approach to surface passivation. The type-I core/shell structure is one of the band alignments where the CB and VB edges of the core are located within the energy gap of the shell. Considering that this structure provides carrier confinement to the core, type-I QDs are emissive and suitable for LEDs and bioimaging applications.[73] The AIS/Ga–S core/shell structure is a type-I structure. This band alignment is used to increase the PL QY without changing the spectral shape (except for a minor redshift due to a variation in the wavefunction). Besides, the AIS/Ga–S core/shell structure is useful for eliminating defective PLs.[51] As with other type-I QDs, the band-edge PL wavelength depends on the bandgap energy of the core after coating with Ga–S shells. The luminescence color, which was yellow for the AIS/Ga–S core/shell QDs, was blueshifted to green by an alloy composition of $AgInS_2$ ($E_{g,\,bulk}$ = 1.8 eV) and $AgGaS_2$ ($E_{g,\,bulk}$ = 2.6 eV). The Ag–In–Ga–S/Ga–S quaternary core/shell QDs exhibited narrow band-edge PL with a PL QY exceeding 50%.[74-75] Conversely, a redshift from AIS was demonstrated by

replacing S with Se to produce Ag–In–Se QDs with a narrow bandgap.[76] In that study, the PL wavelength was tuned between red and near-infrared by the In/Ga ratio, not by the S/Se ratio.

Another form of band alignment is type-II band alignment, in which the CB and VB offset in the same direction at the core/shell heterojunction. Type-II heterojunction semiconductors are frequently used in photocatalysts that allow efficient charge separation. However, they can also be used in luminescent materials when fabricated into core/shell structures. In this case, the staggered band offset causes a strong redshift in the PL wavelength because of charge recombination across the interface.[65, 77] For example, the band alignment of ZnSe/CdSe core/shell QDs was varied from types I to II and finally to quasi-type II by increasing the shell thickness. Thus, the PL wavelength was redshifted to more than 250 nm by growing the CdSe shell up to 1.86 nm.[78] Another example of type-II QDs is Cu_2S/CdS core/shell QDs, whose PL wavelength was varied between 515 and 760 nm by tuning the core size and shell thickness.[65] CdS/ZnSe core/shell QDs are also examples of type-II core/shell structures, which exhibit a redshift in their PL peak by growing the ZnSe shells.[79]

As mentioned above, the band alignment and electronic structure at the interface of core/shell QDs have been intensively investigated for groups 12–16 and 14–16 semiconductors (particularly Cd and Pb chalcogenides),[64] whereas similar studies on the 11–13–16 semiconductors have been hampered by the presence of broad defective PLs. Since the Ga–S shell enabled the band-edge PL of AIS QDs, the possibility of controlling the emission wavelength by band alignment is open. Among the candidate materials, Ga–Se was selected as the new shell material for AIS QDs. Based on recent computational studies of the band positions of AIS and Ga–Se, the VB of the Ga–Se material is expected to be within the bandgap of the AIS core, indicating that this combination forms the type-II band alignment.[80-81] This will cause a redshift of the yellow band-edge PL of AIS/Ga–S QDs, and exhibit red to

near-infrared emissions. AIS QDs were prepared according to a recent report.[51] A mixture of the AIS core QDs, Ga, and Se precursors was heated in oleylamine (OLA), which functions as a solvent and capping ligand, to prepare Ga–Se shells. As expected, a redshifted emission was observed from the AIS/Ga–Se core/shell QDs.[80-81] In addition, attempts were made to tune the band structure between types I and II by controlling the S/(S+Se) ratio of the Ga–S–Se ternary shells.[82] Irregular spectral shapes were obtained upon switching the electronic structures.

1.2 Experimental section

1.2.1 Materials

The following reagents were used as received without further purification: silver(I) acetate (Ag(OAc), 99.9%, Mitsuwa Chemical Co. Ltd.); 1-dodecanethiol (DDT, 98.0%, FUJIFILM Wako Pure Chemical Industries Ltd.); indium(III) acetate ($In(OAc)_3$, 99.99%, Sigma-Aldrich); gallium(III) acetylacetonate ($Ga(acac)_3$, ≥99.99%, Sigma-Aldrich); 1,3-dimethyl thiourea (DMTU, >97.0%, TCI); tri-*n*-octylphosphine (TOP, >85,0%, TCI); selenourea (98%, Acros Organics); and concentrated hydrochloric acid (conc. HCl, 37% v/v, Kishida Chemical Co., Ltd.). Oleylamine (OLA, FUJIFILM Wako Pure Chemical Industries Ltd.) solvent was used after vacuum distillation in the presence of calcium hydride to avoid water.

1.2.2 Synthesis of AIS QDs

The samples were synthesized in a two-necked round-bottom flask with a heating mantle equipped with a proportional–integral–derivative controller. The AIS QDs were synthesized based on a method described in the previous report.[51] Briefly, Ag(OAc) (0.4 mmol, 66.8 mg), $In(OAc)_3$ (0.4 mmol, 166.8 mg), and DDT (1.2 mmol, 300 μL) were mixed with OLA (8 mL) in a 50-mL two-necked round-bottom flask. The mixture was evacuated at

120 ℃ and filled with Ar. After the yellow solution was heated to 140 ℃, 0.4 M DMTU (83.3 mg in 2 mL OLA) was added dropwise at a rate of 4 mL/h. The solution temperature was maintained for another 30 min to grow the QDs. After the reaction, the AIS solution was cooled to room temperature and centrifuged to remove large particles. Excess methanol was added to the supernatant to recover the AIS QDs as a precipitate, which was further purified by repeated dissolution in hexane and precipitation with ethanol, and finally stored in hexane.

1.2.3 Synthesis of AIS/Ga–Se core/shell QDs

The fabrication of the Ga–Se shell was performed based on a reported Ga–S shell coating.[52] The AIS core QDs (30 nmol in terms of particles) were added to an OLA solution containing $Ga(acac)_3$ (0.1 mmol, 36.7 mg) and selenourea (0.1 mmol, 12.3 mg). Under an Ar atmosphere, the solution temperature was gradually increased from 240 to 280 ℃ at a rate of 2 ℃/min and subsequently maintained at 280 ℃ for 15 min to complete shell growth. The core/shell QD solution was cooled to room temperature, and 30 μL of conc. HCl was added to the solution. Thereafter, the solution was rapidly heated to 240 ℃ and maintained at this temperature for 60 min. After cooling to ambient temperature, a large precipitate was removed by centrifugation. Finally, the AIS/Ga–Se core/shell QDs were purified by precipitation with ethanol and dispersed in a hexane/TOP mixture (50/50 in volumetric ratio).

1.2.4 Synthesis of AIS/Ga–S–Se core/shell QDs

The AIS core QDs (30 nmol in terms of particles) were added to an OLA solution containing $Ga(acac)_3$ (0.1 mmol, 36.7 mg), DMTU, and selenourea; the amounts of DMTU and selenourea are summarized in **Table 1-1**. The mixture was treated using the same procedure as that for the synthesis of Ga–Se shells. The obtained AIS/Ga–S–Se core/shell QDs were denoted by AIS/Ga–S–Se-*X*, where *X* indicates the percentage of Se (Se/(S+Se)) mixed in the raw material and was varied at 30, 20, and 10. For comparison, the AIS/Ga–S

QDs were synthesized using $Ga(acac)_3$ (0.1 mmol, 36.7 mg) and DMTU (0.1 mmol, 10.4 mg) according to a report.[52]

Table 1-1. Lists of precursors for the fabrication of Ga–S–Se alloy shells.

Sample	Percentage of selenium (Se/(S+Se))	DMTU/mmol	Selenourea/mmol
AIS/Ga–S–Se-10	10%	0.05	0.1
AIS/Ga–S–Se-20	20%	0.075	0.05
AIS/Ga–S–Se-30	30%	0.075	0.0375

1.2.5 Instrumental

Ultraviolet–visible (UV–vis) and PL spectra were recorded using a UV–vis spectrometer (Jasco, V-670) and a spectrofluorometer (Jasco, FP-8600), respectively. The PL QY was obtained as the absolute quantum yield using a spectrofluorometer (Hamamatsu, PMA-12) equipped with an integrating sphere. Chloroform was used as the solvent for samples and a blank, which were placed in a dedicated quartz cuvette. The X-ray Diffraction (XRD) patterns of the samples were recorded using a powder X-ray diffractometer (Rigaku, Japan, SmartLab). The morphologies of the QDs were examined by transmission electron microscopy (TEM, Hitachi, Japan, H-7650) at an acceleration voltage of 100 kV. The elemental compositions of the QDs were determined by inductively coupled plasma atomic emission spectroscopy (ICP–AES; Shimadzu, Japan, ICPS-7510PL). PL decay curves were obtained using a time-correlated single-photon counting setup (Hamamatsu, Japan, Quantaurus-Tau).

1.3 Results and discussion

1.3.1 Formation of AIS/Ga–Se core/shell QDs

Figures 1-1 (a, b) show the TEM images of the AIS core, AIS/Ga–Se core/shell QDs, respectively. An increase in particle size, from 3.1 ± 0.6 to 5.2 ± 1.3 nm, was observed after heat treatment with the Ga–Se precursors, indicating the formation of a Ga–Se shell. The UV–vis and PL spectra of the corresponding samples are shown in **Fig. 1-2**. The AIS core QDs (blue curves) exhibited an absorption edge at ca. 700 nm and broad PL (FWHM = 0.37 eV) at 789 nm (1.57 eV), typical of defect emissions.[51] After the Ga–Se shell formation (green curves), a narrower PL peak (FWHM = 0.19 eV) was observed on the short wavelength side (681 nm, 1.82 eV), suggesting the passivation of surface defects during the Ga–Se shell coating. Notably, this emission wavelength was approximately 100 nm longer than the band-edge PL of the AIS/Ga–S QDs (572 nm (2.17 eV), subsequently mentioned). **Figure 1-3** shows the PL decay profiles of the AIS core (blue) and AIS/Ga–Se core/shell QDs (green). The decay profiles were fitted to a single or biexponential equation. The latter is described as equation 1-1:

$$I(t) = A_1 \exp\left(-\frac{t}{\tau_1}\right) + A_2 \exp\left(-\frac{t}{\tau_2}\right) \quad (1\text{-}1)$$

where I(t) is the PL intensity at time (t), A_1 and A_2 are the amplitudes, and τ_1 and τ_2 are their lifetimes. The amplitude and lifetime of each component are summarized in **Table 1-2**. The decay curve of the AIS core QDs was well fitted to a single exponential equation to yield a lifetime of 866.0 ns, which was assigned to the emission of exciton recombination via the defect state.[51] After passivation by the Ga–Se layer, the average lifetime significantly decreased to 127.8 ns (25.7 and 162.6 ns) at the peak wavelength of the newly generated emission. The seven-fold decrease in the average lifetime and the similarity of each lifetime

component to those of the AIS/Ga–S core/shell QDs indicated a change in the emission mechanism from the defect state to the band-edge or similar transitions.

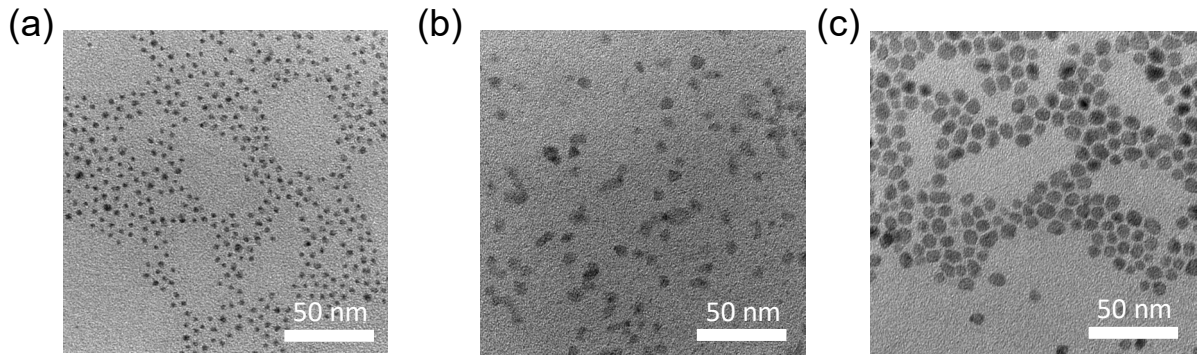

Figure 1-1. TEM images of the (a) AIS core, (b) AIS/Ga–Se core/shell, and (c) AIS/Ga–Se core/shell QDs after HCl treatment.

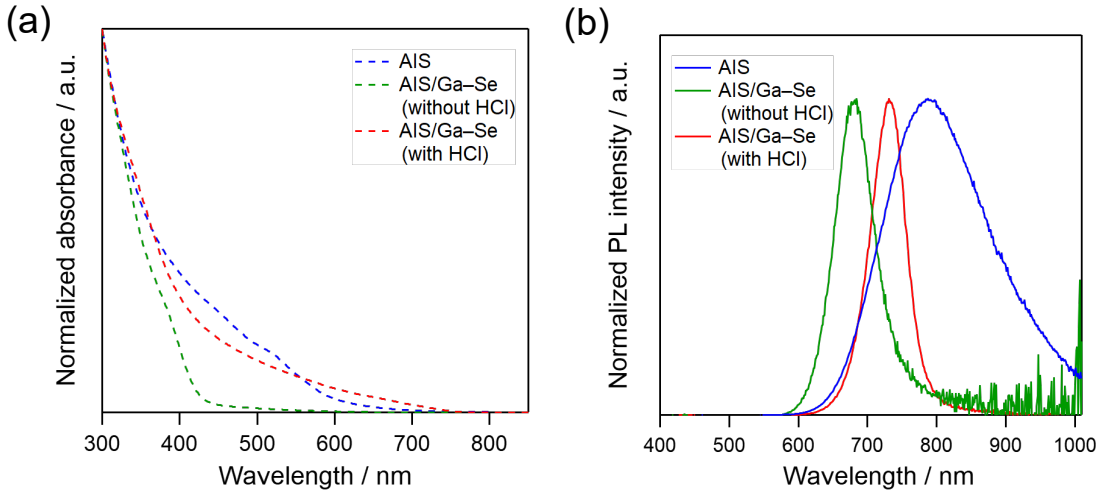

Figure 1-2. (a) UV–vis absorption and (b) PL spectra of the AIS core, AIS/Ga–Se core/shell, and AIS/Ga–Se core/shell QDs with HCl treatment.

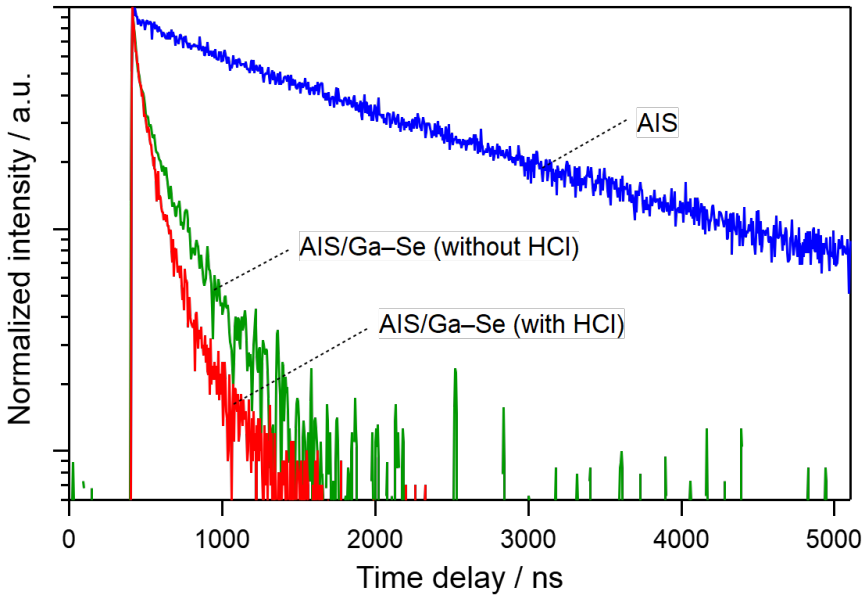

Figure 1-3. PL decay curves of the AIS core and AIS/Ga–Se core/shell prior to and after HCl treatment.

Table 1-2. PL decay components of the AIS core and AIS/Ga–Se core/shell prior to and after HCl treatment.

Sample	Observation position	τ_1/ns	A_1	τ_2/ns	A_2	χ^2	τ_{avg}[a]
AIS	789 nm (1.57 eV)	866.0	848.6	–	–	1.18	866.0
AIS/Ga–Se							
(without HCl)	681 nm (1.82 eV)	25.7	632.0	162.6	292.8	1.05	127.8
(with HCl)	733 nm (1.69 eV)	32.2	723.0	120.0	200.9	1.06	76.9

[a] Intensity average calculated by $\sum_i A_i\tau_i^2 / \sum_i A_i\tau_i$

Figure 1-4 (blue curve) shows the XRD pattern of the AIS core QDs, demonstrating the presence of a tetragonal $AgInS_2$ (ICSD 070-5629). Considering that the XRD peak positions were identical after the formation of the Ga–Se shells (green), the redshift appeared to have been because of the indirect transition between the core and shell caused by the type-II band alignment. Patterns consistent with Ga–Se (indicating GaSe, Ga_2Se_3, or in-between) were not

observed; therefore, the Ga–Se shells were amorphous. The PL QY decreased from the AIS cores (70%) to 1% after forming the Ga–Se shells because of nonradiative transition via defect sites in the Ga–Se shell. The composition analyses (listed in **Table 1-3**) showed that the Ag:In:S ratios of the core QDs mostly correlated with the stoichiometric ratio of $AgInS_2$. However, after forming the Ga–Se shells, the S ratio decreased from the ideal Ag:In:S = 1:1:2, which conflicted with the XRD results. It was assumed that certain S atoms at the core/shell interface were replaced by Se atoms to form an amorphous intermediate layer of Ag–In–S–Se, which was invisible as XRD peak positions but broadened the signals by reducing the crystalline length of the AIS phase.

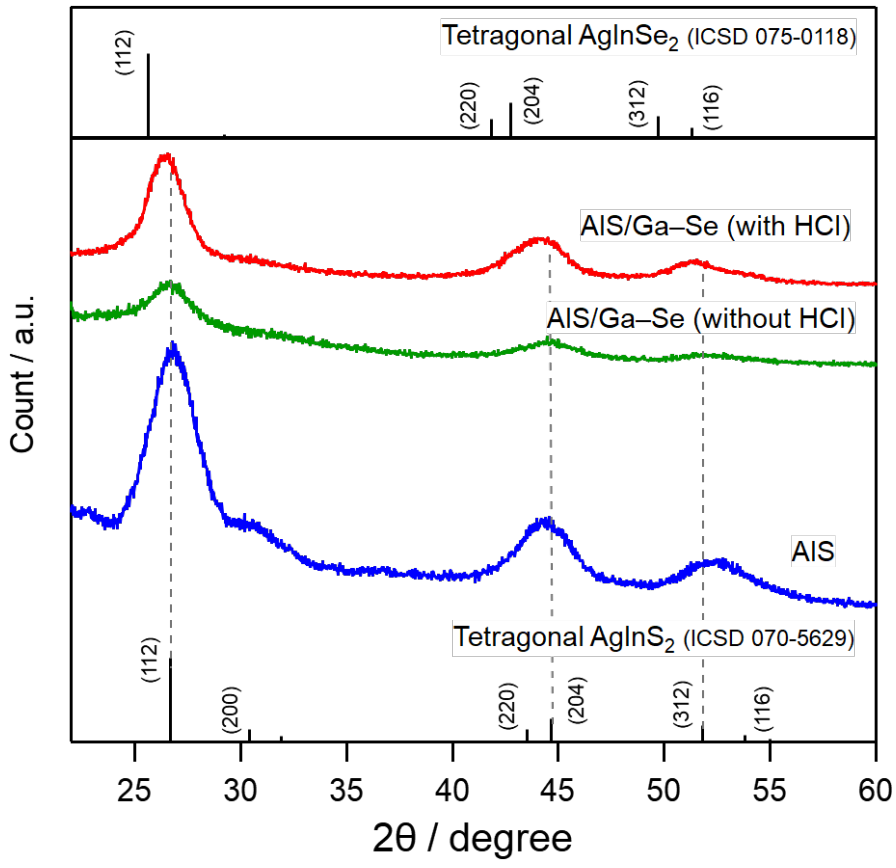

Figure 1-4. XRD patterns of the AIS core and AIS/Ga–Se core/shell prior to and after HCl treatment.

Table 1-3. Composition ratios (Ag = 1.00) of the AIS core and AIS/Ga–Se core/shell QDs determined from the ICP–AES analyses of the purified samples.

Sample	Composition ratios (Ag = 1.00)				
	Ag	In	S	Ga	Se
AIS	1.00	1.09	2.30	–	–
AIS/Ga–Se					
(without HCl)	1.00	1.28	0.88	5.02	8.96
(with HCl)	1.00	1.22	0.46	0.96	3.01

The HCl treatment has been recently revealed to improve the PL QY of QDs with Ga–S shells.[83] As anticipated, the PL QY was recovered to 25% without a significant change in the spectral width. The PL wavelength redshifted by 51 nm (733 nm, 1.69 eV), and a similar redshift was observed for the absorption spectrum (**Figs. 1-2 (a, b)**, red). The recent study showed that the HCl treatment removes impurities derived from imperfectly decomposed raw materials and helps to eliminate the electronic trap states at the core/shell boundary and in the shell body.[75] Additionally, the effect of surface passivation by chloride ions has been reported for ZnSe shells, which is also a Se compound.[84]

The change in the shell property was also evident from the apparent change in the particle shape to a more solid and spherical shape after HCl treatment (see in **Figs. 1-1 (b, c)**). Considering that the Ga and Se contents significantly reduced, just as the HCl treatment decreased the Ga and S contents of the Ga–S shell-coated QDs, the reformulation of the shell body and core/shell interface was considered as a major reason for the improved PL QY. Simultaneously, the S content further decreased, and each XRD peak shifted to a smaller angle, suggesting an alloying process with $AgInSe_2$.[76, 85] This indicated that the S in the AIS core and the Se in the expected intermediate Ag–In–S–Se layer mixed, forming an alloyed Ag–In–S–Se core and redshifting the emission.

After the posttreatment with HCl, the decay time reduced further (**Fig. 1-3**, red). However, this result contradicted the increase in PL QY caused by the treatment (from 1% to 25%) because the shortening of the lifetime typically indicated an increase in the nonradiative transition, which lowered the PL QY. Therefore, it is reasonable to consider that the treatment altered the luminescence mechanism. For example, the spatial overlap of electrons and holes in the band alignments of types I and II differed, which affected the charge recombination kinetics. From this viewpoint, I can speculate that the band alignment changed from type II to the quasi-type II after the HCl treatment because of a reduction in the bandgap of the cores by alloying with $AgInSe_2$ (**Fig. 1-5**). Another possible mechanistic change is the contribution of trap states that occasionally increased the luminescence lifetime (reversible trapping). In the reversible trapping mode, excitons are in thermodynamic equilibrium between the band-edge and trap levels, and the long-lived trapped carriers increase the lifetime of the band-edge PL.[86]

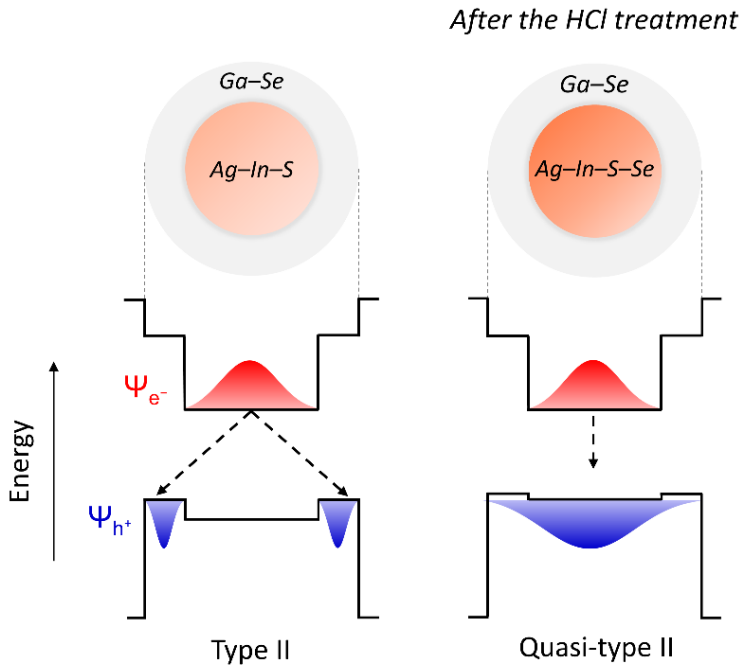

Figure 1-5. Schematics of the electronic structure and carrier wavefunctions in the /Ga–Se core/shell QDs after HCl treatment.

To determine the extent to which the band alignment (types I and II) and core alloying ($AgInS_2$ and $AgInSe_2$) contributed to the redshift in the luminescence, the XRD peak positions of the (112) plane after HCl treatment (26.4°) were examined. Considering the (112) peak positions of $AgInS_2$ (26.7°) and $AgInSe_2$ (25.6°), the percentage of Se substitution was calculated following Vegard's rule, as described below[87]

$$2a_{AgInS_ySe_{(2-y)}} = y\left(a_{AgInS_2}\right) + (2-y)\left(a_{AgInSe_2}\right), \qquad (1\text{-}2)$$

where each a represents the lattice parameter of $AgInS_ySe_{(2-y)}$, $AgInS_2$, and $AgInSe_2$, and y represents the ratio of S atoms in the total chalcogens in the core QDs, S/(S+Se). Following this calculation, the percentage of Se in the alloy Ag–In–S–Se core was 44% (y = 1.1). The bulk bandgap values of $AgInS_2$ and $AgInSe_2$ were 1.87 and 1.24 eV, respectively. Therefore, the redshift of the 44% Se Ag–In–S–Se was calculated to be 0.28 eV if the bandgap of the alloy was linearly dependent on its composition. This was significantly smaller than the observed redshift (0.48 eV, from 572 to 733 nm) of the Ga–Se-coated, HCl-treated AIS QDs, suggesting the partial contribution of the band alignment effect.

1.3.2 Tuning emission of AIS/Ga–S–Se core/shell QDs

To investigate the physicochemical aspects of the selenide shells and to demonstrate continuous color tuning by this system, I fabricated Ga–S–Se ternary shells. **Figure 1-6** shows the absorption and PL spectra of the AIS/Ga–S–Se core/shell QDs with different Se contents after the HCl treatment. As the Se/(S+Se) ratio increased, the absorption onset redshifted, and the PL spectra simultaneously redshifted. The spectral widths of the 10%, 20%, and 30% Se samples were unexpectedly broadened. These results suggested the presence of multiple emission levels, i.e., in the core and between the core and shell, owing to the transition of the band alignment from types I to II.

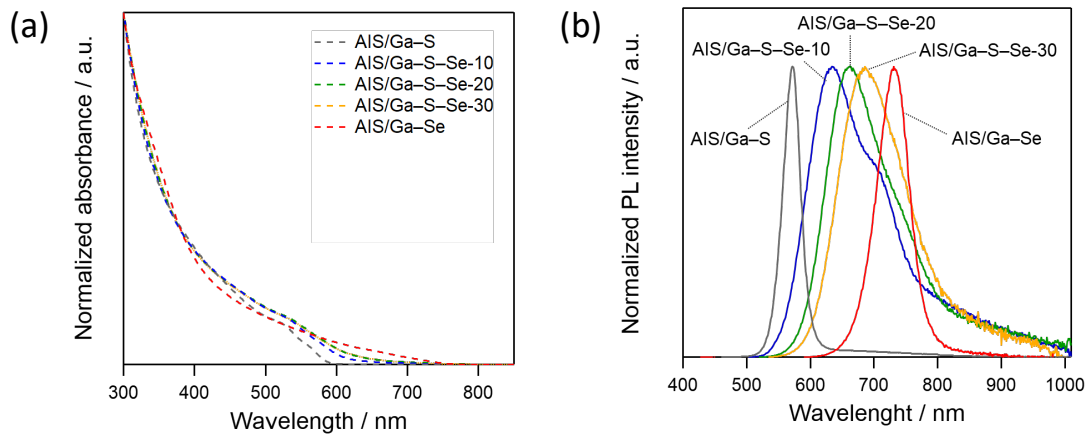

Figure 1-6. (a) UV–vis and (b) PL spectra of the AIS/Ga–S, AIS/Ga–Se, and AIS/Ga–S–Se core/shell QDs whose shells were prepared using different S/Se precursor ratios.

Figure 1-7 shows the XRD patterns of the AIS/Ga–S, AIS/Ga–Se, and AIS/Ga–S–Se QDs with different Se contents. Although the reasonable increases in particle size were observed after the formation of Ga–S–Se shells (summarized in **Fig. 1-8**), the gallium sulfide and gallium selenide phases were undetectable in all the samples, indicating that they were amorphous or that these crystalline lengths were too insufficient to be detected by XRD. In all cases, the spectral shape was that of the tetrahedral $AgInS_2$ or its alloy with $AgInSe_2$. However, the magnitudes of the peak shifts for the Ga–S–Se-shelled QDs were smaller than those of the Ga–Se-shelled QDs, indicating that the substitution of S in the core was limited. The chemical compositions of the core/shell QDs also indicated that the residual S content of the Ga–S–Se-shelled QDs exceeded that of the Ga–Se-shelled QDs (**Table 1-4**). Contrarily, the S/Se substitution at the core/shell boundary, i.e., the formation of the Ag–In–S–Se intermediate layer, appeared to be inevitable as long as Se was used.

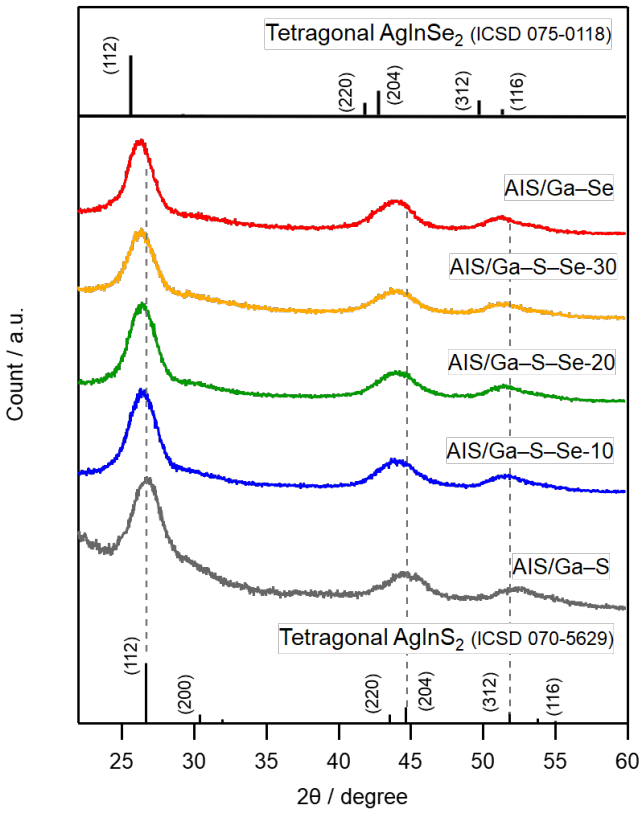

Figure 1-7. XRD patterns of the AIS/Ga–S, AIS/Ga–Se, and AIS/Ga–S–Se core/alloy shell QDs whose shells were prepared using different S/Se precursor ratios (10%–30% Se).

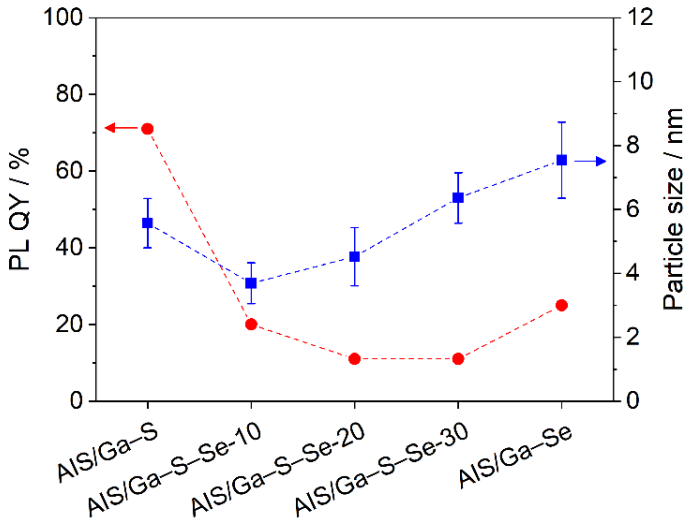

Figure 1-8. PL QY and average particle sizes of AIS/Ga–S, AIS/Ga–Se, and AIS/Ga–S–Se core/shell QDs with different Se contents in the shells. Bars for the particle size indicate the standard deviations.

Table 1-4. Composition ratios (Ag = 1.00) of AIS/Ga–S, AIS/Ga–S–Se, and AIS/Ga–Se core/shell QDs determined from the ICP–AES measurements of the purified samples.

Sample	Elemental composition ratios (Ag = 1.00)				
	Ag	In	S	Ga	Se
AIS/Ga–S	1.00	0.63	2.50	0.69	-
AIS/Ga–S–Se-10	1.00	0.86	1.68	0.55	0.73
AIS/Ga–S–Se-20	1.00	0.88	1.39	0.51	1.05
AIS/Ga–S–Se-30	1.00	0.92	1.11	0.51	1.17
AIS/Ga–Se	1.00	1.22	0.46	0.96	3.01

Figure 1-9 shows the PL decay curves obtained for the AIS/Ga–S, AIS/Ga–Se, and AIS/Ga–S–Se core/shell QDs with different Se contents (10%–30%). The decay curves were well fitted with the biexponential equation, and the amplitude and decay time components are listed in **Table 1-5**. Interestingly, the PL lifetimes of the Ga–S–Se-shelled QDs were significantly longer than those of the AIS/Ga–S QDs and even longer than those of the AIS/Ga–Se QDs. Typically, the PL lifetime of type-II core/shell QDs is longer than that of their type-I counterparts. In addition, the PL QY of the Ga–S–Se-shelled QDs was lower than that of the AIS/Ga–Se and AIS/Ga–S QDs (**Fig. 1-8**). Therefore, from the PL spectrum, lifetime variations, and PL QY, I can speculate that the AIS QDs with a Ga–S–Se alloyed shell exhibited a full type-II band alignment, whereas those with a Ga–Se shell exhibited a quasi-type-II structure.

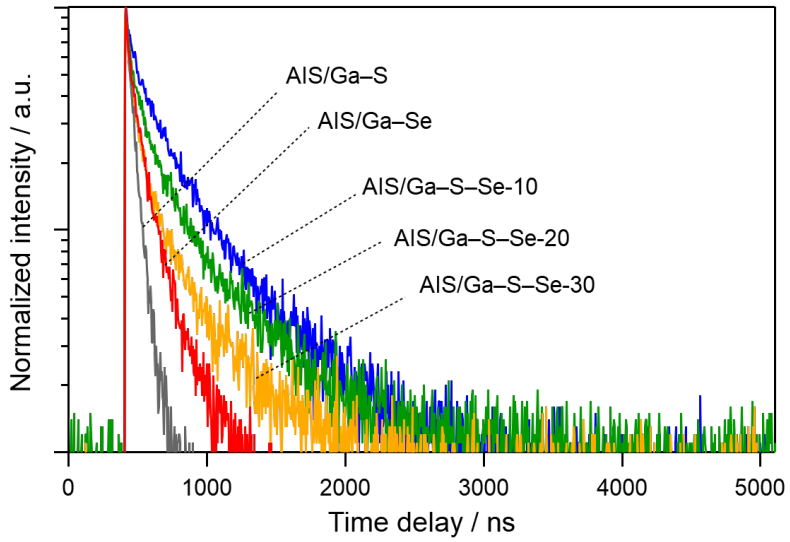

Figure 1-9. PL decay curves of AIS/Ga–S, AIS/Ga–Se, and AIS/Ga–S–Se core/shell QDs with different ratios of S and Se precursors.

Table 1-5. PL decay components of the AIS/Ga–S, AIS/Ga–Se, and AIS/Ga–S–Se core/shell QDs prior to and after HCl treatment.

Sample	Observation position	τ_1/ns	A_1	τ_2/ns	A_2	χ^2	τ_{avg}[a]
AIS/Ga–S	572 nm (2.17 eV)	43.5	949.4	132.7	113.7	1.03	67.3
AIS/Ga–S–Se-10	631 nm (1.97 eV)	94.7	503.9	438.2	412.1	1.17	366.4
AIS/Ga–S–Se-20	654 nm (1.90 eV)	72.3	637.0	422.0	275.5	1.19	322.8
AIS/Ga–S–Se-30	685 nm (1.81 eV)	57.1	687.3	363.9	184.5	1.25	250.6
AIS/Ga–Se	733 nm (1.69 eV)	32.2	723.0	120.0	200.9	1.06	76.9

[a] Intensity average calculated by $\sum_i A_i\tau_i^2 / \sum_i A_i\tau_i$

Considering the experimental data, the AIS QDs coated with Ga–S–Se shells exhibited dual-mode emission, which is typical for QDs whose band alignment is in the boundary region between types I and II. Overall, the luminescence color could be tuned by controlling the composition of S and Se in the Ga–S–Se shells. The XRD peaks slightly shifted to smaller angles, suggesting that the S in the core was replaced with Se. According to Vegard's rule described in the previous chapter, the percentages of Se substitution in the 10%, 20%, and 30% Se shelled AIS QDs were calculated to be 11%, 22%, and 33%, respectively. These percentages corresponded to redshifts of 56, 138, and 208 meV with respect to the band-edge emission of the AIS/Ga–S core/shell QDs, respectively, if the alloy bandgap was linearly dependent on its composition. However, the observed redshifts in the PL spectra of the AIS/Ga–S–Se core/shell QDs were 203, 272, and 358 meV in the same order, which significantly exceeded those expected from the alloy composition, indicating the strong contribution of the type-II band alignment (**Fig. 1-10**). These results were consistent with the lengthening of PL lifetimes typically observed in type-II core/shell QDs. Therefore, the PL of the AIS/Ga–S–Se core/shell QDs appeared to have been generated by the transition between the electrons in the core and the holes in the shell. Contrarily, with a further increase in the Se content, the alloying of the core QDs became more significant. This raised the VB level of the core to the same level as that of the shells and broadened the wavefunction of the holes so that it exists between the core and shell. Owing to an increase in the spatial overlap of the wavefunctions between the electrons and holes, the PL lifetime of the Ga–Se-shelled QDs decreased to the level of their Ga–S-shelled counterparts, and the PL QY was slightly recovered because the trap states on the surface of the shell became insignificant. This study improves the understanding of the surface passivation mechanism of AIS-based QDs, particularly in terms of band alignment.

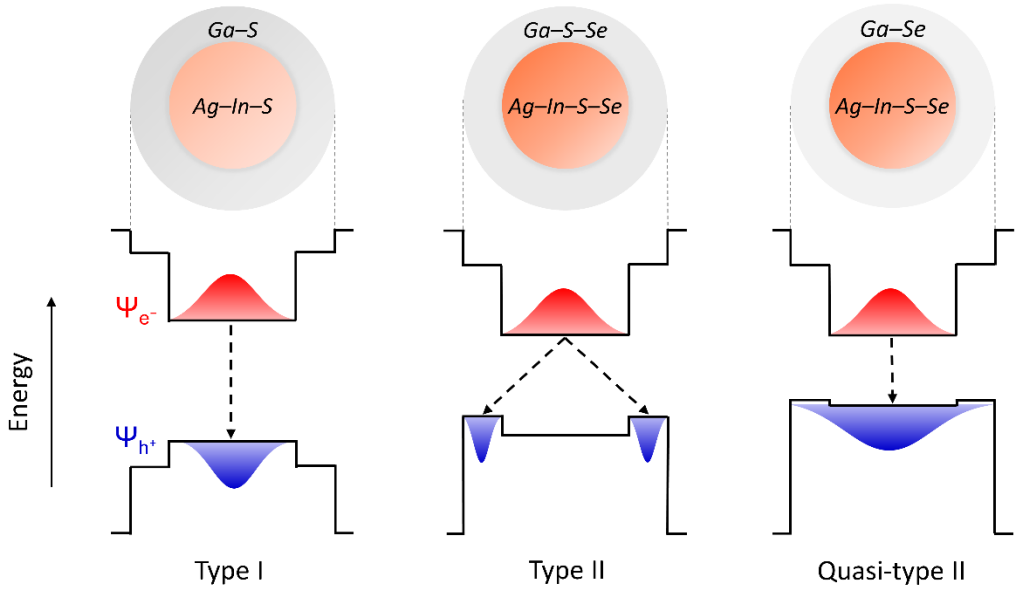

Figure 1-10. Development of the electronic structure and carrier localization in AIS/Ga–S–Se QDs.

1.4 Summary

Here, AIS/Ga–Se core/shell QDs were successfully synthesized in the red-emission region. After the heat treatment with Ga–Se precursors, an increase in the diameter size from 3.1 to 5.2 nm was observed, and a narrower PL spectrum appeared owing to surface passivation by the Ga–Se shell. Owing to the staggered bandgap alignment of the core and shell, a substantial redshift of the PL emission was observed. The long PL lifetime of this emission indicated the presence of indirect transition due to the type-II band alignment. In addition, the PL QY of the core/shell QDs increased to 25% after the heat treatment with HCl. I speculated that the electronic trap states at the core/shell interface and in the shell body were reduced after coating with the Ga–Se shell. However, the shortening of the PL lifetimes occurred after the HCl treatment, suggesting a change in the electronic transition mechanism. The XRD results indicated the S/Se alloying of the core; therefore, the band alignment shifted from type II to quasi-type II due to the high energy shift in the VB of the core was the reason

for these changes in optical properties. When the shell was made into a Ga–S–Se alloy, a continuous shift in the PL wavelength between yellow and red was observed, and the dual-mode emission was observed in certain alloy compositions.

Chapter 2

Photoluminescence Redshift of $AgInS_2$ Quantum Dots by Employing Shells with Graded Composition

2.1 Introduction

Semiconductor QDs have been intensively studied owing to their distinctive optical and electronic properties that differ from the bulk material.[19, 88-89] Recently, group 11–13–16 semiconductor QDs such as AIS have gained attention as environmentally benign alternatives.[90-91] These QDs exhibited reasonably high PL intensity, while their PL was composed of spectrally broad defect emission. The narrow-band emission was achieved when the AIS QDs were coated with gallium sulfide (Ga–S) shells.[51-52] Furthermore, a blue-shift of the band-edge emission was achieved by alloying of AIS ($E_{g,\ bulk}$ = 1.8 eV) and $AgGaS_2$ ($E_{g,\ bulk}$ = 2.6 eV) to increase the bandgap of the core, resulting in PL in the green region.[75, 92-93]

In recent years, advances in tailoring the emission properties of QDs have made them a promising candidate for LEDs.[60-61] In particular, fluorophores for the three primary colors, blue, green, and red, are needed for display applications.[58-59] Common strategies for the wavelength tuning of QDs is doping with transition metals[62-63] or changing the elemental composition of alloyed emissive core.[43, 94] Alternatively, the redshift of AIS-based QDs can be achieved by controlling the charge delocalization within the core/shell structure by using an electronic structure known as type II, where the valence and conduction-band-edge potentials are offset in the same direction. In Chapter 1, the coating of the Ga–Se shells on AIS cores was described. A PL redshift was observed owing to a specific electronic structure known as the type II core/shell structure.[95]

The core/graded shell architecture offers an alternative method to achieve PL redshift.[35] This design has been used to tune the optical properties of binary semiconductor QDs, like CdSe, by creating shells with a graded composition. This gradient typically results in an average composition represented as $Cd_{1-x}Zn_xSe_{1-y}S_y$, with a higher proportion of ZnS at the outer edge.[66-68] When shells have a graded composition, the distribution of electrons and holes becomes broader compared to QD that have a distinct compositional gap between the core and shell (discrete shell). This effect results in a redshift of the PL spectra owing to an increase in effective size.[66] Therefore, changing the compositional gradient and the thickness of the graded part allow systematic PL shifts. In addition, compared to the discrete shell, the graded shell has less lattice strain, resulting in a decrease in the nonradiative transition and an increased PL QY.[67, 96]

At present, the effect of the graded shell on the optical property for AIS-based QDs is not yet fully understood. However, research group I affiliated with have occasionally observed an unexpected redshift in the PL of silver indium gallium sulfide (Ag–In–Ga–S)/Ga–S core/shell QDs.[92] That is, the wavelength of the band-edge PL was longer than that of AIS/Ga–S (580–590 nm)[51-52], whereas the bandgap of Ag–In–Ga–S should, theoretically, be larger than that of AIS[75, 92-93]. I hypothesize that the abnormal wavelength shift that I observed previously is due to the graded structure that is spontaneously generated by the synthesis condition. In this work, AIS core is initially coated with an indium sulfide (In–S) shell, which has a narrower bandgap (2.2 eV) than Ga–S (2.8 eV), with the aim of forming an In–Ga–S graded shell. The core/shell QDs are then reacted with gallium(III) diethyldithiocarbamate ($Ga(DDTC)_3$), followed by a $GaCl_3$ treatment to form Ga–S outer shell. Whereas the red-color PL was obtained, compositional and X-ray diffraction (XRD) analyses

suggested that, within a series of synthesis operations, the QDs underwent complicated structural changes. These changes are discussed in relation to changes in PL properties, with the formation of graded shells in mind.

2.2 Experimental section

2.2.1 Materials

Indium(III) chloride ($InCl_3$, 99.9%) and elemental S (99%) were purchased from Mitsuwa Chemical Co. Ltd. Gallium(III) chloride anhydrous ($GaCl_3$, 98.0%) was purchased from TCI (Tokyo Chemical Industry Co., Ltd.). Diethylammonium *N,N*-diethyldithiocarbamate (DEA–DDTC, ⩽100%) was purchased from FUJIFILM Wako Pure Chemical Industries Ltd.).

Silver(I) acetate (Ag(OAc)), Indium(III) acetate ($In(OAc)_3$), 1,3-dimethyl thiourea (DMTU), and 1-dodecanethiol (DDT) were purchased from the same suppliers mentioned in Chapter 1 (1.2.1). In addition, oleylamine (OLA, FUJIFILM Wako Pure Chemical Industries Ltd.) was purified in a similar manner as described in Chapter 1 (1.2.1).

2.2.2 Synthesis of gallium(III) *N,N'*-diethyldithiocarbamate

The synthesis of gallium(III) *N,N'*-diethyldithiocarbamate ($Ga(DDTC)_3$) was performed based on the methodology detailed in a previous study.[75] Initially, in a N_2 glovebox, a solution of $GaCl_3$ in dehydrated toluene was prepared, to which was added a toluene solution containing three equivalents of DEA–DDTC. The mixture was reacted for 1 h with rigorous stirring. Upon completion of the reaction, the solvent was removed by a rotary evaporator, and the white powder was further dried under vacuum (100 Pa) for an additional hour. The crude product was purified by re-crystallization in chloroform over a period of 12 h. The filtered product was then dried in a vacuum at 60 °C, and a white powder of $Ga(DDTC)_3$ was obtained in 82% yield. It was stored in a desiccator cabinet filled with N_2 before use. The composition of the product was confirmed by an ICP–AES to be Ga:S = 1:6.2.

2.2.3 Synthesis of AIS QDs

AIS core QDs were prepared in a similar manner as described in Chapter 1 (1.2.2).

2.2.4 Preparation of AIS/In–S core/shell QDs

The synthesis of the In–S shell was performed based on the reported procedure for In_2S_3 nanoparticles with optimization.[97] $InCl_3$ (0.1 mmol) and 0.4 equivalents of elemental S were mixed with 10 mL of OLA. The reaction mixture was then heated to 80 °C under vacuum. After filling with Ar, the solution temperature was increased to 120 °C, and the AIS QD solution (30 nmol in terms of particles) was injected. The temperature of the solution was increased to 180 °C and maintained for 30 min to allow the In–S shell to grow. Upon completion of the reaction, the solution was cooled and then evacuated at 200 °C to remove unreacted S precursors. After cooling to room temperature, the QDs were purified using ethanol and chloroform. Finally, the sample was dissolved in 1 mL of hexane.

2.2.5 The formation of Ga–S outer shell

0.1 mmol of $Ga(DDTC)_3$ and 10 mL of OLA were placed in a 50 mL round bottom flask. The mixture was heated under vacuum at 80 °C for 10 min and then filled with Ar. The temperature controller was set to 230 °C. To prevent Ostwald ripening during the temperature rise, the AIS/In–S core/shell QDs were injected when the solution temperature reached 160 °C. The temperature was further increased from 230 to 280 °C at a rate of 2°C/min. Separately, 0.1 mmol of $GaCl_3$ was dissolved in 1 mL of OLA and loaded into a gas-tight syringe. When the temperature reached 280 °C, the $GaCl_3$ solution was injected. Heating was continued for another 30 min. After the reaction was completed, the same purification process as for In–S-coated QDs was applied. Finally, the QDs were dissolved in 1 mL of hexane and stored in a freezer.

2.2.6 Instrumental

The instruments for material characterization were carried out as described in Chapter 1 (1.2.5).

2.3 Results and discussion

2.3.1 Formation of AIS/In–S core/shell QDs

Figures 2-1 (a, b) display the TEM images of the AIS core QDs, both before and after heat treatment with $InCl_3$ and elemental S. It is noteworthy that the particle size increased from 4.2±0.4 to 5.3±0.7 nm, while maintaining its spherical shape, suggesting the formation of In–S shells. Prior to the reaction, elemental analysis of the QDs by ICP–AES revealed a compositional ratio of Ag:In:S of approximately equal to 1:1:2 (see **Table 2-1** for details). However, post-reaction analysis of purified samples showed a significant increase in the proportions of In and S. Specifically, the ratios of In and S relative to Ag increased by 0.73 and 1.48, respectively. This indicates the formation of In–S layer with an excess of S when compared to the stoichiometric ratio of In_2S_3.

Figure 2-2 shows the XRD patterns of the QDs, which are the same samples analyzed in the previously presented TEM images. $AgInS_2$ primarily exhibits two crystal phases: the tetragonal, often referred to as the chalcopyrite structure, and the orthorhombic, similar to the wurtzite structure. The AIS core QDs are biased toward the tetragonal phase, although the signals are weak due to their small crystal size. After coating with In–S, the tetragonal phase persisted, with no discernible peaks associated with In_2S_3. This finding suggests that the In–S shell is amorphous, similar to the attributes of Ga–S shells reported in recent studies.[51-52]

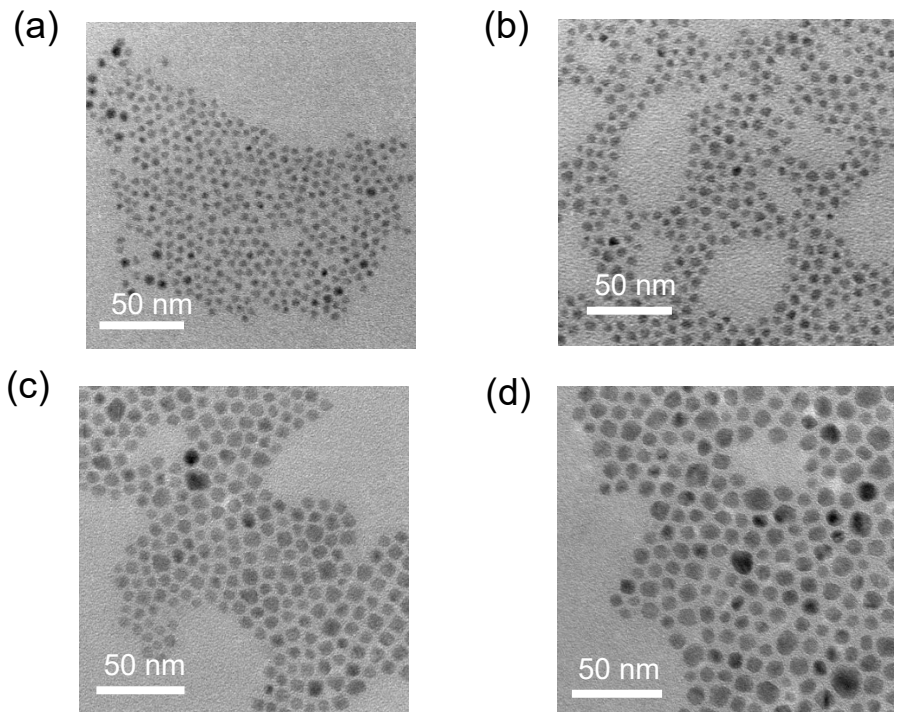

Figure 2-1. TEM images of (a) AIS core, (b) AIS/In–S core/shell, and AIS/Ag–In–Ga–S/Ga–S core/graded shell QDs (c) before and (d) after $GaCl_3$ treatment.

Table 2-1. Elemental compositions of AIS core, AIS/In–S core/shell, and AIS/Ag–In–Ga–S/Ga–S core/graded shell QDs before and after $GaCl_3$ treatment.

Sample	Composition ratios (Ag = 1.00)			
	Ag	In	S	Ga
AIS	1.00	0.93	1.99	–
AIS/In–S	1.00	1.66	3.47	–
AIS/Ag–In–Ga–S/Ga–S				
(Before $GaCl_3$ treatment)	1.00	1.00	4.11	1.54
(After $GaCl_3$ treatment)	1.00	0.75	2.18	0.35

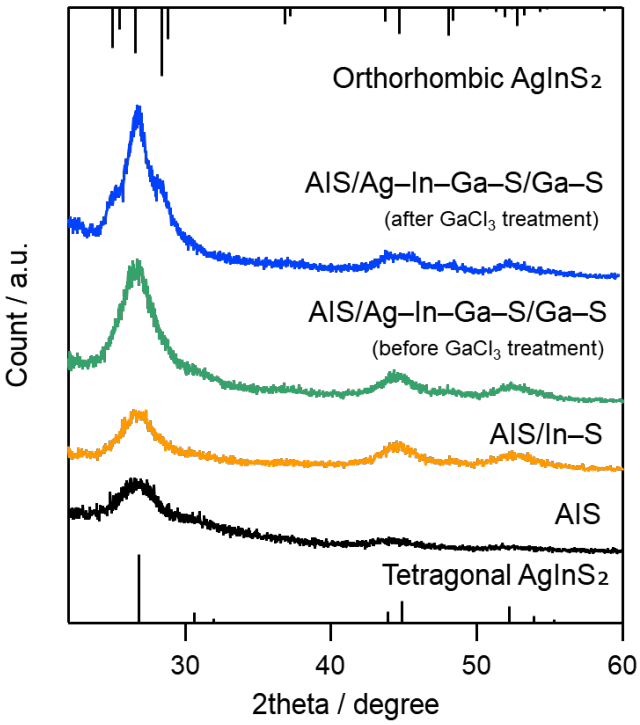

Figure 2-2. XRD patterns of AIS core, AIS/In–S, and AIS/Ag–In–Ga–S/Ga–S core/graded shell QDs before and after $GaCl_3$ treatment. The bars at the top and bottom of the graph represent the reference patterns for the orthorhombic (ICDD 075-6150) and tetragonal $AgInS_2$ (ICDD 077-6632), respectively.

Figure 2-3 presents the absorption and PL spectra of the AIS core (displayed in the black curve) and AIS/In–S core/shell (the yellow curve) QDs. After introduction of amorphous In–S shells, an obvious blue shift (by 140 nm) in the absorption tail was observed, indicating a significant reduction in surface defects. On the contrary, a small shoulder around 540 nm appears to be slightly redshifted after In–S shell coating. Although the local maxima of the absorption spectra of AIS QDs are not obvious compared to CdSe and InP QDs, this change seems to reflect the extension of the exciton wavefunction due to the presence of the shell. The PL spectra showed a new PL component at 593 nm after In–S shell coating, probably due to band-edge PL. However, a significant amount of defective PL remained, consistent with the previous research that In–S coating does not completely remove defects.[52]

In addition, the position of band-edge PL was approximately 10 nm longer than that of AIS/Ga–S core/shell QDs (ranging between 575–585 nm). This is due to an insufficient core/shell band offset, with such a redshift being characteristic of core/shell QDs possessing a small band offset.[98] Concurrently, the PL QY value was only 1% for the band-edge PL and 23% over the entire emission spectrum, which is a significant decrease from 76% before the In–S shell coating. This drastic QY decrease is attributed to the strong tendency of the In–S surface oxidation to increase the nonradiative transition rate.[99]

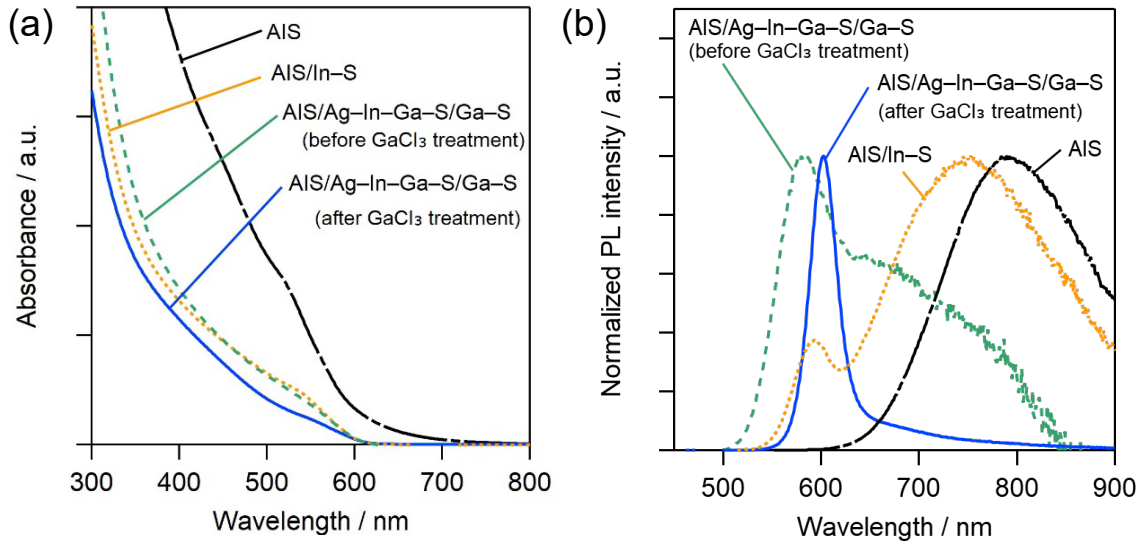

Figure 2-3. (a) Absorption and (b) PL spectra of AIS core, AIS/In–S core/shell, and AIS/Ag–In–Ga–S/Ga–S core/graded shell QDs before and after $GaCl_3$ treatment.

Figure 2-4 presents the PL decay profiles of the AIS core (the black curve) and AIS/In–S core/shell QDs (the yellow curve). These curves were fitted with a two or three exponential equation given by equation 2-1:

$$I(\mathrm{t}) = A_1\exp(-\frac{t}{\tau_1}) + A_2\exp(-\frac{t}{\tau_2}) + A_3\exp(-\frac{t}{\tau_3}) \quad (2\text{-}1)$$

where I(t) denotes the PL intensity at time t, A_1, A_2, and A_3 are the amplitudes, and τ_1, τ_2, and τ_3 are the corresponding lifetimes. When fitting the data, I used the minimum number of exponents necessary to achieve a satisfactory fit. The quality of fit was assessed using the χ^2

value, a measure of error calculated as the sum of the squared differences between the observed and the expected values, each divided by the corresponding expected value. A χ^2 value below 1.2 was considered acceptable. The fitting results are summarized in **Table 2-2**, which also provides the values of intensity average (τ_{avg}). As previously reported, the PL of AIS core (τ = 918 ns) can be attributed to the donor–acceptor pair recombination from defect states.[91, 100] On the other hand, the PL lifetime of the new peak appearing at 593 nm after In–S coating was significantly shorter than that of the core. This change suggests a transformation in the emission mechanism, possibly to the band-edge transition.[52]

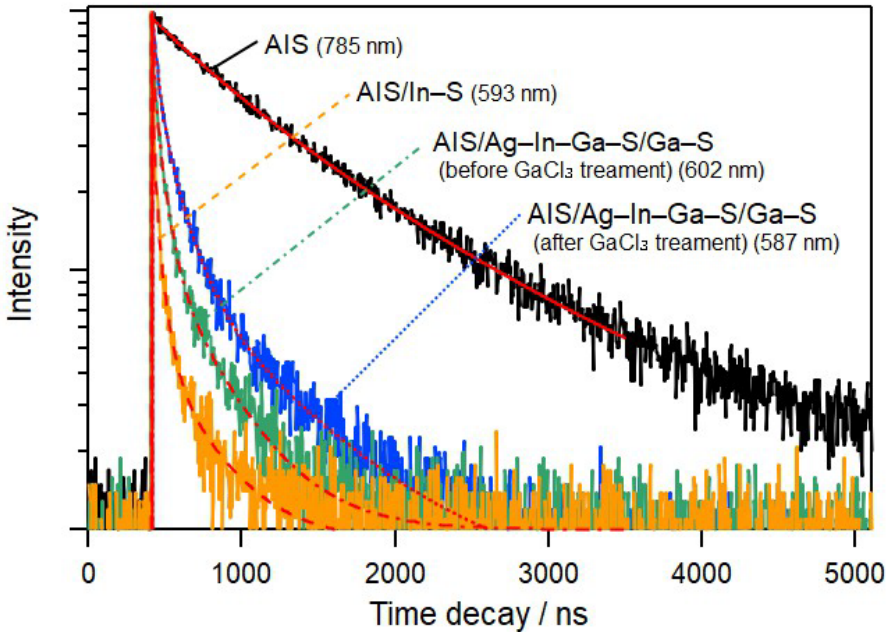

Figure 2-4. PL decay profiles of AIS core, AIS/In–S core/shell, and AIS/Ag–In–Ga–S/Ga–S core/graded shell QDs before and after $GaCl_3$ treatment.

Table 2-2. PL decay components of AIS core, AIS/In–S, and AIS/Ag–In–Ga–S/Ga–S core/graded shell QDs before and after $GaCl_3$ treatment.

Sample	τ_1/ns	A_1	τ_2/ns	A_2	τ_3/ns	A_3	χ^2	τ_{avg}[a]
AIS	918	1.00	–	–	–	–	1.16	918
AIS/In–S	3.67	0.703	26.6	0.255	182	0.042	1.19	92
AIS/Ag–In–Ga–S/Ga–S								
(Before $GaCl_3$ treatment)	11.7	0.526	63.2	0.380	337	0.094	1.07	198
(After $GaCl_3$ treatment)	33.5	0.503	140	0.406	684	0.092	1.05	377

[a] Intensity average calculated by $\sum_i A_i\tau_i^2 / \sum_i A_i\tau_i$

2.3.2 Overcoating with Ga–S outer shell

To further investigate into the effect of In–S shell, AIS/In–S core/shell QDs were subsequently coated with Ga–S outer shells. This additional layer is expected to passivate the In–S shell surface and reduce the nonradiative transition path, especially when such a transition is caused by surface oxidation. The process for applying the Ga–S coating was adapted from a recently developed method using $Ga(DDTC)_3$ as both the Ga and S sources.[75] After heating the AIS/In–S core/shell QDs alongside $Ga(DDTC)_3$, there was a notable increase in particle size from 5.3±0.7 nm to 7.0±1.0 nm (see **Fig. 2-1 (c)**). This change confirms the formation of the Ga–S outer shells. Whereas an increase in Ga content was observed, the In ratio within the $Ga(DDTC)_3$-treated QDs decreased and approached the values of before the In–S shell coating. This result, at first glance, suggests that the In–S shell is largely replaced by Ga–S, which is not surprising given the report that In_2S_3 can be the template for $AgInS_2$ and $ZnIn_2S_4$ owing to the presence of In vacancies.[101-102] The XRD patterns remained largely unchanged, indicating that the core QDs retained the tetragonal phase (**Fig. 2-2**, green curve). There was no shift in the absorption onset, whereas the band-edge PL was slightly blue-shifted to 587 nm and the ratio of defective PL was decreased compared to that before Ga–S coating (**Figs. 2-3 (a, b)**, green curves). Nevertheless, the

increase in PL QY for the band-edge moiety was marginal, moving from 1% to 3%. This trend was further supported by a slight extension of the PL decay profile (see **Fig. 2-4**, green curve).

Previously, the research group I am affiliated with experienced the lack of PL QY improvement of the band-edge emission after Ga–S shell formation (reaction with $Ga(DDTC)_3$). This phenomenon has been attributed to the insufficient decomposition of $Ga(DDTC)_3$, leading to a high organic residue after heating at 280 °C in OLA.[75] Currently, the most effective method to obtain pure inorganic Ga–S shells is to heat the core/shell QDs with $GaCl_3$. This process not only facilitates the conversion of $Ga(DDTC)_3$ to Ga–S but also eliminates trap states in the Ga–S shell through atomic rearrangement. After the $GaCl_3$ treatment, there was a slight particle growth, possibly due to the formation of a more rigid shell (**Fig. 2-1 (d)**). However, the resulting composition and structure differed from my initial expectations. Specifically, compositional analysis showed a further decrease in the In ratio after the treatment, whereas apparent In/Ga ratio rather increased owing to the decrease in Ga.

In XRD pattern (**Fig. 2-2**, the blue curve), a partial splitting of the highest peak (~27°) was observed. As mentioned, nanoparticles of AIS can exist in two distinct crystal phases, tetragonal chalcopyrite and orthorhombic.[51] In bulk systems, the orthorhombic phase is known as the high temperature phase because of its high tolerance for cation disordering, especially the exchange of Ag and In. However, in the nanocrystalline system, the orthorhombic phase can exist at room temperature when synthesized under certain conditions.[94] The three characteristic peaks around 27° are specific to the orthorhombic phase, and it is likely that, during the $GaCl_3$ treatment, a partial phase transition from tetragonal to orthorhombic took place. Since this transformation has not been observed in AIS/Ga–S core/shell QDs under the same $GaCl_3$ treatment, the presence of the In–S inner shell might be linked to this occurrence. In addition, the peaks appeared at higher angles relative to the

orthorhombic $AgInS_2$ reference (ICDD 075-6150). This result suggested the occurrence of partial In/Ga substitution, which caused an atomic rearrangement within particle. Such alterations in material properties lead to a noticeable shift in the emission spectrum as shown by the blue curve in **Figs. 2-3 (a, b)**. A distinct band-edge PL appeared at 602 nm, with its defect PL significantly reduced compared to the untreated states. PL decay analysis revealed an increase in lifetimes, consistent with the earlier observations that the gallium chloride treatment reduces the nonradiative transitions (**Table 2-2**). Yet, these recorded lifetimes were longer than the previously documented values for AIS[51-52] and Ag–In–Ga–S[75, 92-93] core/shell QDs that exhibited similar or superior PL QY values. This suggests that the sample after $GaCl_3$ treatment has a distinct electronic state that is different from the previous AIS or Ag–In–Ga–S core/shell QDs synthesized without an In–S interlayer.

2.3.3 Effect of reaction temperature for In–S shell coating

In order to more clearly discern the effect of In–S interlayer, the reaction temperature for the In–S coating was incrementally raised from 180 °C to 200 °C and 220 °C, with the aim of producing thicker shells. **Figures 2-5 (a, b)** displayed the TEM images of AIS/In–S core/shell QDs prepared with the growth temperature of 200 °C and 220 °C. These QDs had average diameters of 6.2±1.3 nm and 7.7±1.7 nm when In–S shells were coated at 200 °C and 220 °C, respectively. Compositional examinations highlighted an increased In ratio (**Table 2-3**), which varied from In/Ag = 1.66 (180 °C) to In/Ag = 1.72 (200 °C) and further to 1.76 (220 °C). However, these values were below the values expected from the volumetric changes of the particles due to the shell formation, which was $V_{core/shell}/V_{core}$ = 200% for 180 °C, 221% for 200 °C, and 394% for 220 °C. This discrepancy became more pronounced at elevated reaction temperatures. Given the increased polydispersity of the latter two QDs, the observed increase in particle size can be ascribed not only to In–S shell expansion, but also to Ostwald ripening, which is likely to be more pronounced at higher temperatures. In

terms of crystal structure, the shift toward the orthorhombic phase became pronounced as the reaction temperature increased (see **Fig. 2-6 (a)**). Such trends starkly contrast with the Ga–S shell formation process where the tetragonal phase remains after the reaction at 280 °C, thereby highlighting the distinctive nature of the In–S shell.

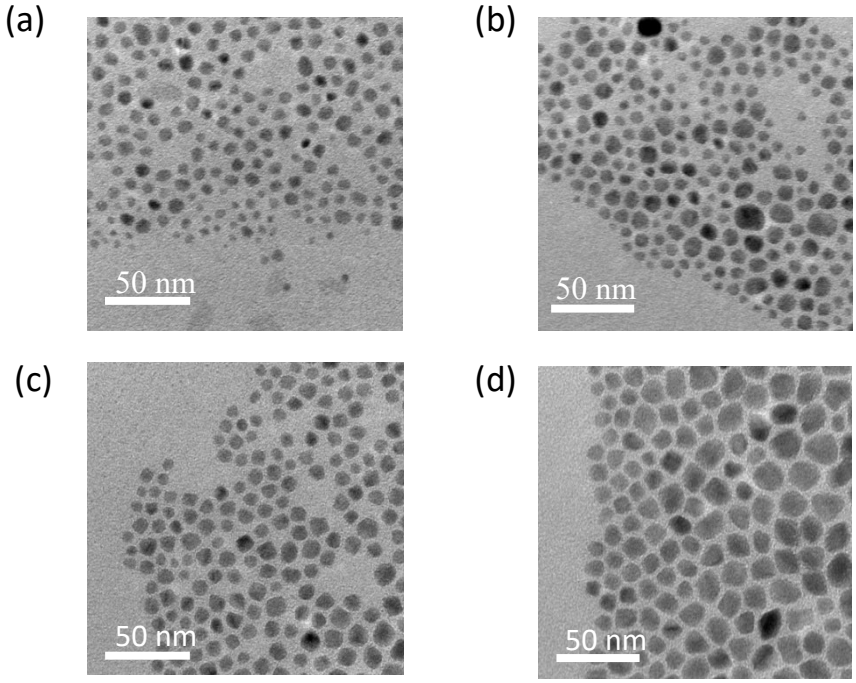

Figure 2-5. TEM images of (a, b) AIS/In–S core/shell QDs and (c, d) AIS/Ag–In–Ga–S/Ga–S core/graded shell QDs. The In–S growth temperatures are (a, c) 200 °C and (b, d) 220 °C.

Table 2-3. Elemental composition of AIS/In–S core and AIS/Ag–In–Ga–S/Ga–S core/graded shell QDs synthesized with different In–S growth temperatures.

Sample	In–S growth temperature	Composition ratios (Ag = 1.00)			
		Ag	In	S	Ga
AIS/In–S	200 °C	1.00	1.72	3.20	–
AIS/Ag–In–Ga–S/Ga–S[a]		1.00	0.71	2.45	0.70
AIS/In–S	220 °C	1.00	1.76	3.30	–
AIS/Ag–In–Ga–S/Ga–S[a]		1.00	0.61	2.69	0.95

[a] After $GaCl_3$ treatment

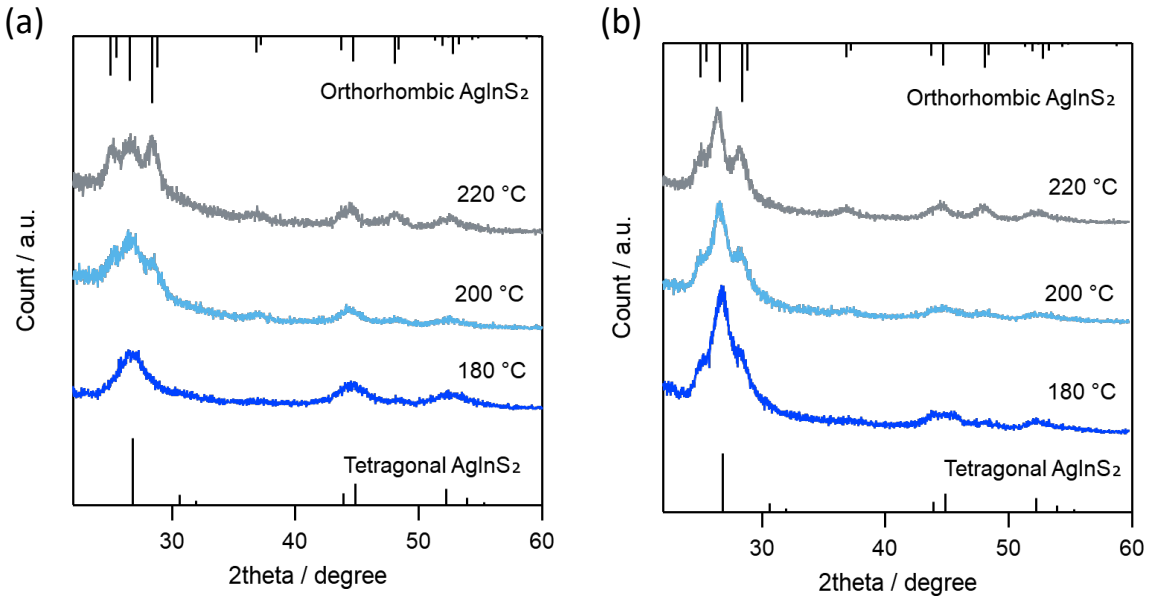

Figure 2-6. XRD patterns for (a) AIS/In–S core/shell and (b) AIS/Ag–In–Ga–S/Ga–S core/graded shell QDs. The growth temperatures for the In–S shell in each figure are 180 °C, 200 °C, and 220 °C. Reference bars at the top and bottom of the graph correspond to orthorhombic (ICDD 075-6150) and tetragonal $AgInS_2$ (ICDD 077-6632) phases, respectively.

Figures 2-7 (a, b) and 2-8 (a) show the absorption spectra, PL spectra, and decay curves of AIS/In–S core/shell QDs, respectively, recorded at their respective band-edge PL peaks. The presence of band-edge PL indicates that the type-I core/shell structure remains intact as the In–S shell thickens. However, there was a notable redshift with increasing temperature for the In–S shell coating, which is due to the broadening of the wavefunction. Meanwhile, the QY values consistently decreased, indicating the increase of nonradiative recombination due to the defective nature of the In–S shells. The two contradictory effects might contribute to the irregular variation of the PL lifetimes, which was 92 ns (180 °C), 91 ns (200 °C), 109 ns (220 °C). When these samples were reacted with $Ga(DDTC)_3$ and subsequently treated with $GaCl_3$ to complete the Ga–S shell, the band-edge PL became even more pronounced. **Figures 2-7 (c, d) and 2-8 (b)** show the absorption spectra, PL spectra, and decay curves, respectively. The PL peak wavelength was shifted to 612 nm (for 200 °C)

and 622 nm (for 220 °C), showing a redshift of approximately 40 nm from the standard AIS/Ga–S core/shell QDs (575–585 nm). Also, the absorption onset redshifted with an increase in the growth temperature. Much like the samples coated with In–S shell at 180 °C, there was an observable increase in particle size and decrease in the In ratio (see in **Figs. 2-5 (c, d)** and listed in **Table 2-3**), accompanied by a subtle transition to the orthorhombic phase (see in **Fig. 2-6 (b)**). An extended PL decay time further suggests a reduction in nonradiative transitions.

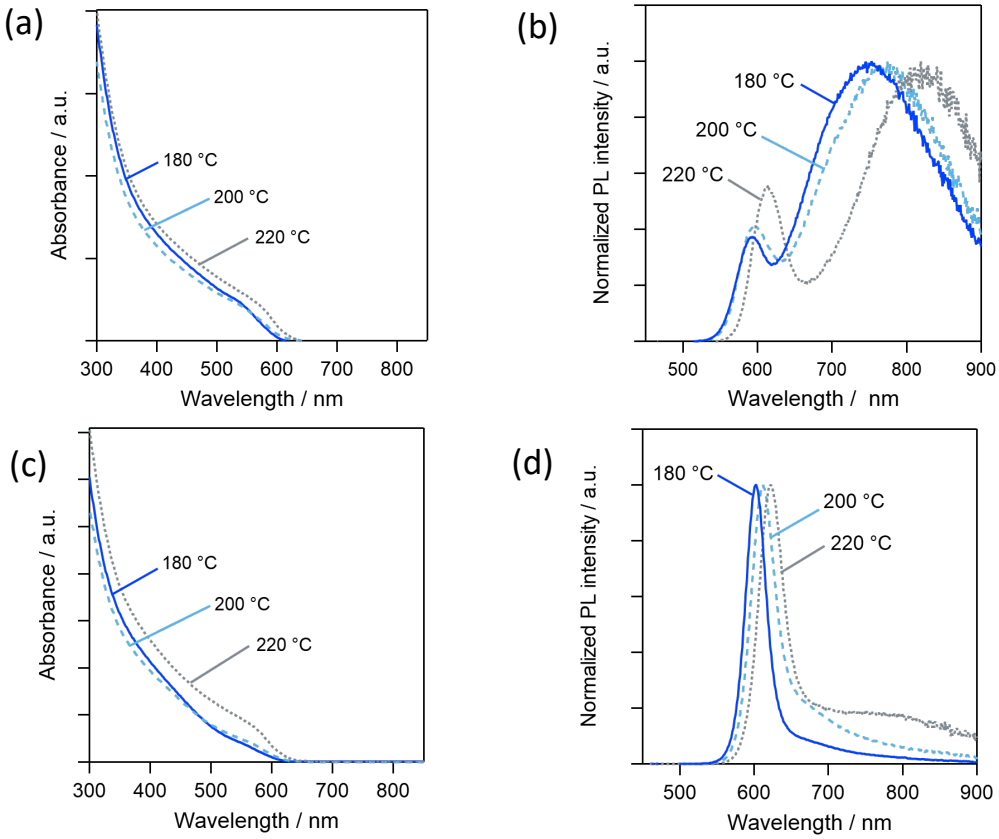

Figure 2-7. Absorption and PL spectra of (a, b) AIS/In–S core/shell and (c, d) AIS/Ag–In–Ga–S/Ga–S core/graded shell QDs, synthesized at In–S shell growth temperatures of (blue) 180 °C , (sky blue) 200 °C, and (grey) 220 °C.

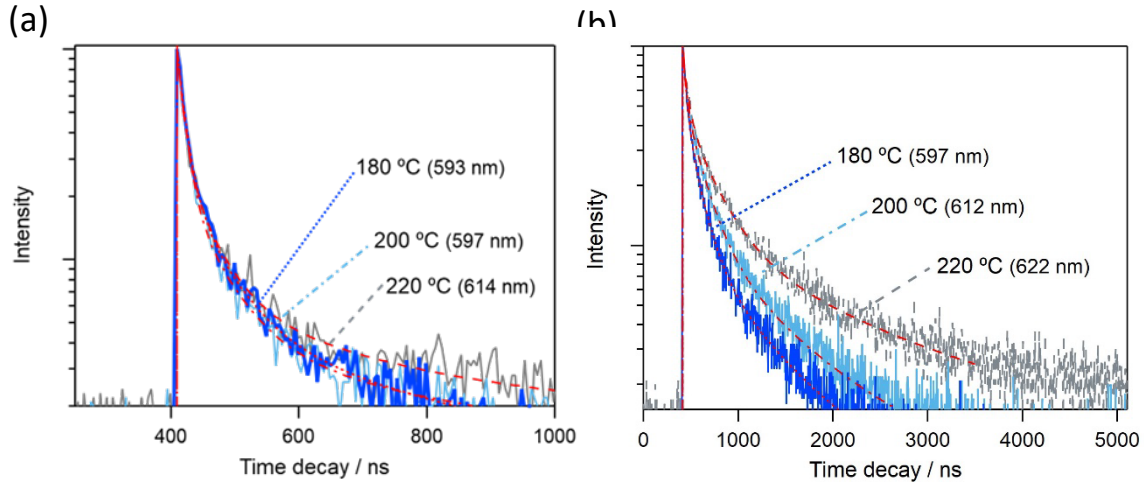

Figure 2-8. PL lifetimes for (a) AIS/In–S core/shell and (b) AIS/Ag–In–Ga–S/Ga–S core/graded shell at In–S growth temperatures of In–S; 180, 200, and 220 °C.

Table 2-4. PL decay components of AIS/In–S core/shell, and AIS/Ag–In–Ga–S/Ga–S core/graded shell QDs synthesized with different In–S growth temperatures.

Sample	In–S growth temp.	τ_1/ns	A_1	τ_2/ns	A_2	τ_3/ns	A_3	χ^2	τ_{avg}[b]
AIS/In–S		3.11	0.703	25.4	0.266	196	0.031	1.02	91
AIS/Ag–In–Ga–S/Ga–S[a]	200 °C	31.6	0.474	187	0.425	872	0.101	1.07	504
AIS/In–S		3.66	0.755	32.4	0.215	234	0.029	1.17	109
AIS/Ag–In–Ga–S/Ga–S[a]	220 °C	50.7	0.507	287	0.390	1530	0.103	0.92	932

[a] After $GaCl_3$ treatment, [b] Intensity average calculated by $\sum_i A_i\tau_i^2 / \sum_i A_i\tau_i$

2.3.4 Discussion

Collectively, the data obtained suggest that the application of the In–S shell coating prior to Ga–S redshifts the band-edge PL wavelength by up to 40 nm. A notable structural variation associated with this wavelength change is the phase shift of the core from tetragonal

to orthorhombic. However, based on previous publication[51], the shape and position of the band-edge PL was irrelevant to the crystalline phases. When the PL of QDs redshifted more than expected from their composition, it is often attributed to carrier delocalization that appears when there is minimal potential offset between the core and shell: quasi-type II band alignment.[103] However, a straightforward explanation involving an In–S/Ga–S multishell structure, where the In–S inner shell borders between type I and II relative to the AIS core, was inconsistent with the results of the compositional analyses. Boldt *et al.* observed a redshift during heating CdSe/CdS/ZnS core/multishell QDs at 310 °C, and attributed it to the formation of CdSe/$Cd_xZn_{1-x}S$ core/graded shell structure due to interfacial alloying.[104-105] While alloying at the type I core/shell interface typically results in an increased bandgap for the core, the graded composition creates a stepless band-edge potential curve, which broadens the electron wavefunction. If this broadening effect is more pronounced than the increase in the core's bandgap, a redshift would occur. Accompanying this shift, they also reported a 2.0-fold elongation of PL decay lifetimes and a rise in PL QY. These findings resonate well with the optical variations observed for AIS/In–Ga–S/Ga–S core/multishell QDs during the $GaCl_3$ treatment.

Figure 2-9 (a) summarizes the structural changes during the shell formation and the subsequent $GaCl_3$ treatment. The In–S shell, by itself, contributed to the band-edge PL, although its intensity was weak due to the limited band offset at the core/shell interface. The subsequent Ga–S shell coating improved the band-edge PL ratio, which is consistent with the AIS/Ga–S core/shell QDs without an In–S interlayer. After the $GaCl_3$ treatment performed at 280 °C, the band-edge PL intensified and redshifted even though the In content decreased to below the level of Ag. If I follow the previous idea that $GaCl_3$ treatment promotes atomic rearrangement, these contradictory observations suggest the formation of a graded shell. Considering the significant decrease in In content, the structure of the QDs after $GaCl_3$

treatment is closer to AIS/Ag–In–Ga–S/Ga–S rather than AIS/In–Ga–S/Ga–S. While this structure causes an increase in core's bandgap, the compositional gradient in the shell region stretched the carrier wavefunction to induce the redshift. It is likely that the stretching of the carrier wavefunction exceeded the effect of Ga substitution in the core.

Figure 2-9 (b) shows the calculation of the quantum size effect for AIS QDs based on the finite-depth effective mass approximation; details are provided in the General Introduction.[38-40, 106-107] In this study, relative permittivity (ϵ) 6.7[108] and the electron mass (m_e) and hole mass (m_h) are 0.12 and 0.21, respectively[107]. Because I do not get the rigorous structure of the graded shell, a model assuming a uniform core ($E_{g,\ bulk}$ = 1.87 eV) and a surrounding matrix (E_g = 5.00 eV) was adopted.[41] The bandgap value of 4.2-nm AIS core QDs is expected to be 2.15 eV (576 nm) and is similar to the reported PL peak wavelength for AIS/Ga–S core/shell QDs (582 nm)[51], validating this calculation. When the PL wavelengths of the AIS/Ag–In–Ga–S/Ga–S core/graded shell QDs were plotted as a function of the apparent diameter, the three plots were at ca. 70 meV above the expected bandgap. This difference may be due to the presence of the Ga–S outer shell, meaning that the actual wavefunction distribution is smaller than the apparent size. Because the variation of the bandgap energy is almost parallel to that by the size effect, the redshift in PL is thought to result primarily from the extension of the excited carrier wavefunction within the graded composition particle.

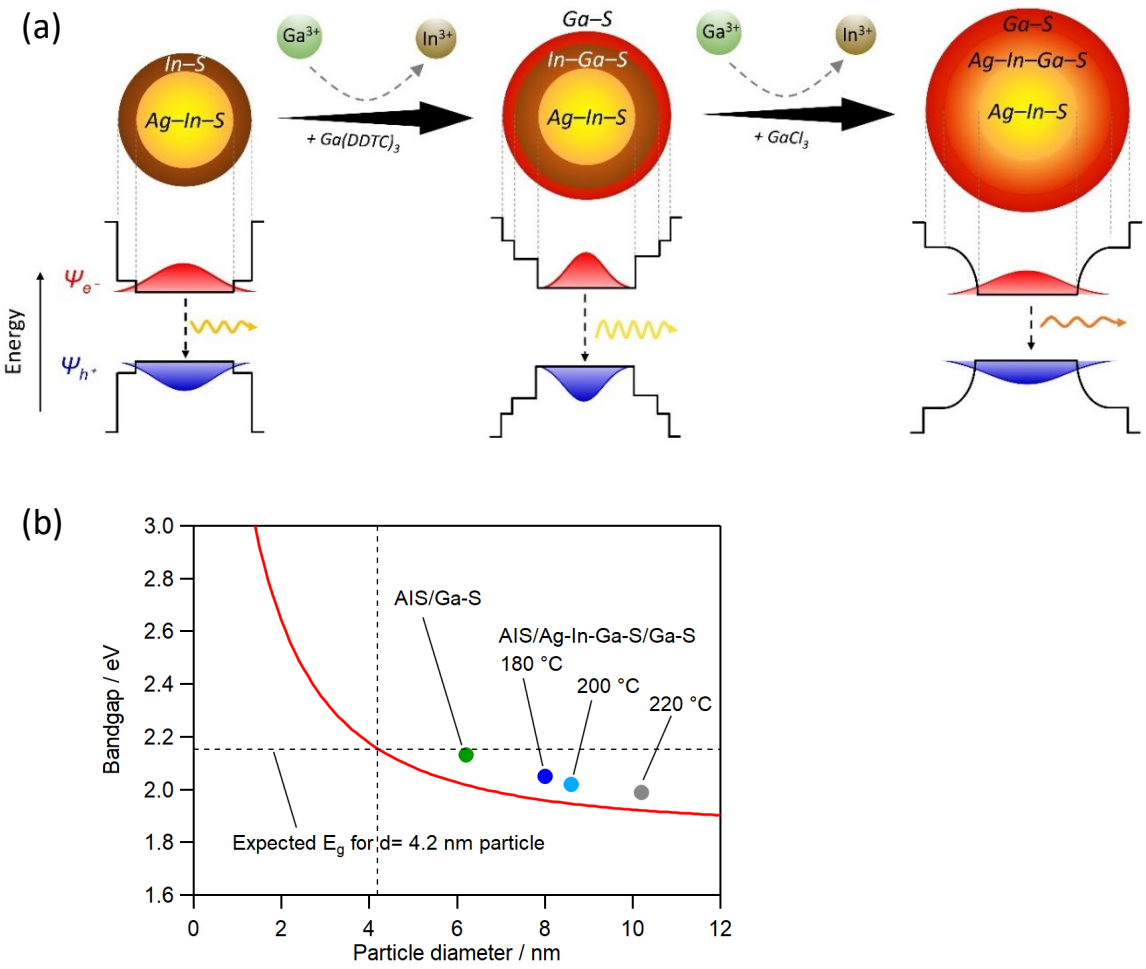

Figure 2-9. (a) Structural illustrations and corresponding electronic diagrams of AIS/In–S core/shell QDs during the formation Ga–S shells and their treatment with $GaCl_3$. (b) (red line) Calculated bandgap variation of $AgInS_2$ QDs by quantum size effect and (circles) plots of PL peak energies for AIS/Ga–S core/shell and AIS/Ag–In–Ga–S/Ga–S core/graded shell QDs with In–S shell growth temperatures of 180, 200, and 220 °C.

2.4 Summary

In summary, I demonstrate a PL redshift of the AIS QDs by coating In–S prior to Ga–S shells. As previously reported, the In–S shell by itself exhibited only a weak band-edge PL. However, the presence of the In–S as an inner shell altered the PL characteristics after coating the Ga–S shells. This redshift could be attributed to the inner shell, which has a smaller bandgap than Ga–S, broadening the distribution of the

wavefunction and reducing the quantum size effect. However, the elemental composition showed a decrease in In content after the heat treatment with $GaCl_3$, which is essential to complete the Ga–S shell. This indicated the replacement of In in the core with Ga, theoretically increasing the bandgap. These inconsistent results were discussed in relation to the formation of the shells with graded compositions, which was reported to redshift the PL. Also, the increase in PL lifetimes, indicating the decrased overlap of electron and hole wavefunctions, supported these considerations. By raising the reaction temperature during In–S coating, thicker In–S layers were formed. These nanoparticles also experienced a decrease in In content after Ga–S shell coating. However, the redshift in the band-edge emission was significant, shifting 40 nm compared to standard AIS/Ga–S core/shell QDs, and achieving a red emission with a peak at 622 nm without the use of other elements.

Chapter 3

Bright Red Luminescence from Ag−In−Ga−S-based Quantum Dots by Introducing Copper

3.1 Introduction

As the commercial use of QDs expands, there is an increasing demand for Cd-free QDs.[94, 109-114] The research group I am affiliated with has achieved PL from AIS QDs, an alternative to cadmium chalcogenide QDs, utilizing groups 11 and 13 metals instead of group 12 metals.[44, 115-116] Unfortunately, at that time, group 11–13–16 QDs only displayed broadband emission due to defect levels in the bandgap, significantly diminishing their value as fluorophores. Narrow band-edge PL in the yellow region (580–590 nm) was achieved by coating the surface of AIS QDs with Ga–S shells.[51-52] The Ga–S shell, a group 13–16 semiconductor, was effective in eliminating trap states on the $AgInS_2$ QDs' surface. The band-edge emission was then blue-shifted to green by either alloying $AgInS_2$ ($E_{g,\ bulk}$ = 1.8 eV) with $AgGaS_2$ ($E_{g,\ bulk}$ = 2.6 eV) to increase the bandgap of the cores,[74, 92-93] or by reducing the size of the $AgInS_2$ cores to less than 4 nm.[117]

The selective synthesis of multinary nanomaterials is challenging, and controlling their composition and size is difficult owing to the reactivity gap between metals. For instance, the synthesis of quaternary silver indium gallium sulfide ($AgIn_xGa_{1-x}S_2$, Ag–In–Ga–S) QDs often results in Ag_2S particles because of the high reactivity of Ag with S, which reduced the product yield of the target QDs (<15%). This issue was recently overcome by injecting an Ag source into a solution containing activated In, Ga, and S sources, producing 4-nm Ag–In–Ga–S QDs with a product yield of above 60%.[75] Furthermore, the uniform composition in a QD ensemble facilitated the monochromaticity in PL after coating with Ga–S shells. Because the bandgap of the Ag–In–Ga–S quaternary system strongly depends on the In/Ga ratio,

inhomogeneity in composition as well as size can be an origin of spectral broadening. Therefore, the achievement of a record-narrow PL FWHM (31 nm) indicates that the method based on Ag source injection provides accurate composition control. This was a record narrow value as the Cd-free QD ensemble.

In this study, red luminescence was generated from AIS/Ga–S-based core/shell QDs by incorporating Cu. As $CuInS_2$ in bulk possesses a narrower bandgap (1.5 eV) compared to that of AIS (1.8 eV), I anticipate that a reduction in the bandgap could change the color from yellow to red.[118] Hughes et al. recently studied Cu doping in AIS QDs that exhibit a defective PL at 720 nm. They identified a nonlinear relationship between the defective PL wavelength and an increasing Cu ratio, and the PL was observed to shift to 800 nm (comparable to that of pure $CuInS_2$) even at Cu ratios as low as 0.2.[119] They stated that Cu doping generates acceptor levels derived from the Cu3d orbital, which promptly induces a PL redshift. It will be interesting to observe changes in the spectra of the band-edge emitting AIS/Ga–S core/shell QDs upon doping with Cu.

3.2 Experimental section

3.2.1 Materials

Silver(I) *N,N'*-diethyldithiocarbamate (Ag(DDTC), >98.0%), sodium *N,N'*-diethyldithiocarbamate trihydrate ($NaDDTC \cdot 3H_2O$, 92.0%), Copper(II) sulfate pentahydrate ($CuSO_4 \cdot 5H_2O$, 99.5%), and 1-octadecene (>90.0%) were purchased from FUJIFILM Wako Pure Chemical Industries Ltd. Hydroxyl amine hydrochloride ($NH_2OH \cdot HCl$, >97.0%) was purchased from TCI (Tokyo Chemical Industry Co., Ltd.). Tris(4-carbazoyl-9-ylphenyl)amine (TCTA, 97%) was purchased from Luminescence Technology. Al (99.9%) and molybdenum(VI) oxide (MoO_3, 99.9999%) were purchased from the Kojundo Chemical Laboratory. $Zn_xMg_{1-x}O$ (x = 0.05) nanoparticles were prepared based on the procedures

described in literature.[120-121] Water used in this study was purified by Milli-Q Integral-3 (Merck, 18.2 MΩ cm).

Silver(I) acetate (Ag(OAc)) was purchased from the same supplier mentioned in Chapter 1 (1.2.1). Indium(III) chloride ($InCl_3$), Gallium(III) chloride ($GaCl_3$), and diethylammonium *N,N'*-diethyldithiocarbamate (DEA–DDTC) were purchased from the same suppliers mentioned in Chapter 2 (2.2.1). Besides, oleylamine (OLA, FUJIFILM Wako Pure Chemical Industries Ltd.) was purified in the same manner as described in Chapter 1 (1.2.1).

3.2.2 Synthesis of Indium(III) *N,N'*-diethyldithiocarbamate

Indium(III) *N,N'*-diethyldithiocarbamate ($In(DDTC)_3$) were prepared by a similar method of $GaCl_3$ (5.6 mmol, 1 g), DEA–DDTC (17.1 mmol, 3.7 g), and dehydrated toluene (75 mL) were added in a 200-mL erlenmeyer flask under glove box and then vigorously stirred for 1 hour. After the reaction was completed, the product was collected by a rotary evaporator and was dried under vacuum for 1 hour to eliminate any unreacted precursor and solvent. The $Ga(DDTC)_3$ was further purified by re-crystallization in chloroform for 12 hours. The purified $Ga(DDTC)_3$ was recovered by filtration and vacuum-dried at 60 °C for 3 hours with a yield of 82%. Finally, $Ga(DDTC)_3$ was stored in a desiccator cabinet filled with N_2 before use. The composition of the product was confirmed by an ICP–AES to be In:S = 1:6.3.

3.2.3 Synthesis of copper *N,N'*-diethyldithiocarbamate

Copper *N,N'*-diethyldithiocarbamate (CuDDTC) was synthesized following the report by Nguyen et al.[122] $CuSO_4 \cdot 5H_2O$ (12.8 mmol, 3.2 g) was added to a 300 mL ice-cooled three-neck flask and dissolved in ultrapure water (100 mL). After introducing argon, ammonia (25 mL) was added to this aqueous solution, and the solution color was changed to deep blue. Hydroxylamine hydrochloride (50.4 mmol, 3.5 g) was then added over a period of 45 minutes, after which the deep blue solution gradually changed to colorless. After stirring overnight,

sodium diethyldithiocarbamate trihydrate (15.6 mmol, 3.51 g) dissolved in ultra-pure water (40 mL) was added to this solution, and the resulting yellow crystals were separated by vacuum filtration. The crystals were washed in sequence with water, ethanol, and diethyl ether, then vacuum-dried at 50 Pa and 50 °C. The dried crystals were dissolved in as little chloroform as possible, then recrystallized using diethyl ether. The obtained yellow crystals were separated by vacuum filtration and vacuum-dried at 50 Pa. The composition of the product was confirmed by an energy dispersive X-ray spectrometer (EDS) to be Cu:S = 1:2.

3.2.4 Synthesis of gallium(III) *N,N'*-diethyldithiocarbamate

Gallium(III) *N,N'*-diethyldithiocarbamate ($Ga(DDTC)_3$) was prepared in a similar manner as described in Chapter 2 (2.2.2).

3.2.5 Synthesis of Ag–In–Ga–S core QDs

$In(DDTC)_3$ (0.3 mmol, 167.9 mg), $InCl_3$ (0.2 mmol, 44.2 mg), $Ga(DDTC)_3$ (0.1 mmol, 51.45 mg), and OLA (10 mL) were added to a 50-mL two-neck flask. The mixture was evacuated and heated to 100 °C, and the temperature was maintained for 10 min before argon was introduced. The temperature controller was set to 200 °C, and when the temperature reached 130 °C, an OLA solution (1 mL) containing Ag(OAc) (0.25 mmol, 41.7 mg) was immediately injected into the reaction solution. The temperature was increased to 200 °C and maintained for 20 min, after which the heating mantle was removed, and the solution was allowed to cool. The nanoparticle component was precipitated using acetone and methanol, which was then separated through centrifugation. Purification was performed twice through dissolution/re-precipitation by using chloroform and methanol, and the product was then dispersed in hexane.

3.2.6 Synthesis of Ag–Cu–In–Ga–S core QDs

In a 50 mL two-neck flask, $In(DDTC)_3$ (0.2 mmol, 111.9 mg), $InCl_3$ (0.2 mmol, 44.2 mg), $Ga(DDTC)_3$ (0.1 mmol, 51.45 mg), and OLA (10 mL) were added, and the solution was evacuated and heated to 100 °C. After introducing argon, the temperature controller was set to 200 °C. When the actual temperature reached 150 °C, a mixture of AgDDTC (0.225 mmol, 57.63 mg) and CuDDTC (0.025 mmol, 5.30 mg) dispersed in octadecene was injected into the reaction solution. The reaction was continued and the product was purified similarly to the case of Ag–In–Ga–S QDs synthesis. In addition to this experiment, the molar ratio of raw materials was varied as listed in **Table 3-1**.

Table 3-1. List of materials and synthesis conditions.

No.	Group 11 elements	Group 13 elements	Injection temperature	Heating temp/ time	Data
1	Ag(OAc) 0.075 mmol	$In(DDTC)_3$ 0.10 mmol $InCl_3$ 0.05 mmol	120 °C	200 °C 20 min	Fig. 3-1
2	Ag(OAc) 0.25 mmol	$In(DDTC)_3$ 0.30 mmol $Ga(DDTC)_3$ 0.10 mmol $InCl_3$ 0.20 mmol	130 °C	200 °C 20 min	Fig. 3-2
3	Ag(DDTC) 0.225 mmol Cu(DDTC) 0.025 mmol	$In(DDTC)_3$ 0.10 mmol $Ga(DDTC)_3$ 0.10 mmol $InCl_3$ 0.20 mmol	150 °C	200 °C 20 min	Fig. 3-3 (a-d) (blue)
4	Ag(DDTC) 0.225 mmol Cu(DDTC) 0.025 mmol	$In(DDTC)_3$ 0.30 mmol $Ga(DDTC)_3$ 0.10 mmol $InCl_3$ 0.20 mmol	150 °C	200 °C 20 min	Fig. 3-3 (c) (purple)

Table 3-1. List of materials and synthesis conditions (continued).

No.	Group 11 elements	Group 13 elements	Injection temperature	Heating temp/ time	Data
5	Ag(DDTC) 0.225 mmol Cu(DDTC) 0.025 mmol	$Ga(DDTC)_3$ 0.20 mmol $InCl_3$ 0.20 mmol	150 °C	200 °C 20 min	Fig. 3-3 (c) (green)
6	Ag(DDTC) 0.175 mmol Cu(DDTC) 0.075 mmol	$In(DDTC)_3$ 0.10 mmol $Ga(DDTC)_3$ 0.10 mmol $InCl_3$ 0.20 mmol	160 °C	200 °C 20 min	Fig. 3-3 (d) (light green)
7	Ag(DDTC) 0.125 mmol Cu(DDTC) 0.125 mmol	$In(DDTC)_3$ 0.10 mmol $Ga(DDTC)_3$ 0.10 mmol $InCl_3$ 0.20 mmol	160 °C	200 °C 20 min	Fig. 3-3 (d) (orange)

3.2.7 Ga–S shell formation

Sulfur (0.1 mmol, 3.21 mg), $Ga(DDTC)_3$ (0.1 mmol, 51.45 mg), and OLA (10 mL) were added to a 50 mL two-neck flask. The solution was heated while being evacuated until it reached 100 °C. After maintaining this temperature for 10 minutes, argon was introduced, and the temperature controller was set to 230 °C. When the solution temperature reached 160 °C, core QDs dispersed in hexane was injected and the temperature was raised to 230 °C. When the solution temperature reached 230 °C, a solution of $GaCl_3$ (0.1 mmol, 17.61 mg) dissolved in OLA (0.5 mL) was injected and the temperature was further raised to 280 °C at a rate of 2 °C/min. When the solution temperature reached 280 °C, a solution of $GaCl_3$ (0.5 mmol, 88.04 mg) dissolved in OLA (2.5 mL) was injected and the mixture was stirred for an additional 30 minutes at the same temperature. The mixture was allowed to cool down, and the precipitate of nanoparticles obtained by adding methanol, which was collected by centrifugation and dispersed in 1 mL of chloroform.

3.2.8 Instrumental

The Instruments for material characterization were carried out as described in chapter 1 (1.2.5). Additionally, The surface chemical electronic state and composition of the QDs were measured using an X-ray photoelectron spectrometer (XPS; ULVAC–PHI ESCA3057) equipped with an Al target.

3.2.9 Fabrication of quantum-dot light-emitting diodes (QD-LED) devicesQuantum-dot

light-emitting diodes (QD-LEDs) were fabricated on 100 nm-thick indium tin oxide-patterned glass substrates. The substrates were cleaned through sequential sonication in a detergent and ethanol, which was then treated in an ultraviolet-ozone cleaner. A 40-nm-thick electron injection layer (EIL) comprising $Zn_{0.95}Mg_{0.05}O$ nanoparticles was formed by spin-coating, and baked at 180 °C. The Ag–In–Ga–S QDs were adjusted to a concentration of 3.5 mg/mL in chloroform and were spin-coated onto the EIL and baked at 100 °C (emitting layer, EML). Subsequently, the substrate was introduced into a vacuum chamber, and a 55-nm-thick TCTA, 10-nm-thick MoO_3, an 100-nm-thick Al anode were deposited successively as a hole transport layer, hole injection layer, and an anode, respectively. The QD-LEDs were encapsulated with a glass cover under an N_2 atmosphere and submitted to performance tests.

3.2.10 Characterization of QD-LED devices

The luminance−current−voltage characteristics of the QD-LEDs were measured using a luminance meter (Konica Minolta, LS-110) and a source meter (Keithley, Model 2400), and their EL spectra were measured using a spectroradiometer (Konica Minolta, CS-2000A). The EQE was calculated under the assumption of Lambertian emission. Furthermore, the cross-sectional images of the QD-LEDs were observed using a scanning electron microscope (SEM; Hitachi High-Tech, S- 5500) after cross-sectional processing using a focused ion beam.

3.3 Results and discussion

3.3.1 Formation of Ag–In–Ga–S/Ga–S core/shell QDs with high In ratio

As mentioned in the introduction, an injection of $Ag(OAc)_3$ into a mixture of $Ga(DDTC)_3$ and $InCl_3$ produces Ag–In–Ga–S quaternary QDs very accurately and selectively. This process involves the formation of Ag_2S nanoparticle intermediates, which eventually transform into monodisperse Ag–In–Ga–S QDs. With this in mind, as a first experiment, I attempted to synthesize AIS QDs by substituting $Ga(DDTC)_3$ with $In(DDTC)_3$, the conditions of which are shown in **Table 3-1** (sample No. 1). However, the obtained QDs were polydisperse and larger (d = 7.0 ± 1.7 nm) than the recently prepared Ag–In–Ga–S QDs (3.9 ± 0.4 nm),[75] with a significant defect PL remaining even after Ga–S shell coating (**Fig. 3-1**). In the synthesis of Ag–In–Ga–S quantum dots, the mixture precursors acted as a dual-purpose agent, providing the materials and forming a protective shell around the Ag_2S seeds. Therefore, the insufficient size control could be due to the inability of the indium sulfide precursor to protect the Ag_2S seeds. This resulted in significant growth of Ag_2S, which in turn led to an increase in the particle size of the AIS QDs.

To address this issue, a small amount of $Ga(DDTC)_3$ was employed as a protectant for the Ag_2S seeds. **Figs. 3-2 (a, b)** shows the ultraviolet–visible (UV–vis) spectra of Ag–In–Ga–S core QDs before and after coating with Ga–S shells. Predominantly, the emission from the core QDs is composed of a broad component, attributable to defect transition. However, a discernable shoulder emerges on the short wavelength side (580 nm). As recently reported, this shoulder is identified as the band-edge PL and is peculiar to the QDs synthesized through Ag-source injection.[75] The synthesis process involves the formation of Ag_2S/In–Ga–S pseudo-core/shell structure, which subsequently transitions to Ag–In–Ga–S QDs, leaving an excess of In–Ga–S to form a thin passivation layer. After coating with Ga–S shells, a distinct band-edge PL was observed at 593 nm with a FWHM of 33 nm (120 meV). The redshift of

the peak is correlated with an increase in shell thickness, which leads to an extension of the electron/hole wavefunctions due to limited band offsets between the core and the shell. The defect PL moiety decreased more than that of the QDs synthesized using only In precursors. TEM image shows that the addition of a small amount of $Ga(DDTC)_3$ effectively prevents the excessive growth of the QDs (d = 5.5 ± 1.0 nm, **Figs. 3-2 (c, d)**), without causing a significant PL blueshift.

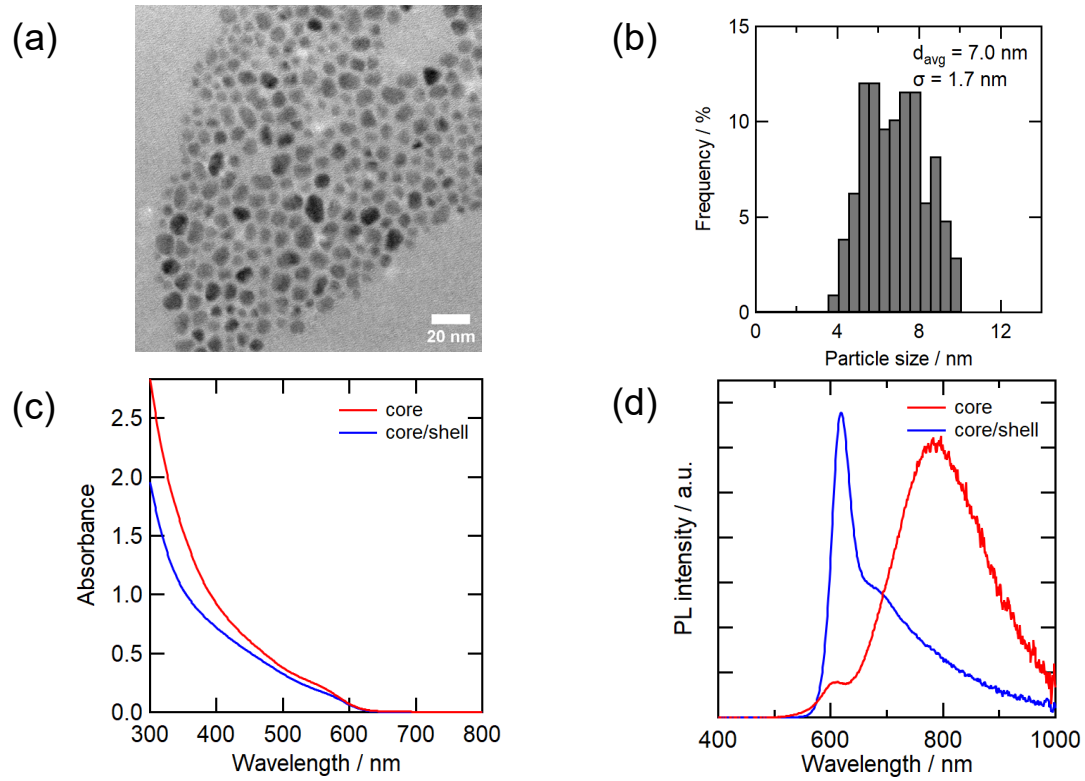

Figure 3-1. (a, b) TEM image of AIS core QDs, (c) UV–vis and (d) PL spectra of (red) AIS core and (blue) AIS/GaS_z core/shell QDs. The core QDs were prepared synthesized by injecting Ag(OAc) into an OLA solution containing $In(DDTC)_3$ and $InCl_3$ (refer to sample No. 1 in **Table 3-1**).

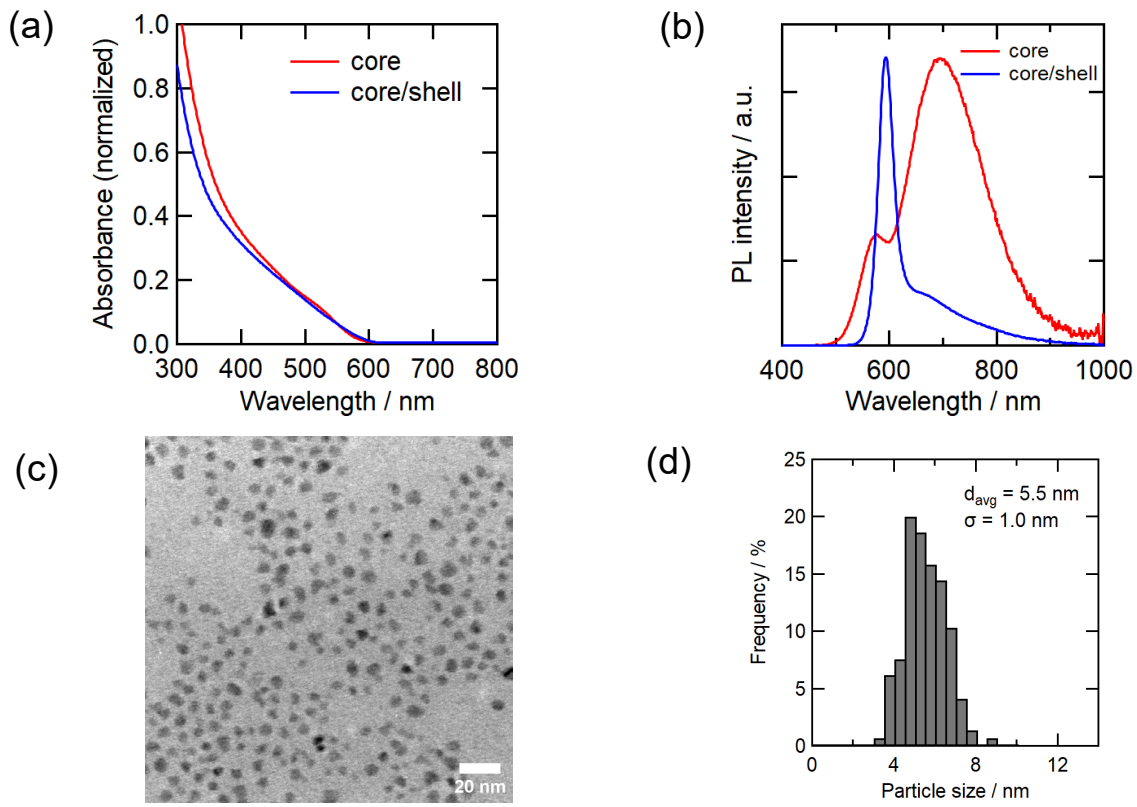

Figure 3-2. (a) UV–vis absorption and (b) PL spectra of Ag–In–Ga–S core (red) and Ag–In–Ga–S/Ga–S core/shell QDs (blue) (c, d) TEM image of Ag–In–Ga–S core QDs. The core QDs were prepared by Ag-source injection using specific precursor amounts (refer to sample No. 2 in **Table 3-1**).

3.3.2 Formation of Ag–Cu–In–Ga–S/Ga–S core/shell QDs

Based on the role of reagents mentioned in the previous section, I prepared Ag–Cu–In–Ga–S quinary QDs by replacing partly the Ag precursor with a Cu precursor. However, when Cu(OAc) was mixed with Ag(OAc) in OLA, the solution color changed to blue, indicating the formation of Cu(II) species. Considering the standard potentials versus standard hydrogen electrode, i.e., $E^{o}_{Cu^{2+/+}} = 0.153\ V$, $E^{o}_{Ag^{+/0}} = 0.7994\ V$, the color change can be attributed to the redox reaction between Cu(I) and Ag(I) acetates, generating Cu(II) acetate and Ag(0). To avoid the undesirable reaction between the raw materials, I examined group 11 precursors and selected a combination of Ag(DDTC) and Cu(DDTC), which appears to minimally

disrupt on the established reaction mechanism for the Ag–In–Ga–S quaternary system. I prepared the air-stable, pale-yellow Cu(DDTC) powder using a previously reported method, and confirmed a Cu:S ratio of 1:2 through energy dispersive X-ray analysis.[122] However, upon dissolving Cu(DDTC) in OLA, I observed a gradual color change from yellow to green, eventually resulting in a blue precipitate. Since Cu(DDTC) is easily oxidized by oxygen in certain solvents, such as acetonitrile, the color change suggests the formation of Cu(II) species. Consequently, I selected to introduce the Ag(DDTC) and Cu(DDTC) mixture as an octadecene (ODE) suspension.

Figure 3-3 (a, b) shows UV–vis and PL spectra of Ag–Cu–In–Ga–S core and core/shell QDs. Shell formation was conducted similarly to the case of the Ag–In–Ga–S QDs.[75] The introduction of Cu, constituting 10% of the total group 11 elements, redshifted the PL of the core/shell QDs from 593 nm to 651 nm (**Table 3-2)**. The FWHM of the PL spectra was 60 nm (183 meV), when Gaussian curve fitting was performed in the range where defect PL was not prominent. The PL QY was 65%, comparable to or even higher than the green-color PL of Ag–In–Ga–S core/shell QDs. Intriguingly, the PL peak positions were significantly influenced by In/Ga precursor ratios, but only weakly correlated with Cu/Ag ratios (**Figs. 3-3 (c, d)**). The narrowest PL FHWMin energy (55 nm, 152 meV) was recorded for the highest In sample (In/Ga = 0.50/0.10), but it was still broader than the yellow-color PL (peak = 592 nm) obtained without Cu precursor (FWHM = 33 nm, 120 meV, **Fig. 3-2**) and typical green-emission (peak = 524 nm) of Ag–In–Ga–S core/shell QDs (FWHM = 28 nm, 128 meV) (discussed later in text).

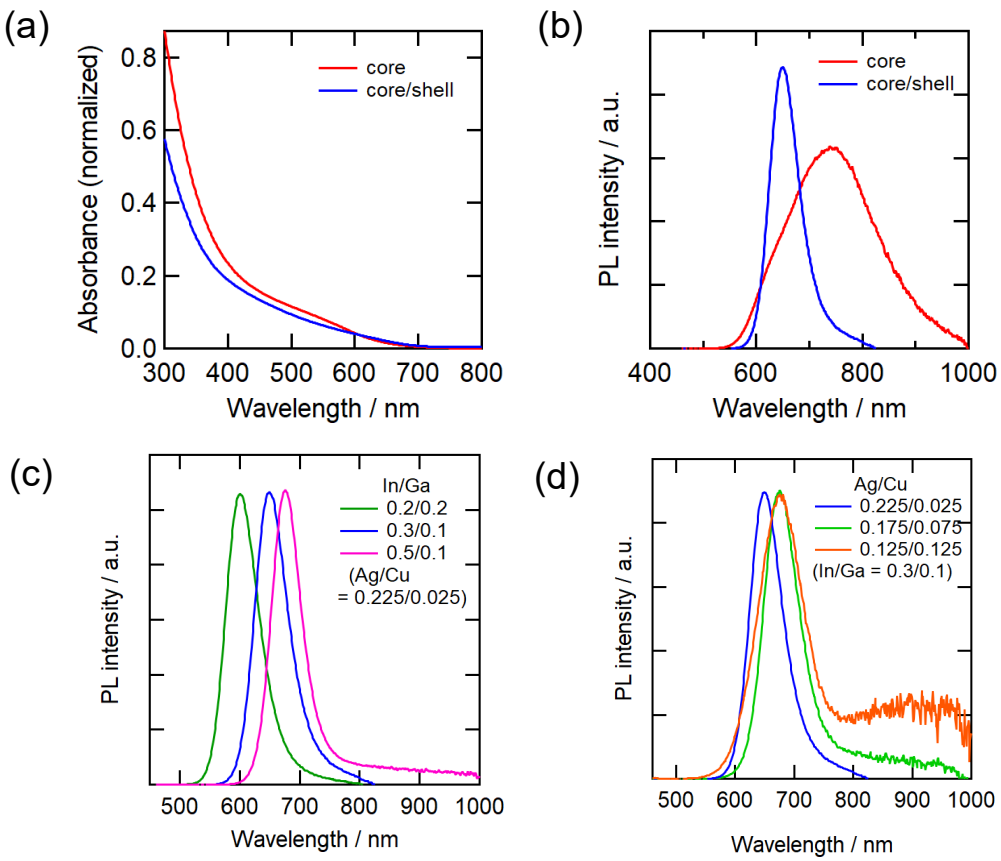

Figure 3-3. Comparative spectral analysis of Ag–Cu–In–Ga–S QDs. (a) UV–vis absorption spectra, and (b) PL spectra of the Ag–Cu–In–Ga–S core QDs (red), and the Ag–Cu–In–Ga–S/Ga–S core/shell QDs (blue). The cores were synthesized using specific precursor quantities (see sample No. 3 in **Table 3-1**). PL spectra demonstrating the impact of varying (c) In/Ga (sample No. 3, 4, and 5) and (d) Cu/Ag precursor ratios (sample No. 3, 6, and 7) on the luminescence properties of the core/shell QDs are also presented.

Table 3-2. List of optical properties of core/shell QDs.

No.	PL peak position (core/shell)	FWHM	PL QY	Data
1	618 nm	37 nm	29%	Fig. 3-1 (d, blue)
2	593 nm	33 nm	29%	Fig. 3-2 (b, blue)
3	651 nm	60 nm	65%	Figs. 3-3 (a, b, c, d, blue)

Table 3-2. List of optical properties of core/shell QDs (continued).

No.	PL peak position (core/shell)	FWHM	PL QY	Data
4	676 nm	55 nm	60%	Fig. 3-3 (c, purple)
5	602 nm	57 nm	62%	Fig. 3-3 (c, green)
6	676 nm	63 nm	28%	Fig. 3-3 (d, light green)
7	677 nm	92 nm	13%	Fig. 3-3 (d, orange)

Structurally, the TEM image reveals that the core QDs exhibit a diameter of 5.2 ± 0.8 nm (**Figs. 3-4 (a, b)**), a size akin to the QDs synthesized without the Cu precursors. The formation of the Ga–S shell led to a nearly 3 nm increase in particle size (**Figs. 3-4 (c, d)**). Compositionally, the Cu content was found to be 5–30% higher than the composition ratios of the starting materials (**Table 3-3**). Conversely, the ratio of In/Ga in the core/shell QDs varied inconsistently, hindering a quantitative evaluation from the composition. This problem is a common occurrence in the analysis of QDs synthesized by Ag-source injection, where the excessive and inseparable formation of In, Ga, and S materials obstructs the compositional analysis.[75] To address this, XRD measurements were conducted for a representative sample (No. 5 in **Table 3-1**) as illustrated in **Fig. 3-5**. The peak of the (112) plane located at 27.4°; this is in reasonable agreement with the expected peak for the alloy, interpolated from the corresponding peaks of $AgInS_2$ (26.7°), $AgGaS_2$ (27.9°), and $CuInS_2$ (27.9°). These results suggest that, at least for the crystalline part of the core, the product is formed in accordance with the composition ratio of the raw materials.

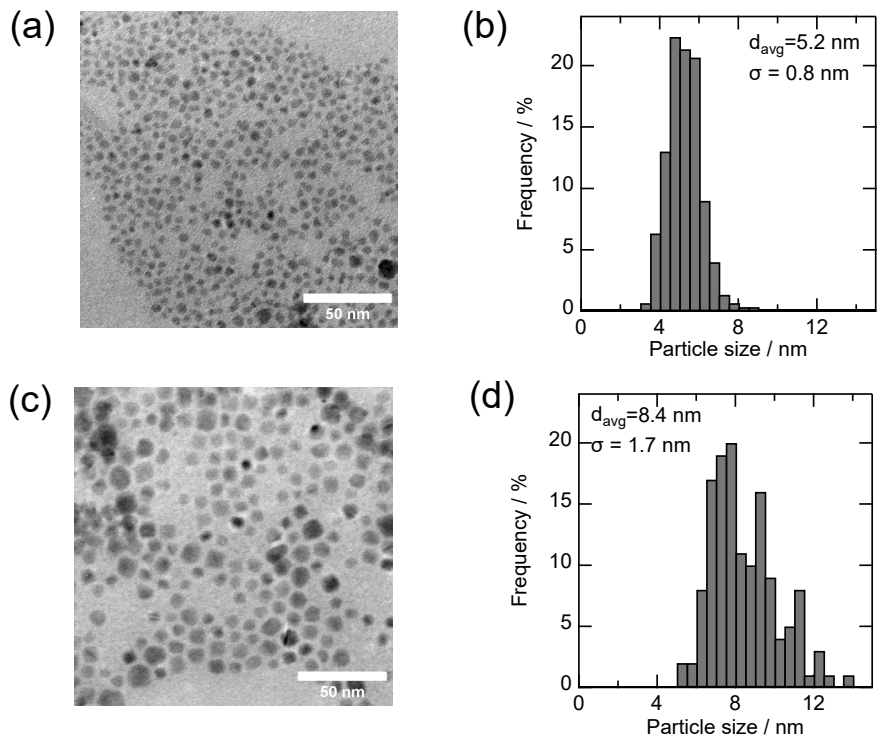

Figure 3-4. (a, c) TEM images and (b, d) size histograms of (a, b) core and (c, d) core/shell QDs corresponding to the samples whose spectra are presented in **Figs. 3-3 (a, b)**.

Table 3-3. List of compositional ratios of core/shell QDs (Ag+Cu = 1.00).

Sample No.	Atomic ratio				
	Ag	Cu	In	Ga	S
3	0.87	0.13	0.66	1.2	3.1
5	0.89	0.11	0.79	1.1	2.9
6	0.57	0.43	1.0	1.3	4.1
7	0.47	0.53	0.60	0.61	2.2

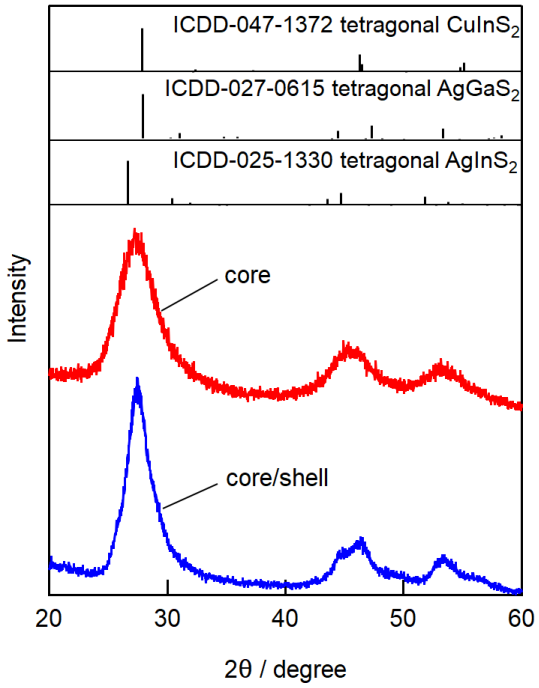

Figure 3-5. XRD patterns for sample No. 5 (Ag/Cu = 0.225/0.025 and In/Ga = 0.2/0.2) in both core and core/shell QDs. The peak at 27.4° for the (112) plane is reasonable considering the corresponding peaks of the three materials: tetragonal $AgInS_2$ (26.7°), $AgGaS_2$ (27.9°), and $CuInS_2$ (27.9°).

3.3.3 Optical properties and origin of PL

To investigate the cause of the slightly broader PL, I performed PL lifetime measurements. **Figure 3-6** shows the decay curves of Ag–In–Ga–S/Ga–S (with different In/Ga ratios) and Ag–Cu–In–Ga–S/Ga–S core/shell QDs recorded at the PL peak wavelength of each sample. The decay components after fitting with bi- or tri-exponential equations (equation 2-2) were summarized in **Table 3-4**. The Ag–In–Ga–S/Ga–S core/shell QDs (528 nm, high Ga content) could be fitted with the two components with the shortest lifetime around 63.8 ns (τ_1), which can be attributed to the band-edge PL.[52, 75] The Ag–In–Ga–S/ Ga–S core/shell QDs (593 nm, low Ga content) was well-fitted with the tri-exponential equation with the shortest lifetime of ca. 50 ns. The elongation of apparent decay time in the single logarithm graph (**Fig. 3-6 (a)**) is mainly due to the increased contribution of the 2296 ns

component (τ_3), originating from an unignorable increase in defect PL (**Fig. 3-2 (b)**). The increase in the ratio of the ~400 ns decay component (A_2) might be due to orbital splitting caused by ligands, crystal fields and electron–hole exchange interactions,[123-126] while the contribution of sharrow trap sites could also be a factor.[67, 86] The Ag–Cu–In–Ga–S/Ga–S core/shell QDs also exhibited three emission components. However, the shortest lifetime component (τ_1) was three times longer than the Cu-free counterparts, suggesting that an incorporation of Cu considerably changed the emission mechanism. This evidence led us to speculate that the radiation from the Cu-containing QDs derives from the localized states, which provide a recombination rate slower than band-edge transition, as shown in **Fig. 3-6 (b)**.

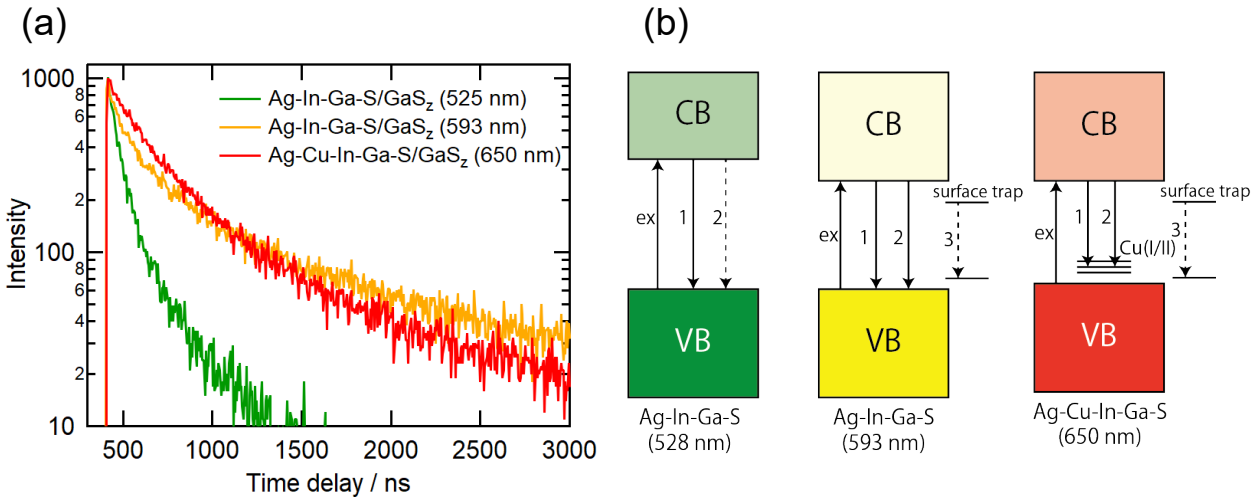

Figure 3-6. (a) PL decay curves for Ag–In–Ga–S/ Ga–S (with green and yellow PL) and Ag–Cu–In–Ga–S/Ga–S core/shell QDs. Samples were excited at 405 nm and the data were recorded at PL peak wavelength of each sample. (b) Schematic of the PL mechanism for the three samples. Numbers 1–3 in the figure correspond to the decay components in **Table 3-4**. Insignificant transition paths were shown as dashed lines.

Table 3-4. PL lifetime components of Ag–In–Ga–S/Ga–S QDs (different Ga/In ratios) and Ag–Cu–In–Ga–S/Ga–S core/shell QDs.

Sample (PL peak)	τ_1/ns	τ_2/ns	τ_3/ns	A_1	A_2	A_3	χ^2
Ag–In–Ga–S[a] /Ga–S (528 nm)	63.8	373	–	0.89	0.11	–	1.00
Ag–In–Ga–S[b] /Ga–S (593 nm)	48.4	394	2296	0.55	0.36	0.09	1.23
Ag–Cu–In–Ga–S /Ga–S (650 nm)	142	411	1880	0.48	0.46	0.06	1.18

[a] Core/shell QDs with high Ga content. The sample described in previous work[75].

[b] Core/shell QDs with low Ga content whose spectrum displayed in **Figs. 3-2 (a, b)**.

Before the achievement of the band-edge PL from AIS QDs, the origin of defective PL from the groups 11–13–16 semiconductor has been mostly considered to be point defects in the crystal lattice.[127-129] Specifically, the Cu(II) sites that are created in $CuInS_2$ QDs during or after synthesis, despite a formal charge of Cu(I), generate an energy level close to the VB. The "free-to-bound" transition between electrons in the CB and the Cu(II) levels was thought to be responsible for the observed broadband PL.[130-131] Among relevant reports, however, Knowles et al. focused on the similarity of PL properties between $CuInS_2$ QDs and Cu(I)-doped CdS QDs, and then considered that Cu(II) point defects (at ground state) is not necessarily required for the transition via Cu sites.[132] Based to their considerations, when the $CuInS_2$ QDs undergo photoexcitation to form excitons, holes become localized at temporarily generated Cu(II) sites. This phenomenon occurs as a result of the robust electron-phonon coupling, which significantly stabilizes the situation of localized holes in comparison to the carrier delocalization energy. This localized state was referred to as self-trapped excitons, and was considered to be the cause of broadband PL. A subsequent study by Hughes et al. pointed

that Cu(I) doping to AIS QDs also generates Cu3d-derived orbitals near the VB, and recombination occurs through these levels.[119] To determine the cause of the PL, which is broad and consists of multiple lifetime components, Knowles et al. performed magneto-optical measurements and found that the self-trapped excitons show singlet and triplet-like behaviors.[132] Nevertheless, the cryogenic measurements revealed a singlet-triplet splitting energy (ΔE_{ST}) that was considerably smaller than the thermal activation energy at ambient temperature. This resulted in an equal occupancy of the two energy levels, thereby facilitating preferential recombination from the singlet state due to its faster recombination kinetics. The observed variations in decay kinetics were rather attributed to the position of the trapped hole. Due to the wavefunction overlap with delocalized electrons in the CB, which have a 1s orbital-like wavefunction, the recombination is more efficient when the hole trap sites are located in the center of the nanoparticle rather than at the outer edge.[133]

XPS measurements revealed that the oxidation state of copper in Ag–Cu–In–Ga–S QDs was in the Cu(I) oxidation state (binding energy of 932 eV) rather than Cu(II) (binding energies of 933–935 eV), as shown in **Fig. 3-7**. This confirmation supports the hypothesis that photoluminescence (PL) arises from self-trapped excitons. Following this understanding, I can discuss the shifts in PL shown in **Figs. 3-3 (c, d)**. Density functional theory (DFT) calculations have predicted that, within the group 11–13–16 semiconductor system, which includes $CuInS_2$, AIS, and $AgGaS_2$, the CB edge is primarily composed of In, Ga, and to a lesser extent S. Conversely, the VB edge consists of Cu, Ag, and S.[119, 134] Hence, the energy of the CB edge is primarily affected by changes in the In/Ga ratio,[134] while the Cu/Ag ratio chiefly determines the energy of the VB edge.[119] Assuming that the Cu levels near the VB are less sensitive to shifts in band positions, changes in the emission wavelength can be significantly influenced by variations in the In/Ga ratio, which impacts the energy of the CB. Conversely, alterations in the Ag/Cu ratio have a negligible effect on the central emission

wavelength (see **Fig. 3-8**). Furthermore, the broadening of the PL at higher Cu ratios can logically be attributed to the increase in Cu sites, which exhibit energy variations based on their positioning within the particles.[133] In contrast, the spectral width of the Ag–Cu–In–Ga–S/Ga–S core/shell QDs was found to be narrower (55–60 nm) than the width reported for the core-only $Ag_{1-x}Cu_xInS_2$ QDs (ca. 200 nm).[119] This can be attributed to the presence of the gallium sulfide shell, which removes potential surface defects near the CB edge, thereby promoting pure free-to-bound transition PL.

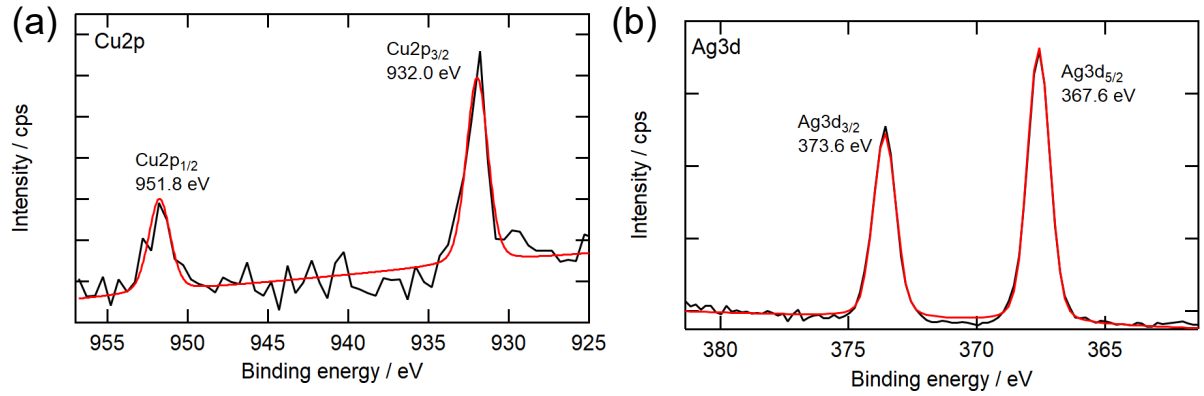

Figure 3-7. XPS spectra of Ag–Cu–In–Ga–S QDs for Cu2p and Ag3d regions

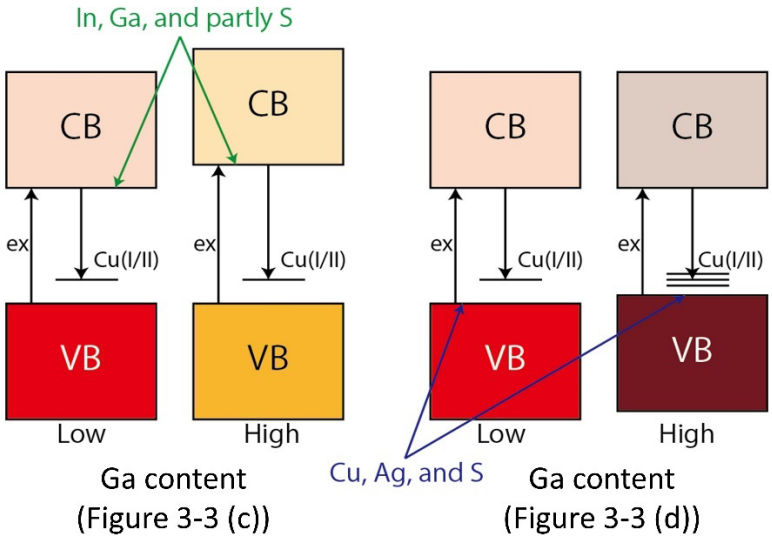

Figure 3-8. Schematic of the PL mechanism for the samples shown in **Figs. 3-3 (c, d)**.

3.3.4 Electroluminescence (EL)

To further demonstrate the potential of this red luminescent material, I fabricated QD-LEDs by using the Ag–Cu–In–Ga–S/Ga–S core/shell QDs. These were prepared following the protocol for sample No. 3 (**Table 3-1)** but on a larger scale. The structure of the devices was identical to that reported in the previous studies, with the EML comprising solely Ag–Cu–In–Ga–S/Ga–S core/shell QDs, without the inclusion of any additional materials to aid charge transport (**Fig. 3-9 (a)**).[121, 135-136] The scanning TEM (STEM) image illustrates the formation of a uniform QD layer, with an average thickness of two monolayers (**Fig. 3-9 (b)**). The device exhibited an electroluminescence (EL) spectrum identical to the PL of the QD solution (**Figs. 3-9 (c)** and **3-10 (a)**). As shown in **Fig. 3-9 (d)**, the luminance–voltage curve shows a turn-on voltage of 2.2 V for this device. This is slightly above the actual photon energy (660 nm, 1.9 eV) but close to the PL energy of the Ag–Cu–In–Ga–S/Ga–S core/shell QDs prepared with a similar In/Ga ratio, without using Cu species (sample no. 2, 593 nm, 2.1 eV). It was hypothesized that charge injection occurred via the CB and VB of the core QDs, rather than direct injection into the Cu levels present in the cores (this discussion may underestimate the resistance in the cell). The device achieved a maximum external quantum efficiency (EQE) of 1.77%, superior to yellow-emitting devices using AIS/Ga–S core/shell QDs and green-emitting devices (**Fig. 3-9 (e)**).[121, 136] Compared with these previous instances, where defective emission was more pronounced in EL than in PL, the Cu-containing QDs exhibited pure free-to-bound emission. Although this phenomenon cannot be fully explained, it could likely be caused by easier electron injection than that in green-emitting QDs, and the fact that the emission energy closely matches the defect emission energy of the green and yellow QDs. These conditions result in pure-red EL with chromaticity coordinates (0.710, 0.289), which satisfy the recommendation ITU-R BT.2020 standard (**Figs. 3-9 (f)** and **3-10 (b)**).

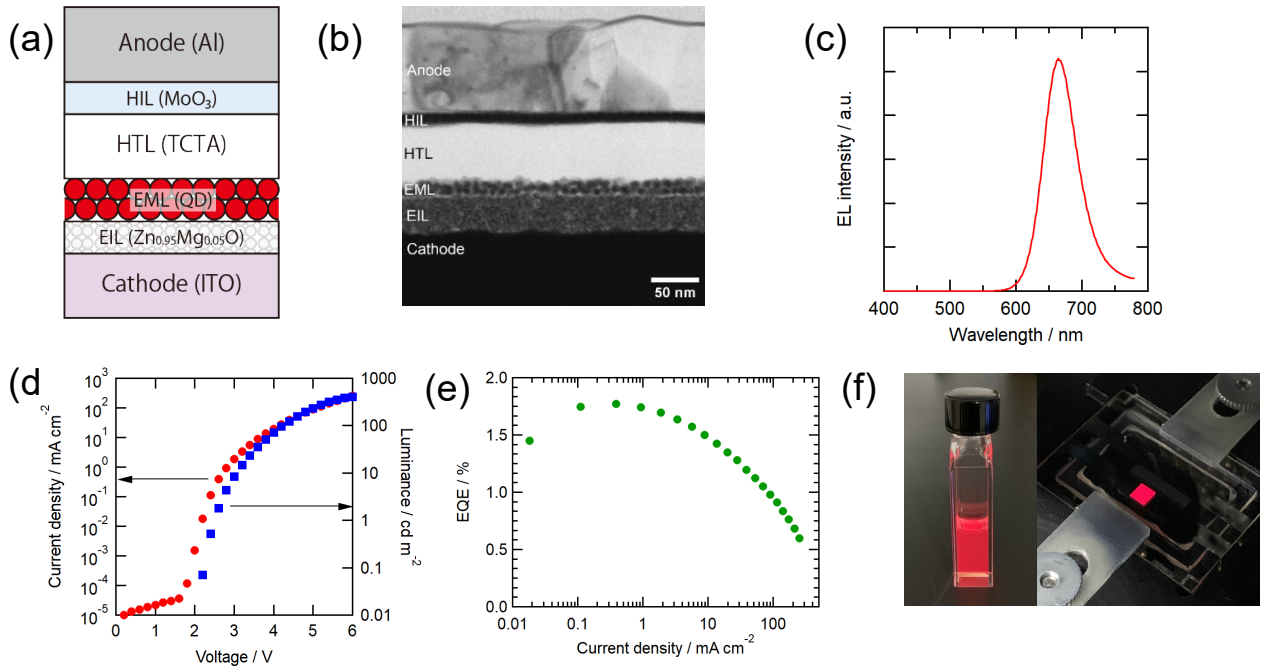

Figure 3-9. (a) Schematic representation and (b) cross-sectional STEM image of the device. (c) EL spectra at 6.0 V; (d) comprehensive voltage–current–luminance plots; and (e) the variation of EQE with respect to current density. (f) Photographs of QD solution and EL device.

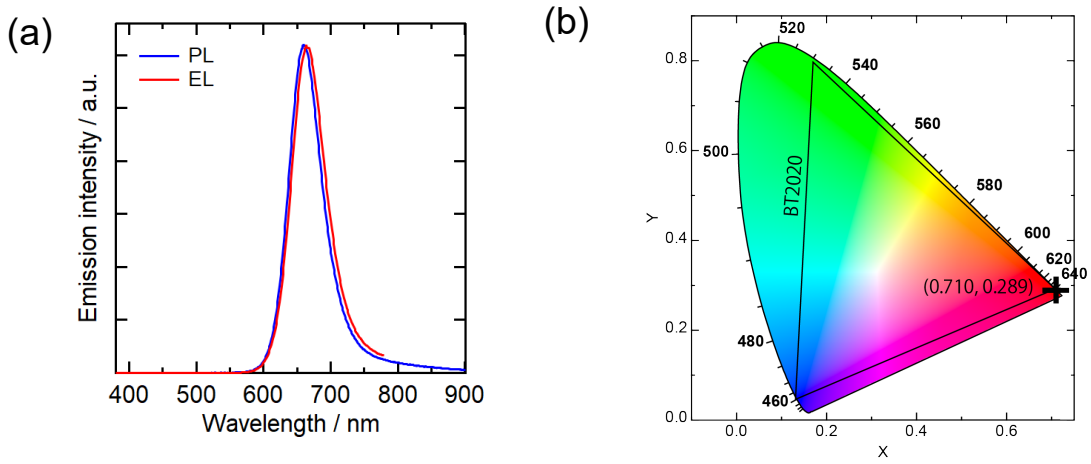

Figure 3-10. (a) Comparison of solution PL spectrum and EL spectrum. (b) CIE color coordinates (0.710, 0289) of the QD-LED corresponding to the spectrum in **Fig. 3-9 (c)**. The triangle indicates the BT.2020 standard.

3.4 Summary

I successfully synthesized Ag–Cu–In–Ga–S/Ga–S core/shell QDs through the injection of a mixture of Ag and Cu sources into a heated solution containing In, Ga, and S sources. This process generated quinary nanoparticles without the formation of precipitated byproducts, thus simplifying purification steps and facilitating scale-up that is well-suited for QD applications. Upon coating with Ga–S shells, the QDs displayed a red-colored PL with a spectral FWHM as narrow as 55 nm. Variation of PL decay profile and PL wavelength shifts when adjusting Cu/Ag ratio suggest that the emission arises from a localized carrier, rather than the band-edge transition observed in Ag–In–Ga–S/Ga–S core/shell QDs. Consistent with previous reports, Cu-containing QDs appear to undergo hole localization, resulting in the formation of self-trapped excitons. These results are supported by the presence of Cu(I) species in the core QDs. Moreover, the QD-LED device utilizing the core/shell QDs demonstrated red EL with high color purity that meets the BT2020 standard.

Conclusions

In this study, the redshift of the PL wavelength of AIS-based QDs was successfully achieved by the different band-engineering procedures as follows.

Chapter 1 described the wavelength shift due to the type II/quasi-type II band alignment. After the Ga–Se shell coating, a narrow PL spectrum was obtained due to the surface passivation by the Ga–Se shell. The staggered band alignment of AIS/Ga–Se core/shell QDs redshifted the PL wavelength to 681 nm, which was significantly longer than the band-edge emission of AIS/Ga–S core/shell QDs (575–585 nm). The prolonged PL decay time was the evidence for the indirect transition of the type II core/shell QDs. Although the PL QY was low, it increased to 25% after HCl treatment due to the reduction of electronic trap states at the core/shell interface and in the shell. On the other hand, the PL spectrum exhibited a further redshift and the PL lifetime became shorter. The ICP–AES and XRD results revealed S/Se substitution in the core QDs, resulting in the formation of an Ag–In–S–Se alloy core. This alloying shifted the VB potential of the core to higher energy and changed the band alignment to quasi-type II. The luminescence color could be tuned by controlling the composition of S and Se in the Ga–S–Se shells.

Chapter 2 described the redshift of AIS-based core/graded shell QDs by coating the AIS core with the In–S shell prior to the Ga–S shell. The presence of the In–S shell as the inner shell could alter the PL characteristics after the Ga–S coating. After the In–S shell coating, the QDs exhibited PL at 593 nm, which is longer than the band-edge emission of AIS/Ga–S core/shell QDs. This redshift resulted from a small band offset between the core/shell interface, which broadened the charge wavefunctions to the In–S shell and reduced an effective size effect. Overcoating with the Ga–S shell exhibited a distinct band-edge PL at 602 nm. However, a significant decrease in In/Ga ratio occurred due to In/Ga substitution at

the core/shell interface. Typically, the decrease in In/Ga ratio in the core increases the bandgap of the AIS QDs. These inconsistent results were explained by the formation of shells with graded composition. It stretched the electron and hole wavefunctions, resulting in a PL redshift. By increasing the temperature for In–S shell coating, the thickness of the In–S shell increased. Although the decrease in In content still occurred after Ga–S shell coating, the PL redshift persisted. Finally, a 40-nm redshift was achieved compared to the band-edge PL of AIS/Ga–S core/shell QDs.

Chapter 3 described the PL redshift by introducing Cu into Ag–In–Ga–S cores. The Ag–Cu–In–Ga–S core QDs were prepared by the injection of Ag and Cu mixture into a hot solution of In, Ga and S precursors. Remarkably, the highly monodisperse QDs were generated without precipitate. Upon Ga–S shell coating, the core/shell QDs exhibited a red-colored emission with a narrow FWHM of 55 nm. The variation of PL spectra and PL decay profiles revealed that the emission originated from the transition of excited electrons in CB to Cu(II) level near the VB. These results were consistent with previous reports of Cu-containing QDs, which underwent hole localization and formed self-trapped excitons. This finding was supported by the presence of Cu(I) species in core QDs. Additionally, the QD-LED fabricated by the Ag–Cu–In–Ga–S/Ga–S core/shell QDs exhibited red EL emission with high color purity that meets the BT2020 standard.

References

1. Electronic Conductivity in Solids. In *Understanding Solids*, 2004; pp 391-429.
2. Serpone, N.; Emeline, A. V., Semiconductor Photocatalysis — Past, Present, and Future Outlook. *The Journal of Physical Chemistry Letters* **2012,** *3* (5), 673-677.
3. Kudo, A.; Miseki, Y., Heterogeneous Photocatalyst Materials for Water Splitting. *Chemical Society Reviews* **2009,** *38* (1), 253-278.
4. Fan, W.; Zhang, Q.; Wang, Y., Semiconductor-based Nanocomposites for Photocatalytic H_2 Production and CO_2 Conversion. *Physical Chemistry Chemical Physics* **2013,** *15* (8), 2632-2649.
5. Rogach, A. L.; Gaponik, N.; Lupton, J. M.; Bertoni, C.; Gallardo, D. E.; Dunn, S.; Li Pira, N.; Paderi, M.; Repetto, P.; Romanov, S. G.; O'Dwyer, C.; Sotomayor Torres, C. M.; Eychmüller, A., Light-Emitting Diodes with Semiconductor Nanocrystals. *Angewandte Chemie International Edition* **2008,** *47* (35), 6538-6549.
6. Green, M., Semiconductor Quantum Dots as Biological Imaging Agents. *Angewandte Chemie International Edition* **2004,** *43* (32), 4129-4131.
7. Nakata, K.; Fujishima, A., TiO_2 Photocatalysis: Design and Applications. *Journal of Photochemistry and Photobiology C: Photochemistry Reviews* **2012,** *13* (3), 169-189.
8. Guo, Q.; Zhou, C.; Ma, Z.; Yang, X., Fundamentals of TiO_2 Photocatalysis: Concepts, Mechanisms, and Challenges. *Advanced materials* **2019,** *31* (50), 1901997.
9. Lee, K. M.; Lai, C. W.; Ngai, K. S.; Juan, J. C., Recent Developments of Zinc Oxide Based Photocatalyst in Water Treatment Technology: A Review. *Water Research* **2016,** *88*, 428-448.
10. Gu, X.; Li, C.; Yuan, S.; Ma, M.; Qiang, Y.; Zhu, J., ZnO based Heterojunctions and Their Application in Environmental Photocatalysis. *Nanotechnology* **2016,** *27* (40), 402001.

11. Wenderich, K.; Mul, G., Methods, Mechanism, and Applications of Photodeposition in Photocatalysis: A Review. *Chemical Reviews* **2016,** *116* (23), 14587-14619.

12. Yang, H., A Short Review on Heterojunction Photocatalysts: Carrier Transfer Behavior and Photocatalytic Mechanisms. *Materials Research Bulletin* **2021,** *142*, 111406.

13. Hoffmann, M. R.; Martin, S. T.; Choi, W.; Bahnemann, D. W., Environmental Applications of Semiconductor Photocatalysis. *Chemical Reviews* **1995,** *95* (1), 69-96.

14. Ekimov, A. I.; Onushchenko, A. A., Quantum Size Effect in Three-Dimensional Microscopic Semiconductor Crystals. *Journal of Experimental and Theoretical Physics Letters* **1981,** *34*, 345-349.

15. Ekimov, A. I.; Efros, A. L.; Onushchenko, A. A., Quantum Size Effect in Semiconductor Microcrystals. *Solid State Communications* **1985,** *56* (11), 921-924.

16. Efros, A. L.; Brus, L. E., Nanocrystal Quantum Dots: From Discovery to Modern Development. *ACS Nano* **2021,** *15* (4), 6192-6210.

17. Ngo, C. Y.; Yoon, S. F.; Fan, W. J.; Chua, S. J., Effects of Size and Shape on Electronic States of Quantum Dots. *Physical Review B* **2006,** *74* (24), 245331.

18. Henglein, A., Photo-Degradation and Fluorescence of Colloidal-Cadmium Sulfide in Aqueous Solution. *Berichte der Bunsengesellschaft für physikalische Chemie* **1982,** *86* (4), 301-305.

19. Brus, L. E., A Simple Model for the Ionization Potential, Electron Affinity, and Aqueous Redox Potentials of Small Semiconductor Crystallites. *The Journal of Chemical Physics* **1983,** *79* (11), 5566-5571.

20. Murray, C. B.; Norris, D. J.; Bawendi, M. G., Synthesis and Characterization of Nearly Monodisperse CdE (E = Sulfur, Selenium, Tellurium) Semiconductor Nanocrystallites. *Journal of the American Chemical Society* **1993,** *115* (19), 8706-8715.

21. Smith, A. M.; Nie, S., Semiconductor Nanocrystals: Structure, Properties, and Band Gap Engineering. *Accounts of Chemical Research* **2010,** *43* (2), 190-200.

22. Rice, Q.; Raut, S.; Burney, K.; Gryczynski, Z.; Gryczynski, I.; Yu, W. W.; Tabibi, B.; Seo, J., Time-Resolved and Temperature-Dependent Fractional Amplitude Contributions to the Broadband Emission of CdSe Quantum Dots. *Crystals* **2021,** *11* (11), 1284.

23. de Mello Donegá, C.; Hickey, S. G.; Wuister, S. F.; Vanmaekelbergh, D.; Meijerink, A., Single-Step Synthesis to Control the Photoluminescence Quantum Yield and Size Dispersion of CdSe Nanocrystals. *The Journal of Physical Chemistry B* **2003,** *107* (2), 489-496.

24. Peng, X.; Manna, L.; Yang, W.; Wickham, J.; Scher, E.; Kadavanich, A.; Alivisatos, A. P., Shape Control of CdSe Nanocrystals. *Nature* **2000,** *404* (6773), 59-61.

25. Xu, L.; Yuan, S.; Zeng, H.; Song, J., A Comprehensive Review of Doping in Perovskite Nanocrystals/Quantum Dots: Evolution of Structure, Electronics, Optics, and Light-Emitting Diodes. *Materials Today Nano* **2019,** *6*, 100036.

26. Lechner, R. T.; Fritz-Popovski, G.; Yarema, M.; Heiss, W.; Hoell, A.; Schülli, T. U.; Primetzhofer, D.; Eibelhuber, M.; Paris, O., Crystal Phase Transitions in the Shell of PbS/CdS Core/Shell Nanocrystals Influences Photoluminescence Intensity. *Chemistry of Materials* **2014,** *26* (20), 5914-5922.

27. Zhou, J.; Liu, Y.; Tang, J.; Tang, W., Surface Ligands Engineering of Semiconductor Quantum Dots for Chemosensory and Biological Applications. *Materials Today* **2017,** *20* (7), 360-376.

28. Wehrenberg, B. L.; Wang, C.; Guyot-Sionnest, P., Interband and Intraband Optical Studies of PbSe Colloidal Quantum Dots. *The Journal of Physical Chemistry B* **2002,** *106* (41), 10634-10640.

29. Kirkwood, N.; Monchen, J. O. V.; Crisp, R. W.; Grimaldi, G.; Bergstein, H. A. C.; du Fossé, I.; van der Stam, W.; Infante, I.; Houtepen, A. J., Finding and Fixing Traps in II–VI and III–V Colloidal Quantum Dots: The Importance of Z-Type Ligand Passivation. *Journal of the American Chemical Society* **2018,** *140* (46), 15712-15723.

30. Rosenthal, S. J.; Chang, J. C.; Kovtun, O.; McBride, J. R.; Tomlinson, I. D., Biocompatible Quantum Dots for Biological Applications. *Chemistry & Biology* **2011,** *18* (1), 10-24.

31. Byers, R. J.; Hitchman, E. R., Quantum Dots Brighten Biological Imaging. *Progress in Histochemistry and Cytochemistry* **2011,** *45* (4), 201-237.

32. Laurand, N.; Guilhabert, B.; McKendry, J.; Kelly, A. E.; Rae, B.; Massoubre, D.; Gong, Z.; Gu, E.; Henderson, R.; Dawson, M. D., Colloidal Quantum Dot Nanocomposites for Visible Wavelength Conversion of Modulated Optical Signals. *Optical Materials Express* **2012,** *2* (3), 250-260.

33. Qasaimeh, O., Characteristics of Cross-gain (XG) Wavelength Conversion in Quantum Dot Semiconductor Optical Amplifiers. *IEEE Photonics Technology Letters* **2004,** *16* (2), 542-544.

34. Bang, S. Y.; Suh, Y.-H.; Fan, X.-B.; Shin, D.-W.; Lee, S.; Choi, H. W.; Lee, T. H.; Yang, J.; Zhan, S.; Harden-Chaters, W.; Samarakoon, C.; Occhipinti, L. G.; Han, S. D.; Jung, S.-M.; Kim, J. M., Technology Progress on Quantum Dot Light-Emitting Diodes for Next-generation Displays. *Nanoscale Horizons* **2021,** *6* (2), 68-77.

35. Todescato, F.; Fortunati, I.; Minotto, A.; Signorini, R.; Jasieniak, J. J.; Bozio, R., Engineering of Semiconductor Nanocrystals for Light Emitting Applications. *Materials* **2016,** *9* (8), 672.

36. Rabouw, F. T.; de Mello Donega, C., Excited-State Dynamics in Colloidal Semiconductor Nanocrystals. *Topics in Current Chemistry* **2016,** *374* (5), 58.

37. Peter Atkins, J. d. P., Physical Chemistry, Eighth Edition. In *Physical Chemistry, Eighth Edition*, Press, O. U., Ed. 2006; pp 246-319.

38. Nosaka, Y., Finite Depth Spherical Well Model for Excited States of Ultrasmall Semiconductor Particles: An Application. *The Journal of Physical Chemistry* **1991,** *95* (13), 5054-5058.

39. Nanda, K. K.; Kruis, F. E.; Fissan, H., Energy Levels in Embedded Semiconductor Nanoparticles and Nanowires. *Nano Letters* **2001,** *1* (11), 605-611.

40. Pellegrini, G.; Mattei, G.; Mazzoldi, P., Finite Depth Square Well Model: Applicability and Limitations. *Journal of Applied Physics* **2005,** *97* (7), 073706.

41. Aguilera, M. L. A.; Hernández, J. R. A.; Trujillo, M. A. G.; López, M. O.; Puente, G. C., Photoluminescence Studies of Chalcopyrite and Orthorhombic $AgInS_2$ Thin Films Deposited by Spray Pyrolysis Technique. *Thin Solid Films* **2007,** *515* (15), 6272-6275.

42. Torimoto, T.; Kameyama, T.; Kuwabata, S., Photofunctional Materials Fabricated with Chalcopyrite-Type Semiconductor Nanoparticles Composed of $AgInS_2$ and Its Solid Solutions. *Journal of Physical Chemistry Letters* **2014,** *5* (2), 336-347.

43. Yarema, O.; Yarema, M.; Wood, V., Tuning the Composition of Multicomponent Semiconductor Nanocrystals: The Case of I–III–VI Materials. *Chemistry of Materials* **2018,** *30* (5), 1446-1461.

44. Torimoto, T.; Adachi, T.; Okazaki, K.-i.; Sakuraoka, M.; Shibayama, T.; Ohtani, B.; Kudo, A.; Kuwabata, S., Facile Synthesis of ZnS−$AgInS_2$ Solid Solution Nanoparticles for a Color-Adjustable Luminophore. *Journal of the American Chemical Society* **2007,** *129* (41), 12388-12389.

45. Pal, B. N.; Ghosh, Y.; Brovelli, S.; Laocharoensuk, R.; Klimov, V. I.; Hollingsworth, J. A.; Htoon, H., 'Giant' CdSe/CdS Core/Shell Nanocrystal Quantum Dots as Efficient

Electroluminescent Materials: Strong Influence of Shell Thickness on Light-Emitting Diode Performance. *Nano Letters* **2012,** *12* (1), 331-336.

46. Maestro, L. M.; Rodríguez, E. M.; Rodríguez, F. S.; la Cruz, M. C. I.-d.; Juarranz, A.; Naccache, R.; Vetrone, F.; Jaque, D.; Capobianco, J. A.; Solé, J. G., CdSe Quantum Dots for Two-Photon Fluorescence Thermal Imaging. *Nano Letters* **2010,** *10* (12), 5109-5115.
47. Uematsu, T.; Kitajima, H.; Kohma, T.; Torimoto, T.; Tachibana, Y.; Kuwabata, S., Tuning of the Fluorescence Wavelength of CdTe Quantum Dots with 2 nm Resolution by Size-Selective Photoetching. *Nanotechnology* **2009,** *20* (21), 215302.
48. Wang; Zhang, H.; Zhang; Li; Sun; Yang, B., Application of Ultrasonic Irradiation in Aqueous Synthesis of Highly Fluorescent CdTe/CdS Core−Shell Nanocrystals. *The Journal of Physical Chemistry C* **2007,** *111* (6), 2465-2469.
49. Moreels, I.; Justo, Y.; De Geyter, B.; Haustraete, K.; Martins, J. C.; Hens, Z., Size-Tunable, Bright, and Stable PbS Quantum Dots: A Surface Chemistry Study. *ACS Nano* **2011,** *5* (3), 2004-2012.
50. Gong, M.; Li, F.; Wang, L.; Xu, Q.; Wu, Z.; Shen, H.; Li, L. S.; Du, Z., Highly Monodisperse PbS Quantum Dots with Facet Engineering for High-Radiance Light-Emitting Diodes in the NIR-II Window. *ACS Photonics* **2023,** *10* (7), 2241-2248.
51. Hoisang, W.; Uematsu, T.; Yamamoto, T.; Torimoto, T.; Kuwabata, S., Core Nanoparticle Engineering for Narrower and More Intense Band-Edge Emission from $AgInS_2/GaS_x$ Core/Shell Quantum Dots. *Nanomaterials* **2019,** *9* (12), 1763.
52. Uematsu, T.; Wajima, K.; Sharma, D. K.; Hirata, S.; Yamamoto, T.; Kameyama, T.; Vacha, M.; Torimoto, T.; Kuwabata, S., Narrow Band-Edge Photoluminescence from $AgInS_2$ Semiconductor Nanoparticles by the Formation of Amorphous III–VI Semiconductor Shells. *NPG Asia Materials* **2018,** *10* (8), 713-726.

53. AbouElhamd, A. R.; Al-Sallal, K. A.; Hassan, A., Review of Core/Shell Quantum Dots Technology Integrated into Building's Glazing. *Energies* **2019,** *12* (6), 1058.

54. Reiss, P.; Protière, M.; Li, L., Core/Shell Semiconductor Nanocrystals. *Small* **2009,** *5* (2), 154-168.

55. Raevskaya, A.; Lesnyak, V.; Haubold, D.; Dzhagan, V.; Stroyuk, O.; Gaponik, N.; Zahn, D. R. T.; Eychmüller, A., A Fine Size Selection of Brightly Luminescent Water-Soluble Ag–In–S and Ag–In–S/ZnS Quantum Dots. *The Journal of Physical Chemistry C* **2017,** *121* (16), 9032-9042.

56. Wei, J.; Li, F.; Chang, C.; Zhang, Q., Synthesis of Emission Tunable $AgInS_2$/ZnS Quantum Dots and Application for Light Emitting Diodes. *Journal of Physics Communications* **2020,** *4* (4), 045016.

57. Song, J.; Ma, C.; Zhang, W.; Li, X.; Zhang, W.; Wu, R.; Cheng, X.; Ali, A.; Yang, M.; Zhu, L.; Xia, R.; Xu, X., Bandgap and Structure Engineering via Cation Exchange: From Binary Ag_2S to Ternary $AgInS_2$, Quaternary AgZnInS alloy and AgZnInS/ZnS Core/Shell Fluorescent Nanocrystals for Bioimaging. *ACS Applied Materials & Interfaces* **2016,** *8* (37), 24826-24836.

58. Bozyigit, D.; Wood, V., Challenges and Solutions for High-Efficiency Quantum Dot-based LEDs. *MRS Bulletin* **2013,** *38* (9), 731-736.

59. Anikeeva, P. O.; Halpert, J. E.; Bawendi, M. G.; Bulović, V., Electroluminescence from a Mixed Red−Green−Blue Colloidal Quantum Dot Monolayer. *Nano Letters* **2007,** *7* (8), 2196-2200.

60. Wu, T.; Sher, C.-W.; Lin, Y.; Lee, C.-F.; Liang, S.; Lu, Y.; Huang Chen, S.-W.; Guo, W.; Kuo, H.-C.; Chen, Z., Mini-LED and Micro-LED: Promising Candidates for the Next Generation Display Technology. *Applied Sciences* **2018,** *8* (9), 1557.

61. Wu, Y.; Ma, J.; Su, P.; Zhang, L.; Xia, B., Full-Color Realization of Micro-LED Displays. *Nanomaterials* **2020,** *10* (12), 2482.

62. Galiyeva, P.; Alem, H.; Rinnert, H.; Balan, L.; Blanchard, S.; Medjahdi, G.; Uralbekov, B.; Schneider, R., Highly Fluorescent, Color Tunable and Magnetic Quaternary Ag–In–Mn–Zn–S Quantum Dots. *Inorganic Chemistry Frontiers* **2019,** *6* (6), 1422-1431.

63. Yoon, S.-Y.; Kim, J.-H.; Jang, E.-P.; Lee, S.-H.; Jo, D.-Y.; Kim, Y.; Do, Y. R.; Yang, H., Systematic and Extensive Emission Tuning of Highly Efficient Cu–In–S-based Quantum Dots from Visible to Near Infrared. *Chemistry of Materials* **2019,** *31* (7), 2627-2634.

64. Jang, Y.; Shapiro, A.; Isarov, M.; Rubin-Brusilovski, A.; Safran, A.; Budniak, A. K.; Horani, F.; Dehnel, J.; Sashchiuk, A.; Lifshitz, E., Interface Control of Electronic and Optical Properties in IV–VI and II–VI Core/Shell Colloidal Quantum Dots: A Review. *Chemical Communications* **2017,** *53* (6), 1002-1024.

65. Li, X.; Shen, H.; Li, S.; Niu, J. Z.; Wang, H.; Li, L. S., Investigation on Type-II Cu_2S–CdS Core/shell Nanocrystals: Synthesis and Characterization. *Journal of Materials Chemistry* **2010,** *20* (5), 923-928.

66. Abdellah, M.; Žídek, K.; Zheng, K.; Chábera, P.; Messing, M. E.; Pullerits, T., Balancing Electron Transfer and Surface Passivation in Gradient CdSe/ZnS Core–Shell Quantum Dots Attached to ZnO. *The Journal of Physical Chemistry Letters* **2013,** *4* (11), 1760-1765.

67. Bae, W. K.; Char, K.; Hur, H.; Lee, S., Single-Step Synthesis of Quantum Dots with Chemical Composition Gradients. *Chemistry of Materials* **2008,** *20* (2), 531-539.

68. Leng, J.; Xu, Y.; Chan, Y.; Wang, P.; Ryuzaki, S.; Okamoto, K.; Tamada, K., Tuning the Emission Colors of Self-Assembled Quantum Dot Monolayers via One-Step Heat

Treatment for Display Applications. *ACS Applied Nano Materials* **2020,** *3* (4), 3214-3222.

69. Lu, Y.-H.; Lin, W.-H.; Yang, C.-Y.; Chiu, Y.-H.; Pu, Y.-C.; Lee, M.-H.; Tseng, Y.-C.; Hsu, Y.-J., A Facile Green Antisolvent Approach to Cu^{2+}-doped ZnO Nanocrystals with Visible-Light-Responsive Photoactivities. *Nanoscale* **2014,** *6* (15), 8796-8803.
70. Song, S.-W.; Lee, S.-H.; Jo, D.-Y.; Yoon, S.-Y.; Kim, H.-M.; Kim, Y.; Han, J.-N.; Lee, Y.-J.; Do, Y. R.; Yang, H., Single and Dual Doping of Blue-Emissive ZnSeTe Quantum Dots with Transition Metal Ions. *Advanced Optical Materials* **2022,** *10* (2), 2101767.
71. Zhong, H.; Bai, Z.; Zou, B., Tuning the Luminescence Properties of Colloidal I–III–VI Semiconductor Nanocrystals for Optoelectronics and Biotechnology Applications. *Journal of Physical Chemistry Letters* **2012,** *3* (21), 3167-3175.
72. Chang, J.-Y.; Wang, G.-Q.; Cheng, C.-Y.; Lin, W.-X.; Hsu, J.-C., Strategies for Photoluminescence Enhancement of $AgInS_2$ Quantum Dots and Their Application as Bioimaging Probes. *Journal of Materials Chemistry* **2012,** *22* (21), 10609-10618.
73. Sahu, A.; Kumar, D., Core-Shell Quantum Dots: A Review on Classification, Materials, Application, and Theoretical Modeling. *Journal of Alloys and Compounds* **2022,** *924*, 166508.
74. Hoisang, W.; Uematsu, T.; Torimoto, T.; Kuwabata, S., Photoluminescence Stability Enhancement of Ag–In–Ga–S/GaS_x Core/Shell Quantum Dots with Thicker Shells by the Addition of Gallium Diethyldithiocarbamate. *Chemistry Letters* **2021,** *50* (11), 1863-1866.
75. Uematsu, T.; Tepakidareekul, M.; Hirano, T.; Torimoto, T.; Kuwabata, S., Facile High-Yield Synthesis of Ag–In–Ga–S Quaternary Quantum Dots and Coating with Gallium Sulfide Shells for Narrow Band-Edge Emission. *Chemistry of Materials* **2023,** *35* (3), 1094-1106.

76. Kameyama, T.; Yamauchi, H.; Yamamoto, T.; Mizumaki, T.; Yukawa, H.; Yamamoto, M.; Ikeda, S.; Uematsu, T.; Baba, Y.; Kuwabata, S.; Torimoto, T., Tailored Photoluminescence Properties of $Ag(In,Ga)Se_2$ Quantum Dots for Near-Infrared In Vivo Imaging. *ACS Applied Nano Materials* **2020,** *3* (4), 3275-3287.

77. Chuang, C.-H.; Lo, S. S.; Scholes, G. D.; Burda, C., Charge Separation and Recombination in CdTe/CdSe Core/Shell Nanocrystals as a Function of Shell Coverage: Probing the Onset of the Quasi Type-II Regime. *Journal of Physical Chemistry Letters* **2010,** *1* (17), 2530-2535.

78. Cao, J.; Jiang, Z.-J., Thickness-Dependent Shell Homogeneity of ZnSe/CdSe Core/Shell Nanocrystals and Their Spectroscopic and Electron- and Hole-Transfer Dynamics Properties. *Journal of Physical Chemistry C* **2020,** *124* (22), 12049-12064.

79. Ivanov, S. A.; Piryatinski, A.; Nanda, J.; Tretiak, S.; Zavadil, K. R.; Wallace, W. O.; Werder, D.; Klimov, V. I., Type-II Core/Shell CdS/ZnSe Nanocrystals: Synthesis, Electronic Structures, and Spectroscopic Properties. *Journal of the American Chemical Society* **2007,** *129* (38), 11708-11719.

80. Huang, D.; Persson, C., Photocatalyst $AgInS_2$ for Active Overall Water-Splitting: A First-Principles Study. *Chemical Physics Letters* **2014,** *591*, 189-192.

81. Cai, H.; Kang, J.; Sahin, H.; Chen, B.; Suslu, A.; Wu, K.; Peeters, F.; Meng, X.; Tongay, S., Exciton Pumping across Type-I Gallium Chalcogenide Heterojunctions. *Nanotechnology* **2016,** *27* (6), 065203.

82. Jung, C. S.; Park, K.; Shojaei, F.; Oh, J. Y.; Im, H. S.; Lee, J. A.; Jang, D. M.; Park, J.; Myoung, N.; Lee, C.-L.; Lee, J. W.; Song, J. K.; Kang, H. S., Photoluminescence and Photocurrents of $GaS_{1-x}Se_x$ Nanobelts. *Chemistry of Materials* **2016,** *28* (16), 5811-5820.

83. Tepakidareekul, M.; Uematsu, T.; Torimoto, T.; Kuwabata, S., Encapsulation of $AgInS_2/GaS_x$ Core/Shell Quantum Dots in In-Fumarate Metal–Organic Frameworks for Stability Enhancement. *CrystEngComm* **2022,** *24* (20), 3715-3723.

84. Kim, M.; Bang, J., Fabrication of Visible-Light Sensitized ZnTe/ZnSe (Core/Shell) Type-II Quantum Dots. *Journal of the Korean Ceramic Society* **2018,** *55* (5), 510-514.

85. Rismaningsih, N.; Yamauchi, H.; Kameyama, T.; Yamamoto, T.; Morita, S.; Yukawa, H.; Uematsu, T.; Baba, Y.; Kuwabata, S.; Torimoto, T., Photoluminescence Properties of Quinary Ag–(In,Ga)–(S,Se) Quantum Dots with a Gradient Alloy Structure for In Vivo Bioimaging. *Journal of Materials Chemistry C* **2021,** *9* (37), 12791-12801.

86. Bodunov, E. N.; Simões Gamboa, A. L., Photoluminescence Decay of Colloidal Quantum Dots: Reversible Trapping and the Nature of the Relevant Trap States. *Journal of Physical Chemistry C* **2019,** *123* (41), 25515-25523.

87. Chang, J. H.; Lee, H. J.; Rhee, S.; Hahm, D.; Jeong, B. G.; Nagamine, G.; Padilha, L. A.; Char, K.; Hwang, E.; Bae, W. K., Pushing the Band Gap Envelope of Quasi-Type II Heterostructured Nanocrystals to Blue: $ZnSe/ZnSe_{1-X}Te_X/ZnSe$ Spherical Quantum Wells. *Energy Material Advances* **2021,** *2021*, 3245731.

88. Murphy, C. J.; Coffer, J. L., Quantum Dots: A Primer. *Applied Spectroscopy* **2002,** *56* (1), 16A-27A.

89. Weller, H., Colloidal Semiconductor Q-Particles: Chemistry in the Transition Region Between Solid State and Molecules. *Angewandte Chemie International Edition in English* **1993,** *32* (1), 41-53.

90. Yu, W. W.; Qu, L.; Guo, W.; Peng, X., Experimental Determination of the Extinction Coefficient of CdTe, CdSe, and CdS Nanocrystals. *Chemistry of Materials* **2003,** *15* (14), 2854-2860.

91. Hamanaka, Y.; Ogawa, T.; Tsuzuki, M.; Kuzuya, T., Photoluminescence Properties and Its Origin of $AgInS_2$ Quantum Dots with Chalcopyrite Structure. *The Journal of Physical Chemistry C* **2011,** *115* (5), 1786-1792.

92. Hoisang, W.; Uematsu, T.; Torimoto, T.; Kuwabata, S., Luminescent Quaternary $Ag(In_xGa_{1-x})S_2/GaS_y$ Core/Shell Quantum Dots Prepared using Dithiocarbamate Compounds and Photoluminescence Recovery via Post Treatment. *Inorganic Chemistry* **2021,** *60* (17), 13101-13109.

93. Kameyama, T.; Kishi, M.; Miyamae, C.; Sharma, D. K.; Hirata, S.; Yamamoto, T.; Uematsu, T.; Vacha, M.; Kuwabata, S.; Torimoto, T., Wavelength-Tunable Band-Edge Photoluminescence of Nonstoichiometric Ag–In–S Nanoparticles via Ga^{3+} Doping. *ACS Applied Materials & Interfaces* **2018,** *10* (49), 42844-42855.

94. Torimoto, T.; Kameyama, T.; Uematsu, T.; Kuwabata, S., Controlling Optical Properties and Electronic Energy Structure of I–III–VI Semiconductor Quantum Dots for Improving Their Photofunctions. *Journal of Photochemistry and Photobiology C: Photochemistry Reviews* **2023,** *54*, 100569.

95. Krobkrong, N.; Uematsu, T.; Torimoto, T.; Kuwabata, S., Emission tuning of $AgInS_2$-based core/shell semiconductor quantum dots with type-II and quasi-type-II band alignments. *Japanese Journal of Applied Physics* **2023,** *62* (6), 061003.

96. Jung, J.; Lin, C. H.; Yoon, Y. J.; Malak, S. T.; Zhai, Y.; Thomas, E. L.; Vardeny, V.; Tsukruk, V. V.; Lin, Z., Crafting Core/Graded Shell–Shell Quantum Dots with Suppressed Re-absorption and Tunable Stokes Shift as High Optical Gain Materials. *Angewandte Chemie International Edition* **2016,** *55* (16), 5071-5075.

97. Park, K. H.; Jang, K.; Son, S. U., Synthesis, Optical Properties, and Self-Assembly of Ultrathin Hexagonal In_2S_3 Nanoplates. *Angewandte Chemie International Edition* **2006,** *45* (28), 4608-4612.

98. Cao, F.; Wang, S.; Wang, F.; Wu, Q.; Zhao, D.; Yang, X., A Layer-by-Layer Growth Strategy for Large-Size InP/ZnSe/ZnS Core–Shell Quantum Dots Enabling High-Efficiency Light-Emitting Diodes. *Chemistry of Materials* **2018,** *30* (21), 8002-8007.

99. Ho, C.-H.; Lin, M.-H.; Wang, Y.-P.; Huang, Y.-S., Synthesis of In_2S_3 and Ga_2S_3 crystals for oxygen sensing and UV photodetection. *Sensors and Actuators A: Physical* **2016,** *245*, 119-126.

100. Hamanaka, Y.; Ozawa, K.; Kuzuya, T., Enhancement of Donor–Acceptor Pair Emissions in Colloidal $AgInS_2$ Quantum Dots with High Concentrations of Defects. *The Journal of Physical Chemistry C* **2014,** *118* (26), 14562-14568.

101. Gao, N.; Zhang, R.; Chen, B.; Zhang, J.; Zhang, X.; Rogach, A. L., Template Synthesis of Silver Indium Sulfide Based Nanocrystals Performed through Cation Exchange in Organic and Aqueous Media. *Nano Research* **2021,** *14* (7), 2321-2329.

102. Tao, C.-L.; Xie, Z.; Xu, D.; Li, X.; Ge, F.; Chen, F.; Jiang, Z.; Gu, W.; Cheng, F.; Wu, X.-J., Templated Synthesis of Ultrathin Indium-based Ternary Metal Sulfide (MIn_2S_4, M = Zn, Cd, and Ni) Nanoplates for Photocatalytic Hydrogen Evolution. *ACS Applied Energy Materials* **2022,** *5* (4), 4877-4884.

103. De Geyter, B.; Justo, Y.; Moreels, I.; Lambert, K.; Smet, P. F.; Van Thourhout, D.; Houtepen, A. J.; Grodzinska, D.; de Mello Donega, C.; Meijerink, A.; Vanmaekelbergh, D.; Hens, Z., The Different Nature of Band Edge Absorption and Emission in Colloidal PbSe/CdSe Core/Shell Quantum Dots. *ACS Nano* **2011,** *5* (1), 58-66.

104. Boldt, K.; Kirkwood, N.; Beane, G. A.; Mulvaney, P., Synthesis of Highly Luminescent and Photo-Stable, Graded Shell $CdSe/Cd_xZn_{1-x}S$ Nanoparticles by In Situ Alloying. *Chemistry of Materials* **2013,** *25* (23), 4731-4738.

105. Boldt, K., Graded Shells in Semiconductor Nanocrystals. *Zeitschrift für Physikalische Chemie* **2017,** *231* (1), 77-92.

106. Márquez, R.; Rincón, C., On the Dielectric Constants of $A^{I}B^{III}C_2^{VI}$ Chalcopyrite Semiconductor Compounds. *Physica Status Solidi (B): Basic Research* **1995,** *191* (1), 115-119.

107. Liu, J.; Hua, E., Electronic Structure and Absolute Band Edge Position of Tetragonal $AgInS_2$ Photocatalyst: A Hybrid Density Functional Study. *Materials Science in Semiconductor Processing* **2015,** *40*, 446-452.

108. Márquez, R.; Rincón, C., On the Dielectric Constants of $A^{I}B^{III}C$ Chalcopyrite Semiconductor Compounds. *physica status solidi (b)* **1995,** *191* (1), 115-119.

109. Moodelly, D.; Kowalik, P.; Bujak, P.; Pron, A.; Reiss, P., Synthesis, Photophysical Properties and Surface Chemistry of Chalcopyrite-Type Semiconductor Nanocrystals. *Journal of Materials Chemistry C* **2019,** *7* (38), 11665-11709.

110. Click, S. M.; Rosenthal, S. J., Synthesis, Surface Chemistry, and Fluorescent Properties of InP Quantum Dots. *Chemistry of Materials* **2023,** *35* (3), 822-836.

111. Moon, H.; Lee, C.; Lee, W.; Kim, J.; Chae, H., Stability of Quantum Dots, Quantum Dot Films, and Quantum Dot Light-Emitting Diodes for Display Applications. *Advanced materials* **2019,** *31* (34), 1804294.

112. Xu, G.; Zeng, S.; Zhang, B.; Swihart, M. T.; Yong, K.-T.; Prasad, P. N., New Generation Cadmium-Free Quantum Dots for Biophotonics and Nanomedicine. *Chemical Reviews* **2016,** *116* (19), 12234-12327.

113. Won, Y.-H.; Cho, O.; Kim, T.; Chung, D.-Y.; Kim, T.; Chung, H.; Jang, H.; Lee, J.; Kim, D.; Jang, E., Highly Efficient and Stable InP/ZnSe/ZnS Quantum Dot Light-Emitting Diodes. *Nature* **2019,** *575* (7784), 634-638.

114. Taylor, D. A.; Teku, J. A.; Cho, S.; Chae, W.-S.; Jeong, S.-J.; Lee, J.-S., Importance of Surface Functionalization and Purification for Narrow FWHM and Bright Green-

Emitting InP Core–Multishell Quantum Dots via a Two-Step Growth Process. *Chemistry of Materials* **2021,** *33* (12), 4399-4407.

115. Uematsu, T.; Doi, T.; Torimoto, T.; Kuwabata, S., Preparation of Luminescent $AgInS_2$−$AgGaS_2$ Solid Solution Nanoparticles and Their Optical Properties. *The Journal of Physical Chemistry Letters* **2010,** *1* (22), 3283-3287.
116. Kameyama, T.; Okazaki, K.-i.; Ichikawa, Y.; Kudo, A.; Kuwabata, S.; Torimoto, T., Photoluminescence Enhancement of ZnS–$AgInS_2$ Solid Solution Nanoparticles Layer-by-Layer-Assembled in Inorganic Multilayer Thin Films. *Chemistry Letters* **2008,** *37* (7), 700-701.
117. Thi Thu Huong, T.; Loan, N. T.; Ung, T. D. T.; Tung, N. T.; Han, H.; Liem, N. Q., Systematic Synthesis of Different-Sized $AgInS_2/GaS_x$ Nanocrystals for Emitting the Strong and Narrow Excitonic Luminescence. *Nanotechnology* **2022,** *33* (35), 355704.
118. Jiang, C.; Tozawa, M.; Akiyoshi, K.; Kameyama, T.; Yamamoto, T.; Motomura, G.; Fujisaki, Y.; Uematsu, T.; Kuwabata, S.; Torimoto, T., Development of Cu-In-Ga-S Quantum Dots with a Narrow Emission Peak for Red Electroluminescence. *The Journal of Chemical Physics* **2023,** *158* (16), 164708.
119. Hughes, K. E.; Ostheller, S. R.; Nelson, H. D.; Gamelin, D. R., Copper's Role in the Photoluminescence of $Ag_{1-x}Cu_xInS_2$ Nanocrystals, from Copper-Doped $AgInS_2$ ($x \sim 0$) to $CuInS_2$ ($x = 1$). *Nano Letters* **2019,** *19* (2), 1318-1325.
120. Kim, J.-H.; Han, C.-Y.; Lee, K.-H.; An, K.-S.; Song, W.; Kim, J.; Oh, M. S.; Do, Y. R.; Yang, H., Performance Improvement of Quantum Dot-Light-Emitting Diodes Enabled by an Alloyed ZnMgO Nanoparticle Electron Transport Layer. *Chemistry of Materials* **2015,** *27* (1), 197-204.
121. Motomura, G.; Uematsu, T.; Kuwabata, S.; Kameyama, T.; Torimoto, T.; Tsuzuki, T., Quantum-Dot Light-Emitting Diodes Exhibiting Narrow-Spectrum Green

Electroluminescence by Using Ag–In–Ga–S/GaS_x Quantum Dots. *ACS Applied Materials & Interfaces* **2023,** *15* (6), 8336-8344.

122. Nguyen, L. M.; Dellinger, M. E.; Lee, J. T.; Quinlan, R. A.; Rheingold, A. L.; Pike, R. D., Convenient Synthesis of Copper (I) Thiolates and Related Compounds. *Inorganica Chimica Acta* **2005,** *358* (4), 1331-1336.
123. Alivisatos, A. P., Perspectives on The Physical Chemistry of Semiconductor Nanocrystals. *Journal of Physical Chemistry* **1996,** *100* (31), 13226-13239.
124. Sercel, P. C.; Efros, A. L., Band-Edge Exciton in CdSe and Other II–VI and III–V Compound Semiconductor Nanocrystals − Revisited. *Nano Letters* **2018,** *18* (7), 4061-4068.
125. Wuister, S. F.; de Mello Donegá, C.; Meijerink, A., Influence of Thiol Capping on the Exciton Luminescence and Decay Kinetics of CdTe and CdSe Quantum Dots. *The Journal of Physical Chemistry B* **2004,** *108* (45), 17393-17397.
126. Guyot-Sionnest, P.; Wehrenberg, B.; Yu, D., Intraband Relaxation in CdSe Nanocrystals and The Strong Influence of The Surface Ligands. *The Journal of Chemical Physics* **2005,** *123* (7), 074709.
127. Uehara, M.; Watanabe, K.; Tajiri, Y.; Nakamura, H.; Maeda, H., Synthesis of $CuInS_2$ Fluorescent Nanocrystals and Enhancement of Fluorescence by Controlling Crystal Defect. *The Journal of Chemical Physics* **2008,** *129* (13), 134709.
128. Kim, Y.-K.; Ahn, S.-H.; Chung, K.; Cho, Y.-S.; Choi, C.-J., The Photoluminescence of $CuInS_2$ Nanocrystals: Effect of Non-Stoichiometry and Surface Modification. *Journal of Materials Chemistry* **2012,** *22* (4), 1516-1520.
129. Aldakov, D.; Lefrançois, A.; Reiss, P., Ternary and Quaternary Metal Chalcogenide Nanocrystals: Synthesis, Properties and Applications. *Journal of Materials Chemistry C* **2013,** *1* (24), 3756-3776.

130. Rice, W. D.; McDaniel, H.; Klimov, V. I.; Crooker, S. A., Magneto-Optical Properties of $CuInS_2$ Nanocrystals. *The Journal of Physical Chemistry Letters* **2014,** *5* (23), 4105-4109.

131. Knowles, K. E.; Hartstein, K. H.; Kilburn, T. B.; Marchioro, A.; Nelson, H. D.; Whitham, P. J.; Gamelin, D. R., Luminescent Colloidal Semiconductor Nanocrystals Containing Copper: Synthesis, Photophysics, and Applications. *Chemical Reviews* **2016,** *116* (18), 10820-10851.

132. Knowles, K. E.; Nelson, H. D.; Kilburn, T. B.; Gamelin, D. R., Singlet–Triplet Splittings in the Luminescent Excited States of Colloidal Cu^+:CdSe, Cu^+:InP, and $CuInS_2$ Nanocrystals: Charge-Transfer Configurations and Self-Trapped Excitons. *Journal of the American Chemical Society* **2015,** *137* (40), 13138-13147.

133. Zang, H.; Li, H.; Makarov, N. S.; Velizhanin, K. A.; Wu, K.; Park, Y.-S.; Klimov, V. I., Thick-Shell $CuInS_2$/ZnS Quantum Dots with Suppressed "Blinking" and Narrow Single-Particle Emission Line Widths. *Nano Letters* **2017,** *17* (3), 1787-1795.

134. Jang, J. S.; Borse, P. H.; Lee, J. S.; Choi, S. H.; Kim, H. G., Indium Induced Band Gap Tailoring in $AgGa_{1-x}In_xS_2$ Chalcopyrite Structure for Visible Light Photocatalysis. *The Journal of Chemical Physics* **2008,** *128* (15), 154717.

135. Motomura, G.; Iwasaki, Y.; Kameyama, T.; Torimoto, T.; Uematsu, T.; Kuwabata, S.; Tsuzuki, T., Green Electroluminescence Generated by Band-edge Transition in Ag-In-Ga-S/GaS_x Core/Shell Quantum Dots. *ITE Transactions on Media Technology and Applications* **2021,** *9* (4), 222-227.

136. Motomura, G.; Ogura, K.; Iwasaki, Y.; Uematsu, T.; Kuwabata, S.; Kameyama, T.; Torimoto, T.; Tsuzuki, T., Electroluminescence from Band-Edge-Emitting $AgInS_2$/GaS_x Core/Shell Quantum Dots. *Applied Physics Letters* **2020,** *117* (9).

Acknowledgements

I would like to express my sincerest gratitude to Professor Dr. Susumu Kuwabata at the Department of Chemistry, Graduate School of Engineering, Osaka University, who provided me an opportunity to join his research group. He always share his valuable experiences and suggestions that have proven beneficial for both my future career and personal growth. I feel deeply honored to have had the opportunity to be his student.

I would like to express my gratitude to Professor Dr. Ken-ichi Nakayama and Professor Dr. Furukawa Shinya at the Department of Chemistry, Graduate School of Engineering, Osaka University for their reviewing this thesis with helpful suggestions. Besides, I would like to express my gratitude to Associate Professor Dr. Taro Uematsu at the Department of Chemistry, Graduate School of Engineering, Osaka University. Without his guidance and heartwarming encouragement, I would not have been able to complete my thesis. Whenever I encountered difficulties during my experiments, he always gave me valuable guidance and warm encouragement. Additionally, he always provides a clear explanation and valuable feedback, even though he is very busy with his tasks. The knowledge and skills I acquired under his mentorship will undoubtedly contribute to my growth as an efficient researcher in this field.

I would like to express my thanks to Mrs Miyuki Takahama, the secretary in my laboratory, for her great support. Whenever I am with her, her kindness and caring nature makes me feel incredibly comfortable, just like being with my mother. Besides, I would like to thank all lab members for accepting me as a part of this laboratory, even though I am a foreigner. Every moment we shared, be it at parties or trips, was an irreplaceable and priceless one, which I will never forget.

I would like to express my thanks to my family members, especially Mrs Managa Krobkrong, my mother, Mr. Thanyakade Thanyaprasertsiri, my father, and Miss Matimon Krobkrong, my sister. Even though I rarely had contact owing to my tight schedule, their presence always encourage me to overcome all the challenges in my doctoral journey. Furthermore, I would like to express my thanks to Mr. Thanakorm Yeamsusawat, Miss Watusiri Suwannarat, Miss Thanyarat Phutthaphongloet, and Miss Sukulya Bunuasunthon, Thai colleagues, Miss Niphapat Singkhornard, Mr. Amir Narongussadorn, my friends, Miss Nutchanikan Phiromphu, my junior, and Miss Phatchada Santawaja, my senior. They always stand by me and help me regain my focus when I lose my direction. I really appreciate them for being my attentive listeners, supportive companions, and valuable advisors during my struggles.

Last but not least, I would like to express my heartfelt gratitude to myself for overcoming the numerous mental and physical obstacles I encountered for three years. My life in Japan was fulfilled with a variety of both negative and positive moments. I am grateful to myself for never surrendering or escaping from problems. I sincerely say that experiences and relationships I gained over 3 years in Japan is going to become precious memories, unforgettable lessons and invaluable treasures that will resonate throughout the rest of my life.